UC Santa Cruz
UC Santa Cruz Electronic Theses and Dissertations

Title
Realization of Planar Silicon Sensors for Fast Timing Experiments

Permalink
https://escholarship.org/uc/item/23j1h7hx

Author
Parker, Colin James

Publication Date
2013

Peer reviewed|Thesis/dissertation

eScholarship.org Powered by the California Digital Library
University of California

UNIVERSITY of CALIFORNIA
SANTA CRUZ

REALIZATION OF PLANAR SILICON SENSORS FOR FAST TIMING EXPERIMENTS

A thesis submitted in partial satisfaction of the
requirements for the degree of

MASTER OF SCIENCE

in

PHYSICS

by

Colin James Parker

September 2013

The Thesis of Colin James Parker
is approved:

Professor Jason Nielsen, Chair

Professor Hartmut Sadrozinski

Professor Abraham Seiden

Tyrus Miller
Vice Provost and Dean of Graduate Studies

Copyright © by

Colin James Parker

2013

Contents

List of Figures

List of Tables

Abstract

Realization of Planar Silicon Sensors for Fast Timing Experiments

by

Colin James Parker

We propose a new silicon sensor design capable of ultra fast (10's of ps) detection for experiments measuring time of flight (ToF) signals. The new design will couple fast readout with the current precise spatial resolution (10's of μm) of silicon pixels. Charge multiplication via impact ionization is exploited to mitigate the loss of signal from the new detectors, which are necessarily thin to shorten carrier collection times. A study of charge multiplication in 300 μm pad diodes manufactured at CNM Barcelona is presented and results are compared with simulations from a commercial TCAD software package. Observed gain factors are measured to be between 3 and 5, demonstrating proof of principle for charge multiplication in planar silicon sensors.

To Emily,

Behind every great opus is a muse

Acknowledgements

Many thanks to the Department of Energy for partially funding this project, as well as CERN's RD50 group for financial and collaborative support. I graciously acknowledge Giulio Pellegrini, Salvador Hidalgo, Pablo Fernández-Martínez, and the rest of the processing team at Centro Nacional de Microelectrónica in Barcelona for providing the samples and comparative measurements for the studies conducted in this thesis. Additionally, I thank Gian-Franco Dalla Betta and Marco Povoli from the Università Degli Studi Di Trento for training, access and support for the software used to conduct the simulations discussed in this thesis. Finally, I would like to thank my colleagues Zach Galloway, Jeffery Ngo, and Davi Schumacher for their help in taking many measurements, my advisors Hartmut Sadrozinski and Vitaliy Fadeyev as well as the rest of my research group for much fruitful discussion about the subject, and the rest of the brilliant minds at SCIPP for constantly inspiring me through the quality of their work.

1 Particle Detection

1.1 Introduction

Though it has been speculated for ages, only in the last 2 centuries has it been observed and proven that the microscopic constituents of nature are particulate. This newfound knowledge has proven to be advantageous in some areas of scientific research and medicinal treatment. High energy physics (HEP) experiments like ATLAS, shown in Fig. 1.1, are attempting to probe deeper into the constituents of matter to characterize particles further, as well as discover new and exotic particles [1]. Medical facilities can also use rather non-intrusive radiation in both observation and treatment of a particular area of interest inside the body of a patient. In each case, the success of the experiment is dependent on the ability to efficiently detect the presence of the particle in question.

Since the 1950's, silicon detectors have been used to detect subatomic particles in experiments [2]. When the silicon detector is used as an ionization chamber, a charged particle liberates electrons and holes as it passes through the material. These carriers are free to drift towards an electrode under the influence of an electric field, and the induced current on the electrodes can be amplified, read out, and registered as a particle hit. In this way, particle tracks can be reconstructed when whole systems of detectors and readout chains are working in unison. A sensor in operation is shown in Fig. 1.2 and an example depicting reconstructed particle tracks is shown in Fig. 1.3.

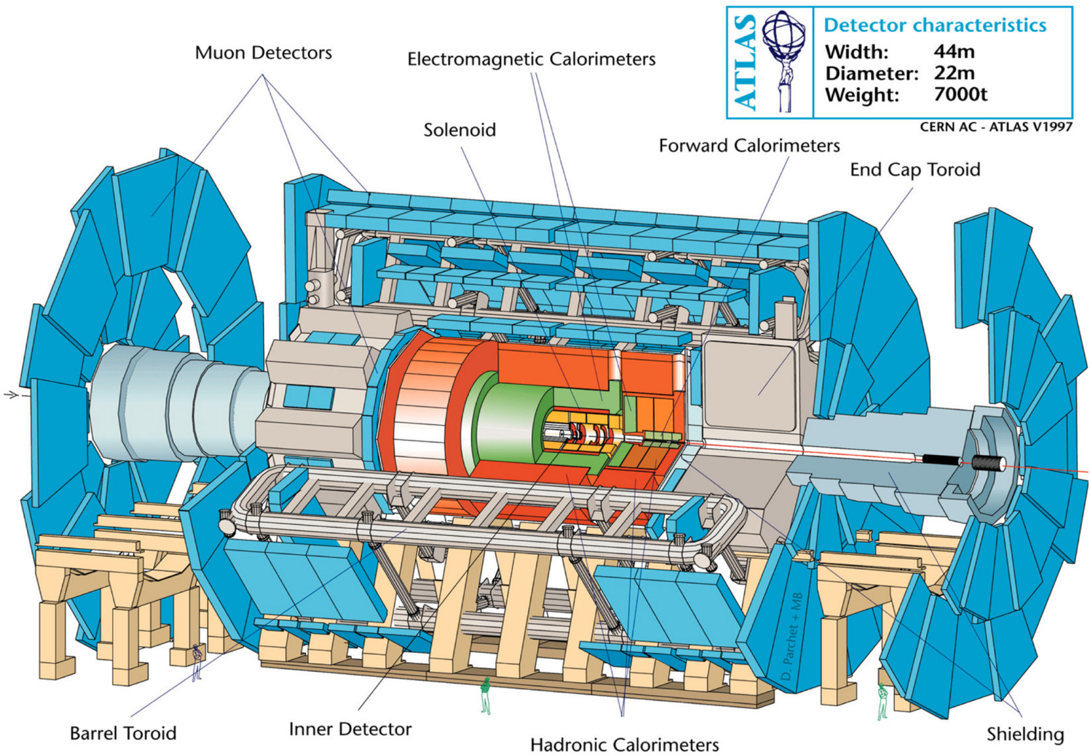

Figure 1.1: The ATLAS Detector at the LHC. Silicon pixels, silicon strips, and straw tubes make up the inner detector, which has the most precise spatial resolution. [1]

Having revolutionized the electronics industry, crystalline silicon's desirable properties have been deeply investigated and well characterized. It's density, crystal structure, and bandgap parameters ensure a traversing minimum ionizing particle (MIP) is most likely to deposit 246 eV per micron of silicon traversed. If the average ionization energy for an electron-hole pair is 3.6 eV this corresponds to 73 electron-hole pairs / um. A typical thickness is 300 μm so the total charge ionized would be close to 22 kpairs or 3.5 fC [3] [4].

Spatial resolution becomes important when reconstructing a particle track. In most HEP experiments, the sensor of choice is the planar sensor, referring to the coplanar readout electrodes located at the surface of the device. It is impossible to dice a silicon wafer into pieces of order 100 μm, which is small enough for efficient particle tracking. Thus to improve spatial resolution, sensors are designed with multiple closely spaced readout electrodes on the

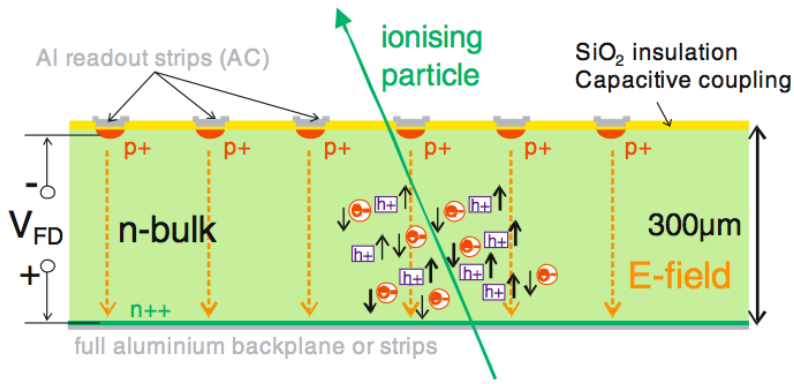

Figure 1.2: Labeled diagram of a typical n-type planar silicon strip detector in operation as an ionizing particle passes through. [2]

same silicon bulk. The simplest and least precise geometry is that of the pad diode, where two parallel, contiguous electrodes are located at the top and bottom surfaces. Next, electrodes can be arranged in strips spaced around 100 μm apart for fine one-dimensional resolution. Finally the 2D pixel sensors have point-like electrodes and a typical pixel like that in Fig. 1.4 covers an area of order 100's of μm.

The increased spatial precision trades off with additional design complexity and power required for the increased number of readout channels, so the application dictates which geometry is necessary. A segmented geometry ensures the position resolution is determined by $\frac{p}{\sqrt{12}}$, where p is the strip pitch, for a final position precise to order 10's of μm, which is among the most precise methods of particle tracking available.

The current generated by the radiation passing through the silicon detector is only the first step in the readout chain. The next steps include amplification of the current and signal shaping for the digitizer. Signal shaping times are tunable in principle but must be optimized for lowest noise possible while maintaining sufficient count rate capability. In addition, digital signal processing has an upper bound on its rate as well. In HEP, the accelerated beam of particles is distributed in "microbunches," which make crossings at the detector at a certain rate, depicted in Fig. 1.5. The electronics in this case are designed to have a timing resolution

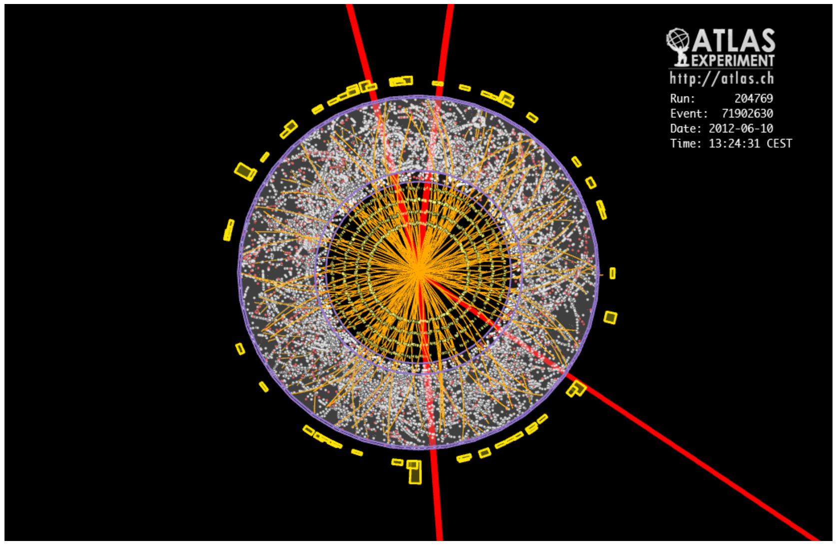

Figure 1.3: ATLAS tags a four muon decay, which is a possible decay mode for the elusive Higgs Boson. The muons' and other particles' tracks are reconstructed with the help of silicon detectors. [1]

only as precise as required from this microbunch crossing frequency [4] [7].

For particle experiments requiring ultra high timing resolution, the preferred choice of detector is the photomultiplier tube (PMT). In practice, one couples Cherenkov radiators with a multi channel PMT to sense an event as fast as 15 ps [8]. These sensors, however measure around several to several hundred mm^2, and therefore may lack significant spatial information about an event [9].

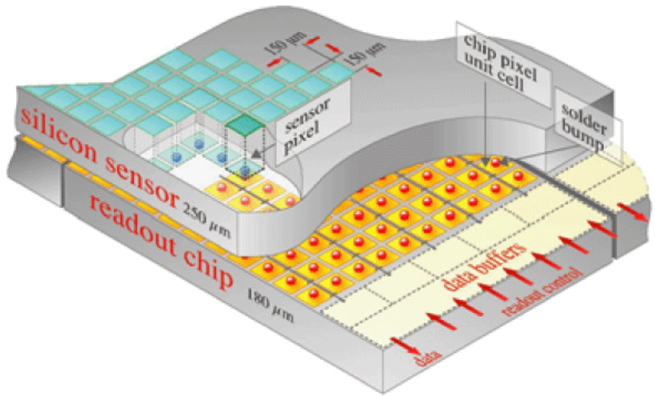

Figure 1.4: Planar pixel sensor geometry is shown mounted on top of readout electronics. Note each unit pixel constitutes a readout channel, allowing for precise spatial resolution. [6]

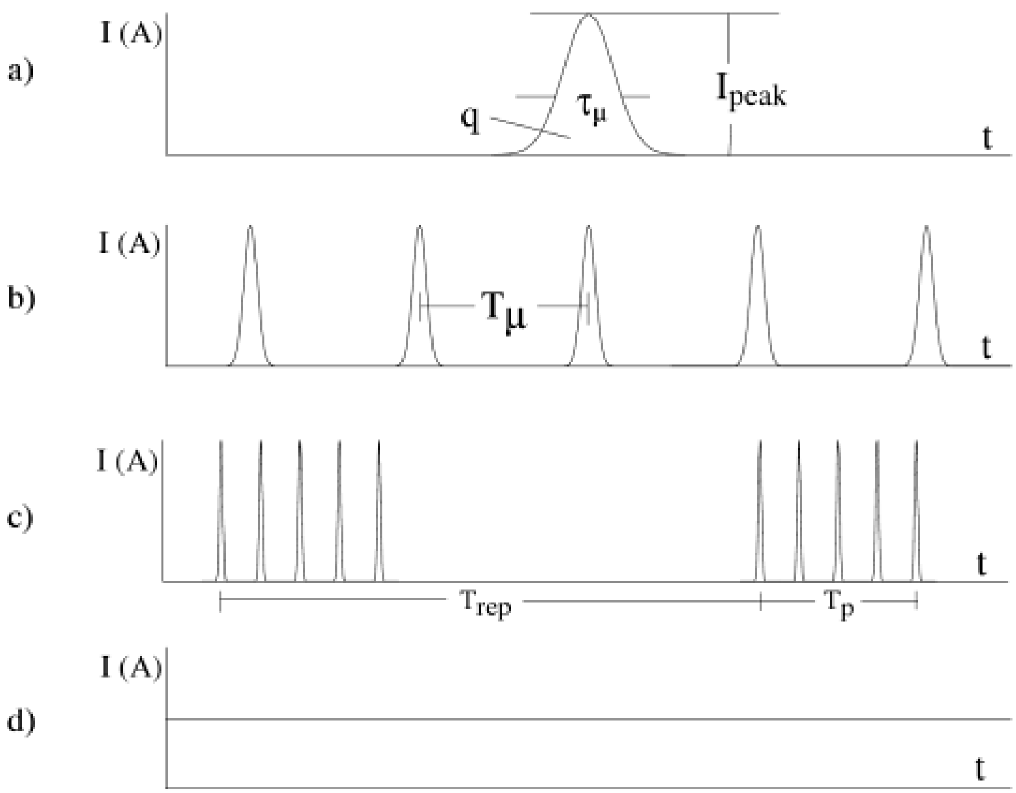

Figure 1.5: A figure from [6] showing beam timing structure. a) The current passing the detector comes in bursts called "microbunches" that last for a certain period. b) The spacing of these micro bunches has a longer period. c) Finally, the group of micro bunches cross the detector after an even longer period. The shaping time for the electronics should be chosen with a) - c) in mind as well as the expected channel occupancy. d) A constant beam current is shown for comparison.

1.2 Motivation for Further Developments

As technology progresses, so too does the sophistication of particle experiments. Sensors must be engineered to meet new demands. Currently, there are several experiments that would greatly benefit by implementing the precise spatial resolution of planar silicon sensors with fast timing of order similar to PMT's mentioned above. Sensors of this caliber will be dubbed 4D, referring to the three spatial and one time dimensions.

At the LHC, protons are collided at relativistic speeds. After the beam bunches cross, some interesting processes produce final state protons that scatter at small angles and small momentum loss. If the detectors placed $\pm$ hundreds of meters down the tunnel could observe these "forward" protons, much information could be determined about the event itself. In addition, vertex association would be possible, and background pile-up could be reduced by a factor of 25 [5]. The "ATLAS Forward Physics" project proposes a detector shown in Fig. 1.6 that will use both planar pixels and micro-channel PMT's, though a single 4D sensor could accomplish the same goal with simpler hardware and fewer components.

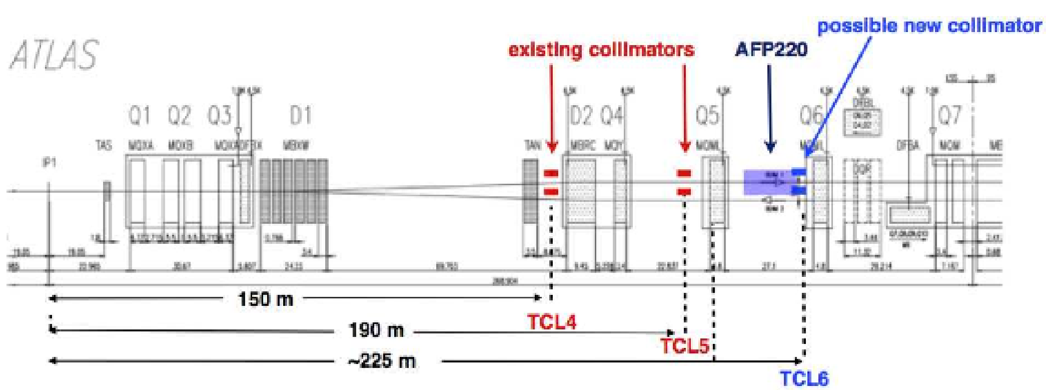

Figure 1.6: The proposed "Forward Detector" on ATLAS for observing slightly deflected protons. Placement of the detector is around +/- 200m from the main detector, and thus requires fast timing resolution for vertex reconstruction at the origin. [5]

Another area of interest for 4D sensors would be any experiment accounting for time of flight (ToF). ToF measurements use a signal's timing information to determine the particle's velocity in a known distance. If the signal propagates at speed c in the medium, a timing resolution of Δt results in a spatial resolution of Δx through the elementary equation $\Delta x = c \times \Delta t$. In this case an increase in timing resolution would correspond to an increase in spatial resolution by the same factor.

For instance, Fig. 1.7 shows the Alpha Magnetic Spectrometer AMS-02 on board the International Space Station. AMS-02 uses four planes of scintillators to examine the ToF of traversing cosmic rays to tag velocity and charge [10]. Shown in Fig. 1.7, the ToF detector must be used in conjunction with position detectors and has a time resolution of 150 ps [11]. The perfection of a 4D sensor would allow not only a combination of both ToF and position tracking in the same device, but may actually improve the timing precision by a factor of 2 or 3.

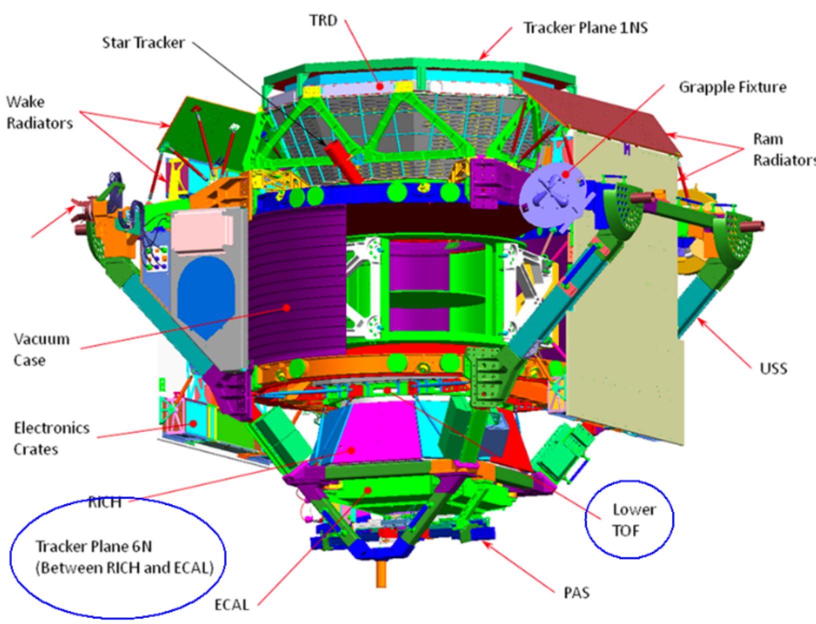

Figure 1.7: A diagram of the systems onboard the AMS 02 Experiment on the International Space Station. The lower ToF and silicon trackers are circled [10].

ToF measurements are also relevant in 3D imaging, where a sensor emits photons to be reflected and reabsorbed and the time in-between events determines the object's distance from the sensor. ToF cameras are commercially available with depth precision to about 1 cm, but

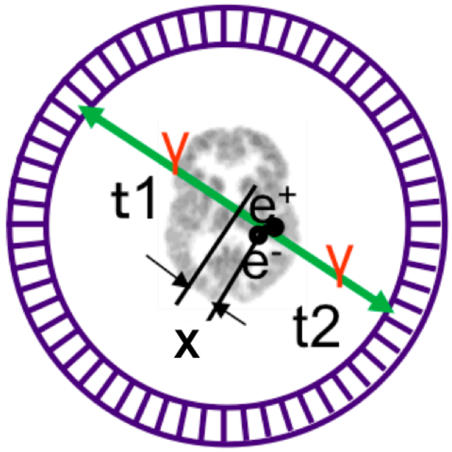

Figure 1.8: With ToF measurements, PET scans will benefit from increased spatial resoultion. In this diagram, the photons arriving at times t1 and t2 correspond to a position uncertainty x. [14]

are often limited to 320×240 pixels, which is far lower than the resolution of a typical modern camera [12]. Presumably this figure could be greatly improved with a 4D silicon sensor, which would have depth resolution to a few mm and a much higher pixel density.

In positron-electron tomography (PET), a positron emitted from a radioactive tracer annihilates quickly with a nearby electron from an atom in a lesion. Since the center-of-mass momentum is small, the annihilation produces two photons that travel in nearly opposite directions. Traditional PET scans have no timing information, so the annihilation event can occur at any point along the line of flight. A ToF measurement would provide the difference in timing from the photons' signals and thus information about the event location along the line of annihilation. A diagram of the ToF PET measurement is shown in Fig. 1.8. A timing resolution of 100 ps gives spatial information to within 1.5 cm [13].

It should be noted that fast slewing signals would be of little value without fast enough readout electronics. Though it may be new territory, some prototypes of readout chips for timing resolution to 10's of ps are in development. For example, the Gigatracker (GTK) at CERN's fixed target experiment NA62 will have a time tagging resolution of 150 ps, though the goal of the readout is to reach 50 ps timing [9].

2 Fast Detection: Concept to Implementation

2.1 Semiconductor Physics

Any information about the passage of a particle event is interpreted from the movement of charge in the sensor, which is detected as electric current and processed in the readout chain. Charge carriers are accelerated under the influence of a local electric field, and are said to be moving at some drift velocity. In introductory texts the relation between drift velocity (v) and electric field (E) is examined at low enough fields such that the dependence is approximately linear $v = \mu E$. Here, μ is the constant of proportionality dubbed carrier mobility [15] [16]. The general case is examined in [17] and takes the form

$$v = \frac{\mu E}{(1 + (\frac{E}{E_c})^{\beta})^{\frac{1}{\beta}}} \tag{2.1}$$

At a temperature of 300 K, the parameters E_c, β, and μ are determined from the data for both electrons and holes and shown in Table 1.1. A plot of the function is shown in Fig. 2.1.

The mobility of carriers in the lattice is dependent on the probability of scattering. Acoustic phonons, impurity states, and other carriers are dominant contributors to scattering for doped silicon at room temperature. In addition, the mobilities of electrons and holes are different because the transport mechanisms are different. At high fields, the asymptotic behavior

T(K)	β	$E_c(V/cm)$	$\mu(cm^2/V\dot{s})$	v_{sat}
Electrons				
300	1.30	7240	1450	1.05×10^7
370	1.44	9500	900	8.55×10^6
430	1.66	12420	600	7.45×10^6
Holes				
300	1.30	18000	450	8.10×10^6
370	1.25	25800	305	7.87×10^6
430	1.28	32700	210	6.86×10^6

Table 2.1: Best fit parameters for equation (5.1) from data measured and discussed in [17].

of the mobility acts to saturate the carrier drift velocity. At fields above 50 kV/cm, electrons will move at about 100 μm/ns and holes about 80 μm/ns [15] [16].

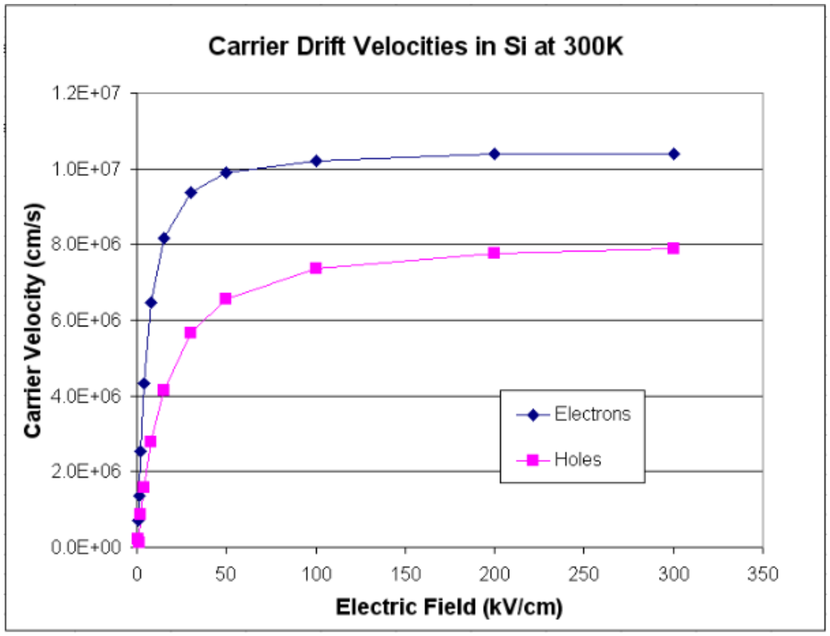

Figure 2.1: A plot of equation (2.1) with parameter fits discussed in [17]. Note that at high fields the velocities saturate to a maximum value.

In heterogeneous silicon, an abrupt junction exists at the boundary demarcating excess donor and excess acceptor states. At room temperature, the impurity states in silicon are mobile, so the diffusion of carriers across the junction leaves behind space charge ions in a "depletion" region devoid of carriers. This depletion region has an associated electric field due to these space charge ions. The equilibrium charge density, electric fields, and energy band diagrams for a p-n junction are shown in a diagram in Fig. 2.2. By altering the equilibrium potential across the junction, one controls the width of the depletion region and thus the electric field. In reverse bias operation, a potential is applied such that the depletion region increases and the free charge ionized by a traversing particle will drift under influence of this space charge electric field [2] [15] [16].

In standard planar sensor geometries, the readout amplifier is insulated from the collecting implant. Consequently, the readout electrode maintained at constant potential conducts a current induced by charges moving inside the sensor bulk. Ramo's theorem [3] says that this

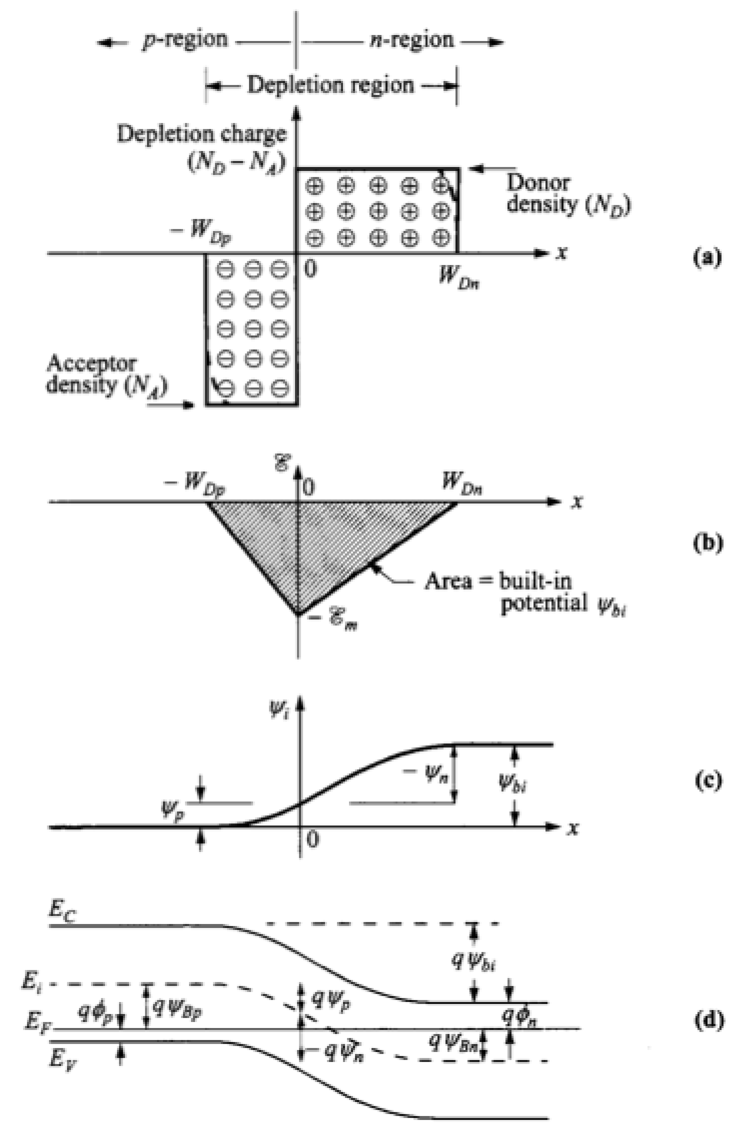

Figure 2.2: Thermal equilibrium characteristics of an abrupt p-n junction as discussed in [15]. a) The space charge distribution. (In this case $N_a > N_d$). b) The resultant electric field profile from the space charge. c) The electrostatic potential difference across the junction. d) The energy band diagram near the junction. [15]

induced current does not exactly mirror the shape of the current pulse, but is proportional to the weighting field component in the direction of the carrier's motion. The weighting field is obtained by placing the electrode of interest at unit potential and all others at ground as shown in Fig. 2.3. In general, the weighting field is stronger the closer to the conductor at unit potential, so the induced current in the amplifier is larger the closer the charge is to the collection electrode [3]. The effect of the weighting field on a moving charge is shown in Fig. 2.4.

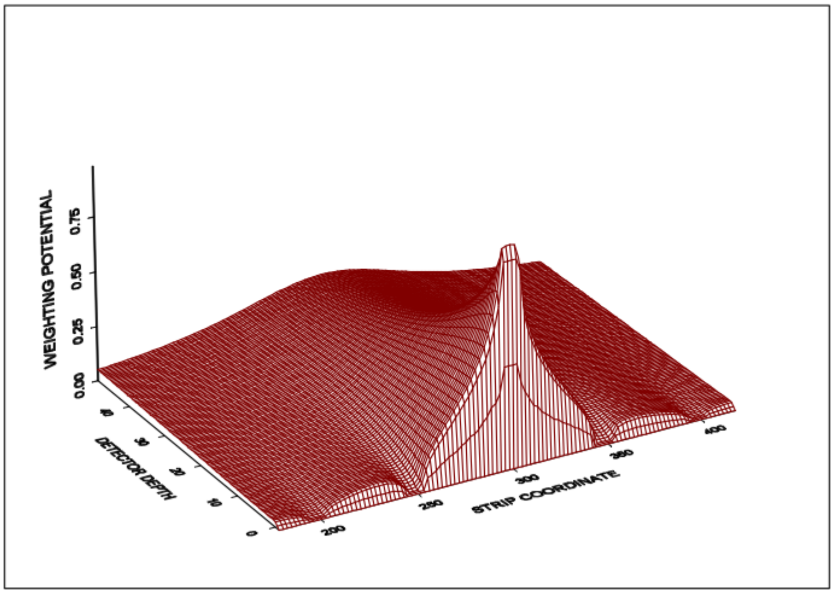

Figure 2.3: Simulation of a 50 μm pitch strip geometry. The central strip is held to 1V and neighbors at ground, and the resulting potential is plotted. The weighting field extracted from this simulation is important in the calculation of the induced current on the input leg of the readout chain. [3]

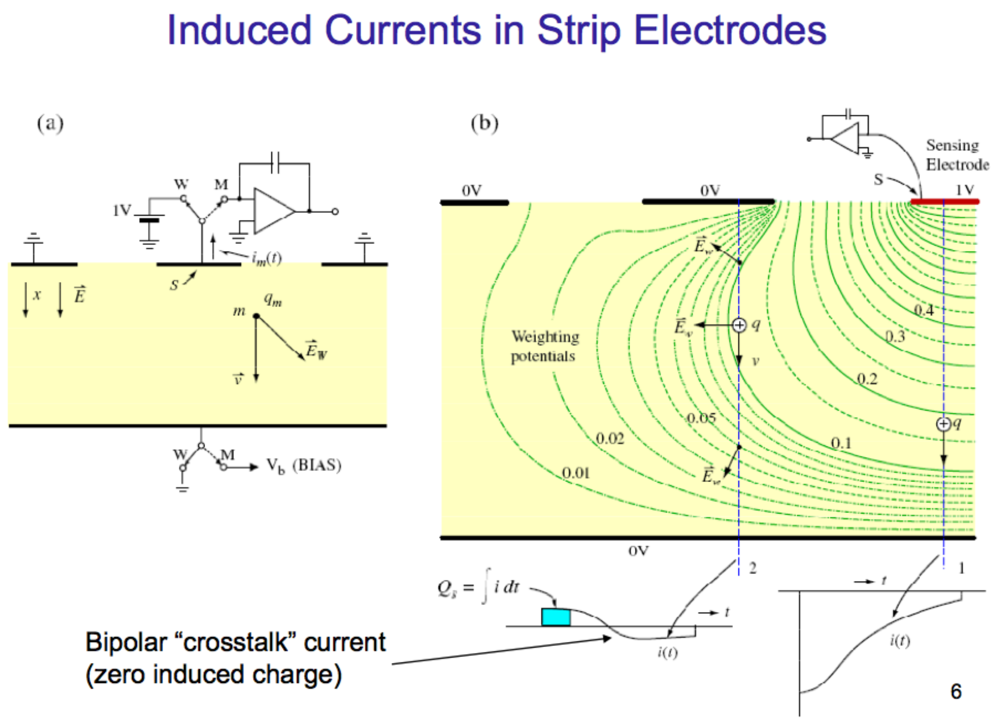

Figure 2.4: A Diagram to show the effect of the weighting field on a moving charge. In a), the circuit diagram is shown with weighting (W) and operational (M) potentials. In b), the induced current on a readout electrode is shown for a charge moving towards 1) the same electrode and 2) a neighbor electrode. Note in 2) there is no net charge induced. [18]

Considering the design of detectors with fast timing capabilities, one would naturally desire to operate with minimum charge collection time. This corresponds to maximum possible drift velocity, which is saturated in the case of high electric field. If established fields are high enough to guarantee saturated drift velocity, the collection time becomes a function only of the distance the carrier will travel. This then leads to the following conclusion: To measure a faster current pulse in a planar silicon detector, one must design a thinner device.

2.2 Thin Detectors

"Is it possible?" This is one of the first naturally occurring inquiries about any new engineering project. Luckily, someone has answered the question before us. Our collaborators at CNM are producing sensors as thin as 10 μm [19]. The production process is depicted in Fig. 2.5.

There are a few drawbacks to account for in thin sensor design. A traversing MIP deposits charge proportional to the distance traveled inside the device. Shorter distance results in a smaller signal. Another problem is the increased capacitance due to backplane proximity to surface electrodes, which acts to increase the noise. Finally, conclusions from [20] assert that traversing particles' energy loss per unit length is less in thinner silicon layers resulting in fewer ionized mobile charges. A plot of this reduced energy loss is shown in Fig. 2.6. These three combined effects reduce the signal to noise ratio (S/N), which for effective operation should be above 10 [21].

Fortunately, there is a way in theory to combat the smaller initial charge, through charge multiplication via impact ionization. In this way, the reduced initial charge is augmented by a certain gain factor that will be optimized to give an appreciable signal. There is a tradeoff between collection time (dependent on sensor thickness) and required gain (determined by S/N ratio), which is depicted in Table 2.2.

Thickness	Backplane Capacitance		Signal	Collection Time	Gain Required	
[um]	Pixels [fF]	Strips [pF/mm]	[No. of e-]	[ps]	for 2000 e-	for 12000 e-
1	250	5.0	35	13	57	343
2	125	2.5	80	25	25	149
5	50	1.0	235	63	8.5	51
10	25	0.50	523	125	3.8	23
20	13	0.25	1194	250	1.7	10.4
100	3	0.05	6954	1250	0.29	1.7
300	1	0.02	23334	3750	0.09	0.5

Table 2.2: Some relevant quantities to consider when designing a thin sensor are presented here. The numbers presented are results of simple scaling calculations [22]

2.3 Impact Ionization

Impact ionization in solid-state devices is traditionally described in a similar manner as Townsend discharge in gases [27], depicted in Fig. 2.7. The process occurs when a carrier

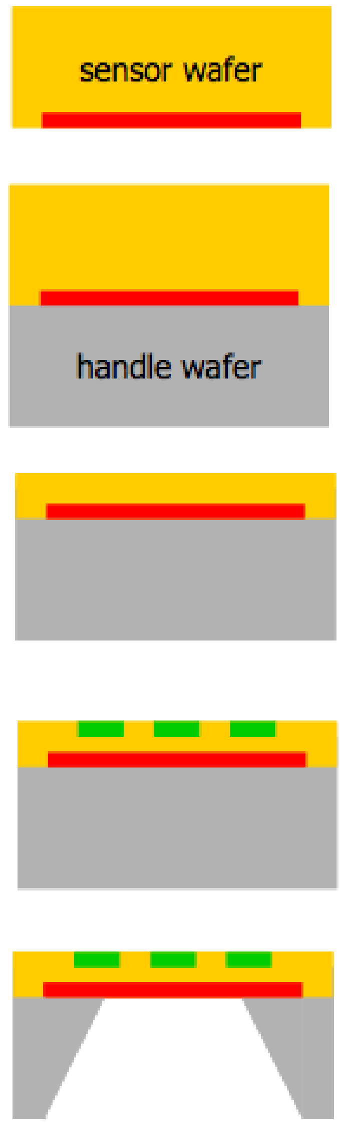

Figure 2.5: This cartoon demonstrates the necessary steps in fabricating thin sensors. [19]

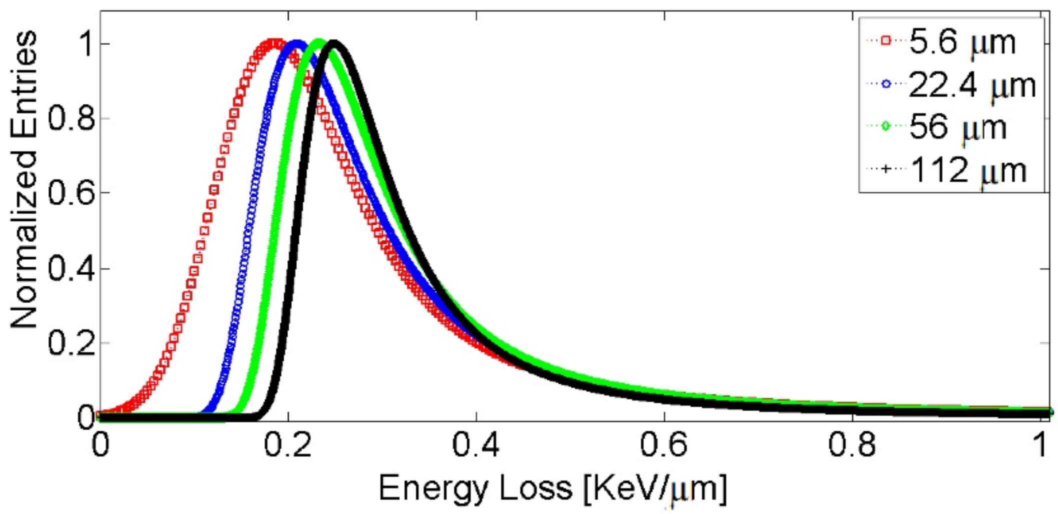

Figure 2.6: Results from a study of energy loss in silicon layers of different thickness. The results from 12 GeV protons demonstrate the reduction in energy loss for thinner layers of silicon. [20]

accelerated by the operational electric field acquires sufficient energy to ionize a lattice atom. The resultant electron-hole pair then accelerates in the field and is capable of ionizing another atom. This positive feedback loop can be the cause of avalanche breakdown in the reverse-biased diode, which is an undesirable condition for sensor operation. However, if the electric field is just less than the breakdown field in silicon, which is typically around 300 kV/cm [33] it is still possible to observe a moderate figure of charge multiplication from impact ionization. This is the desired condition for the thin 4D sensor design.

Charge multiplication in silicon detectors for HEP applications first gained attention several years ago from charge collection efficiency (CCE) data in highly irradiated sensors. It's well understood that irradiation introduces defect states in silicon's energy band gap that contribute to charge trapping [3] [4]. The trapped charge is not integrated within the shaping time so the absolute magnitude of collected charge is reduced. However, data show that at high fluences, CCE actually increases at high bias voltages. The fact that CCE climbs to values over 1 as in Fig. 2.8 shows the net charge read out is greater than the net charge deposited originally

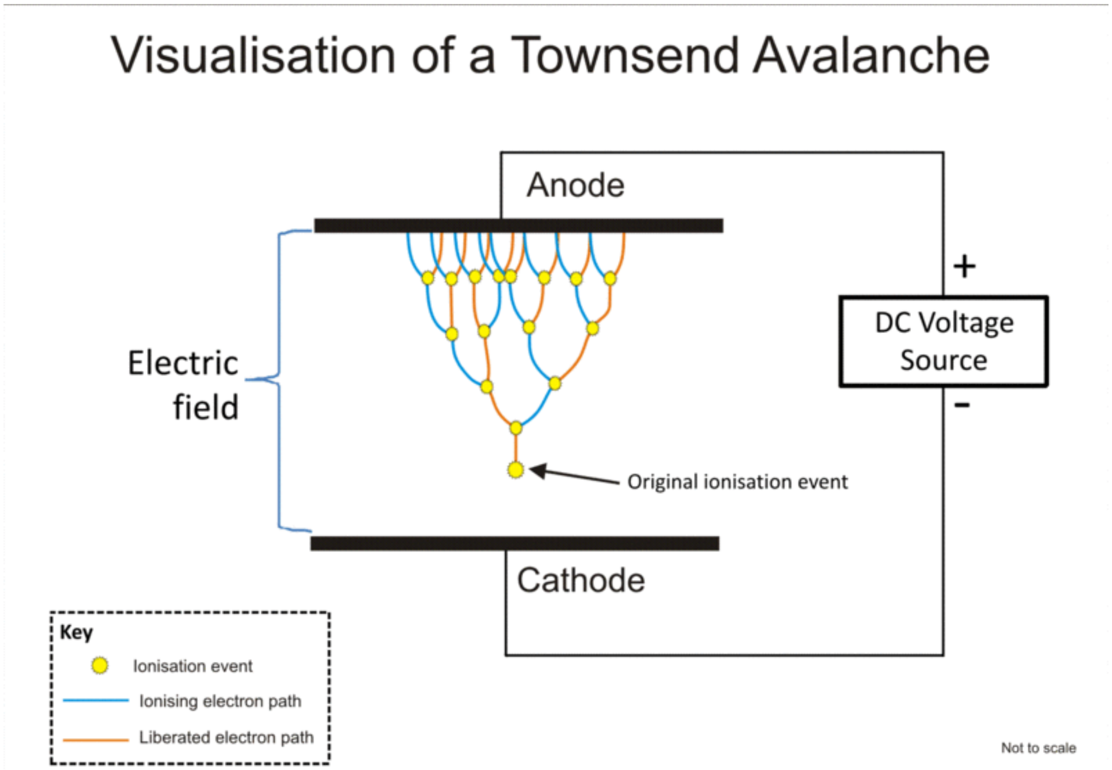

Figure 2.7: A cartoon illustrating avalanche ionization from a single energetic carrier. The figure represents Townsend Discharge, which describes the same mechanism in gases as impact ionization in solids. [23]

[24] [25].

Irradiation primarily introduces acceptor states [3], which alter the space charge and thus the electric field profile. Typically, the electric field near the p-n junction grows in magnitude with increased impurity states. A simulation of irradiation in a strip detector shows this effect in Fig. 2.9. At high enough fluences, the field is large enough that the onset of impact ionization is visible.

The ionization coefficient, usually dubbed α, is a strong function of the electric field and differs for electrons and holes.

$$\alpha_{e,h}(E) = \alpha_{e,h}(\infty)e^{(-b/E_{par})} \tag{2.2}$$

Here, α (∞) and b are parameters fit from data, and E_{par} is the electric field in the

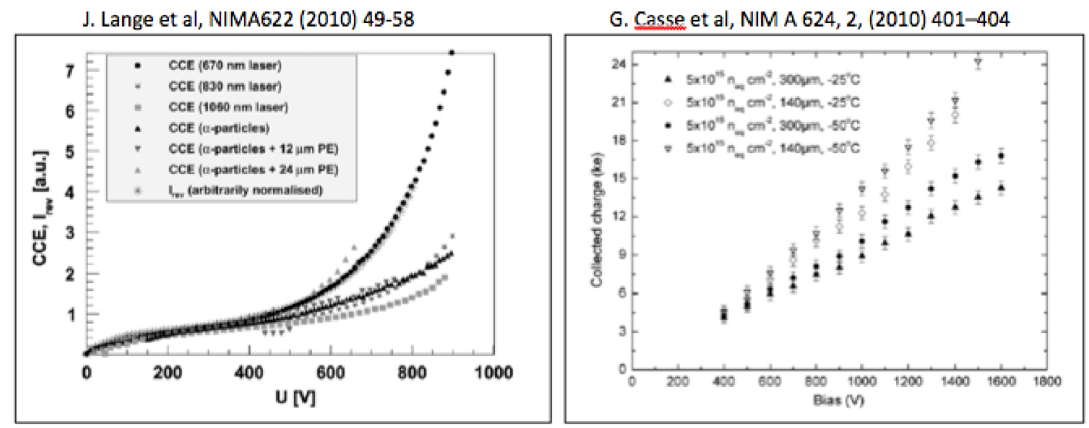

Figure 2.8: Plots from RD50 collaborators showing increased CCE for high fluences and bias voltages (strong electric fields), proof of the charge multiplication concept. [24] [25]

direction of the carrier velocity. This is known as Chynoweth's law, discussed thoroughly in [28]. Ionization coefficients have been measured thoroughly for both electrons and holes in Si for large fields [29], [30]. In [3] it is discussed that these formulae are only first approximations, valid for sufficiently smooth fields and long ionization regions. According to [31], under uniform field, temperature, and pressure

$$\frac{dN}{dx} = \alpha(x)N \tag{2.3}$$

which is integrated to

$$N(x) = N_o e^{(\int \alpha dx)} \tag{2.4}$$

In these equations, N is the number of carriers at any instant, N_0 is the number of initial carriers, and x is the distance traveled by the carriers. This gives the gain factor $G = \frac{N}{N_o}$ as the number of carriers after ionization over the number of original carriers.

There are two distinct states in which impact ionization manifests itself. If the electric field is less than the breakdown field in silicon, but still large enough to accelerate carriers into impact ionization, the response current is said to be linear, or proportional to the initial current. Breakdown occurs when both the electrons and holes created by impact ionization are accelerated to energies large enough to ionize again. The process continues indefinitely as electrons create holes and vice versa. The condition for this to happen is described by the ionization integrals for both electron and hole α coefficients. The mathematics is beyond the scope of this thesis but the interested reader can pursue more information in [15]. If the breakdown field in silicon is exceeded, the device is said to transition into Geiger mode, with gain approaching 10^4 [32]. The plot in Fig. 2.10 shows the transitions into the linear and Geiger modes for an typical avalanche photodiode.

The ionization coefficient is plotted in Fig. 2.11. The breakdown field in Si is usually considered to be close to 300kV/cm [33], where α_e is close to 1 per μm and α_h is close to 0.1 per μm. If it is possible to establish a field near this range in an operational sensor, it is clear that at this field the drifting electrons will ionize exponentially more carriers than drifting holes will for the same distance. The importance point here is to note that to operate a sensor with linear gain and no avalanche breakdown it will be necessary to accelerate electrons into moderate multiplication but keep holes below ionization energy.

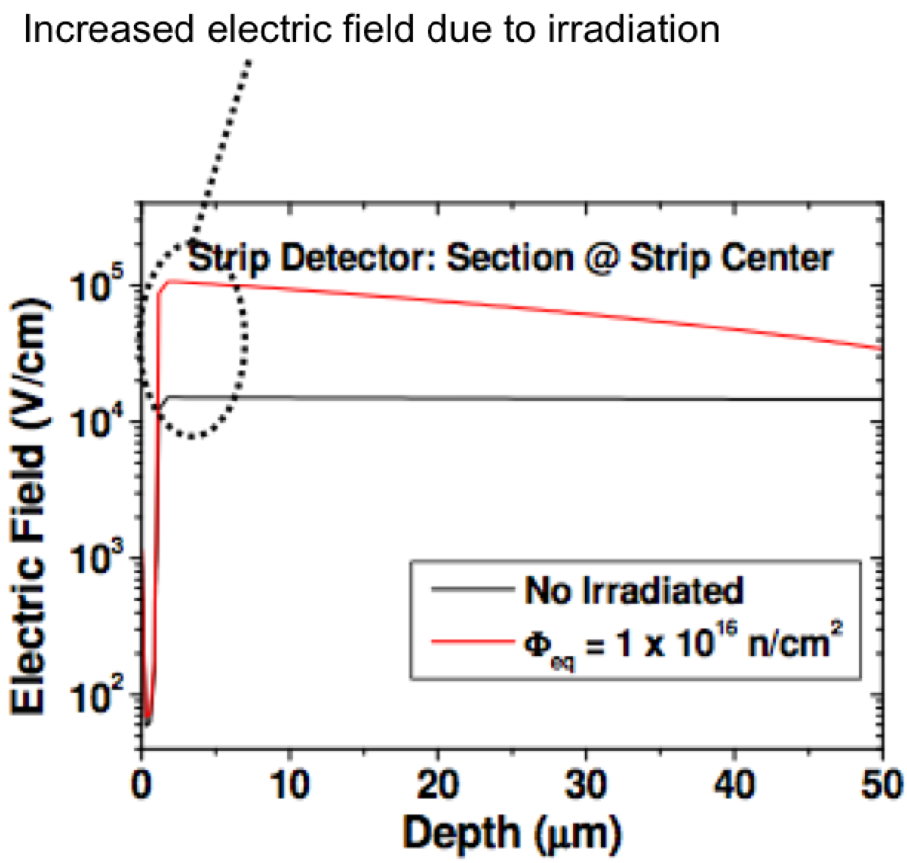

Figure 2.9: Irradiation alters space charge, which is modeled by introducing a deep donor state and a deep acceptor state in the bandgap. The resultant electric field is plotted for the unirradiated case and for a fluence of 1e16 n.eq. Note the higher the fluence the higher the field peak near the electrode. [26]

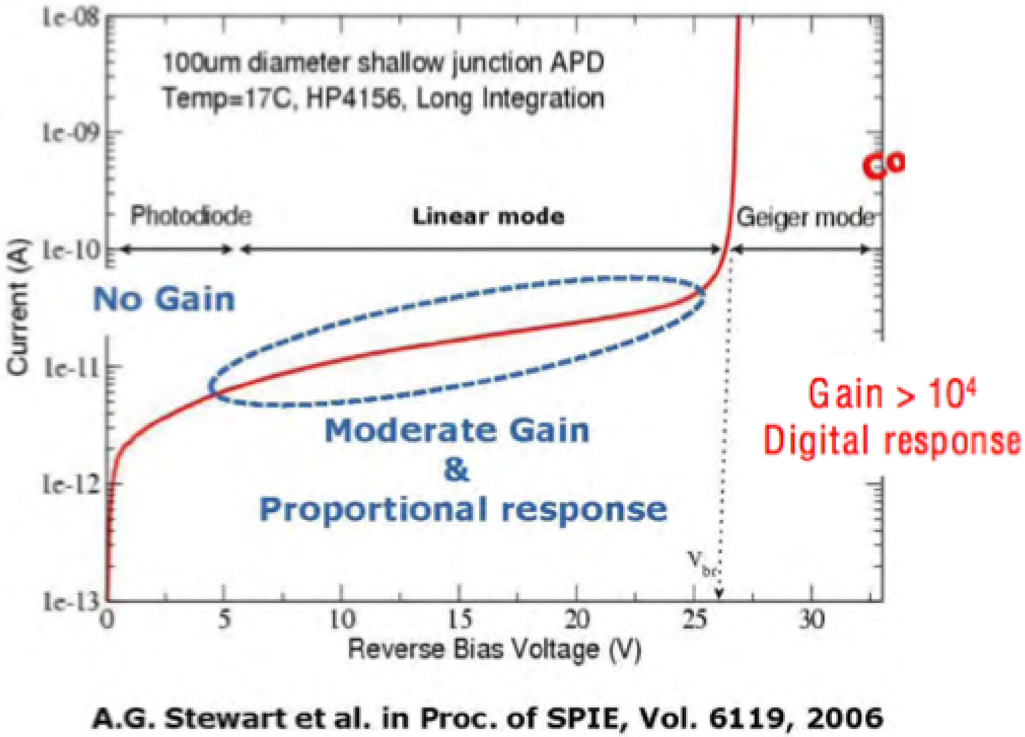

Figure 2.10: A plot to show the various stages of a sensor utilizing charge multiplication to enhance the signal. For our applications, great care must be taken not to exceed the breakdown field and enter Geiger mode. [32]

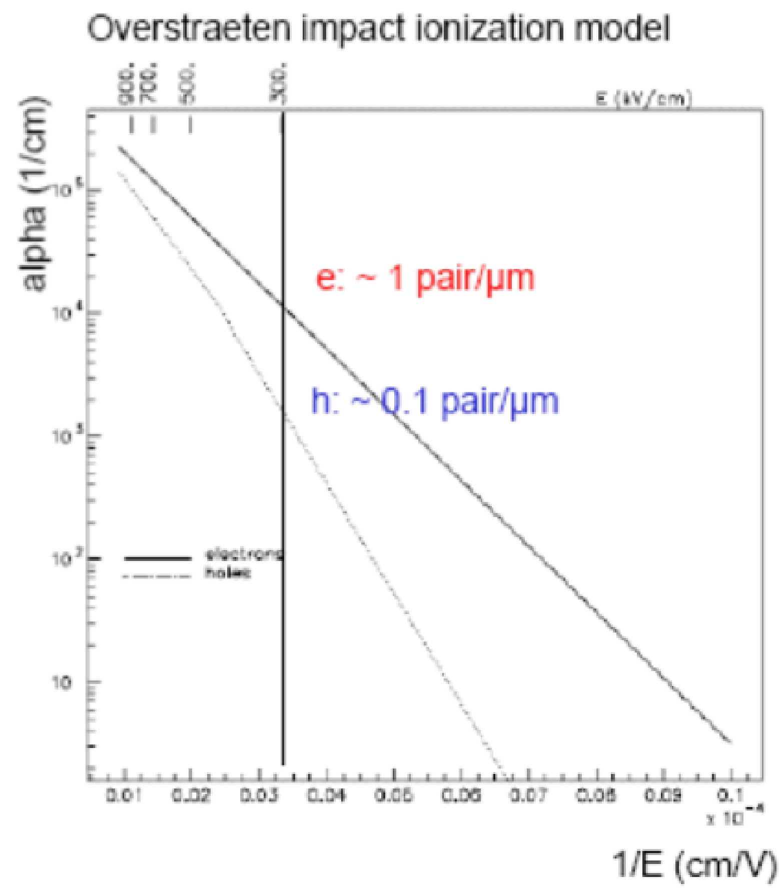

Figure 2.11: A plot of the ionization coefficient showing the strong dependence on the field. If the breakdown field in Si is around 300 kV/cm/cm, then α is close to 1 for electrons and 0.1 for holes. [30]

Naturally, the next relevant question is how to obtain such high operational fields inside silicon without extreme irradiation. Generally, the field increases with bias voltage but operation is only possible until breakdown threshold. Typical breakdown in planar sensors occurs around a small region near junction edges, preventing bulk fields from reaching values sufficient for ionization. This is shown in Fig. 2.12 where field lines are most dense near the junction at implant curvature. To combat this, several methods are suggested to aid in keeping fields uniform throughout. Deep diffusions and guard rings increase junction curvature and distribute field lines more evenly, as discussed in [3].

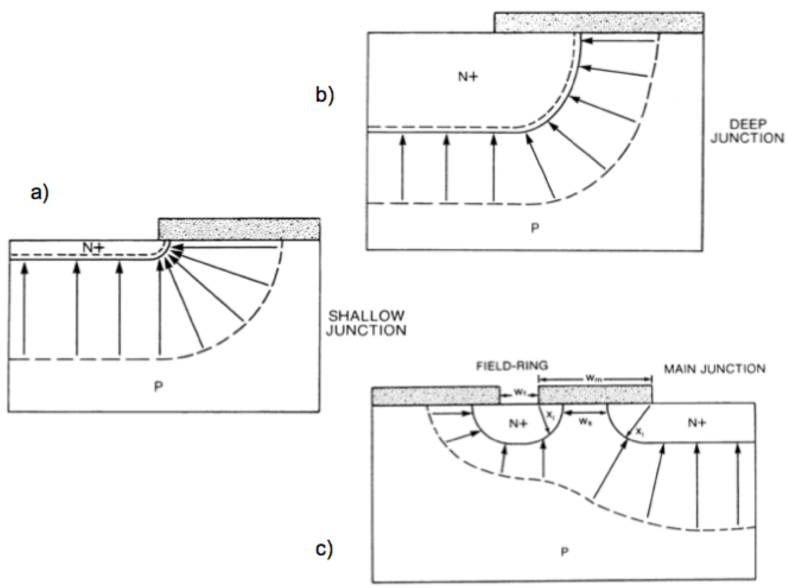

Figure 2.12: The density of field lines near the junction curvature in a) can lead to avalanche breakdown. Techniques to prevent this are shown here. In b) a deeper junction to increase field line spacing, and c) a field ring to distribute the field lines evenly. [3]

With breakdown fields around edges quenched, it is still necessary to have a high, uniform field providing a multiplication region that all mobile charges will pass through. A similar tactic for avalanche photodiodes is suggested in [3]. By implementing a “reach-through” doping scheme, shown in Fig.s 2.13 and 2.14, a suitable “avalanche” region is sustained in the device. In theory this technique can be very powerful but the author also warns that the process is hard to control precisely, resulting in varying gain and possible low yield.

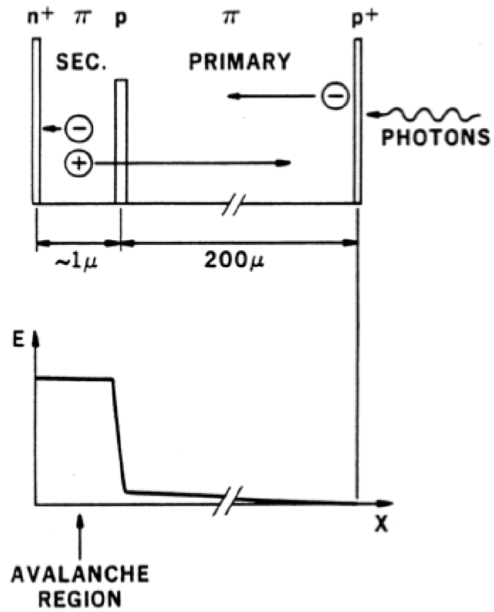

Figure 2.13: The author shows a theoretical doping scheme and the resulting field for an optimized multiplication region. The π symbol represents near intrinsic resistivity p-type silicon. [3]

The sensors studied in this thesis were made with a similar doping scheme and will be described in the next section.

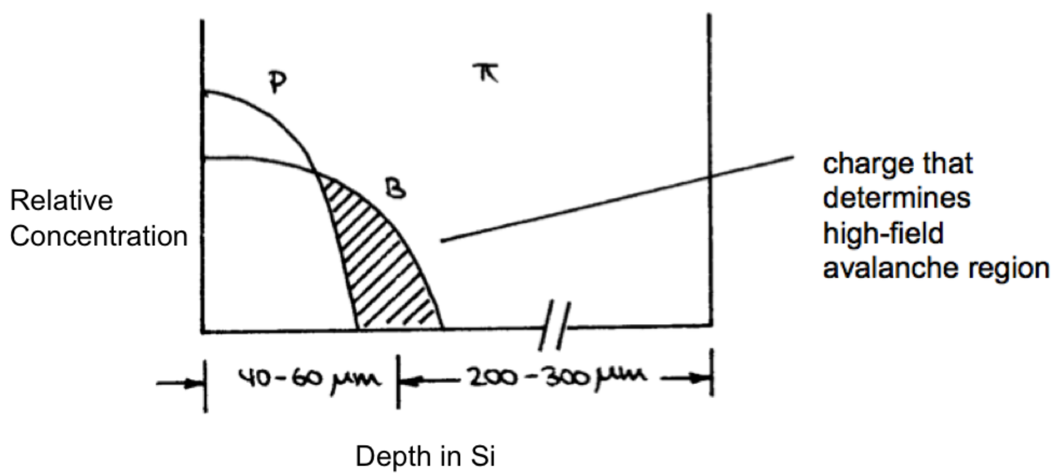

Figure 2.14: This double diffusion is a practical way to achieve a high field region. Commercially available avalanche photodiodes are fabricated in this simple manner [3].

3 Hardware for Data Acquisition

3.1 Sensors

The devices were manufactured by Pablo Fernández-Martínez at Centro Nacional de Microelectrónica (CNM) in Barcelona. The sensors are described in the slides presented in Fig. 3.1, credited to Pablo Fernndez-Martnez [26]. They measure 300 μm thick and close to 7 mm x 7 mm on the surface. The design follows the avalanche photodiode (APD) deep diffusion model, albeit with different parameters, and therefore is aptly named the low-gain avalanche diodes (LGAD). Sensor structure layout, linear doping profiles, and charge collection efficiency gain factor are all presented. We will verify these results, with our data discussed in the following sections.

There were two shipments of sensors from CNM after it was realized that sensors with high leakage current are not necessarily damaged and may actually exhibit various multiplication factors and thus be of great interest. The first shipment contained three devices; two with gain, "(W8-G11 and W8-I10)", and one without gain "(W9-E10)". These devices all have "low" currents ($< 1\,\mu$A) and were used for the transient current technique (TCT) measurements described below.

The next shipment contained a total of 18 devices, 15 from W7 and 3 from W8. Both wafers have the p+ deep diffusion, though with different doses (W7 had $1.6 \times 10^{13}\,\mathrm{cm}^{-2}$ and W8 had $2.0 \times 10^{13}\,\mathrm{cm}^{-2}$) [26]. These devices all have various levels of leakage current, a summary of which is listed in Fig. 3.2. Due to their recent arrival, these sensors have only been DC characterized and are currently being mounted for future TCT studies.

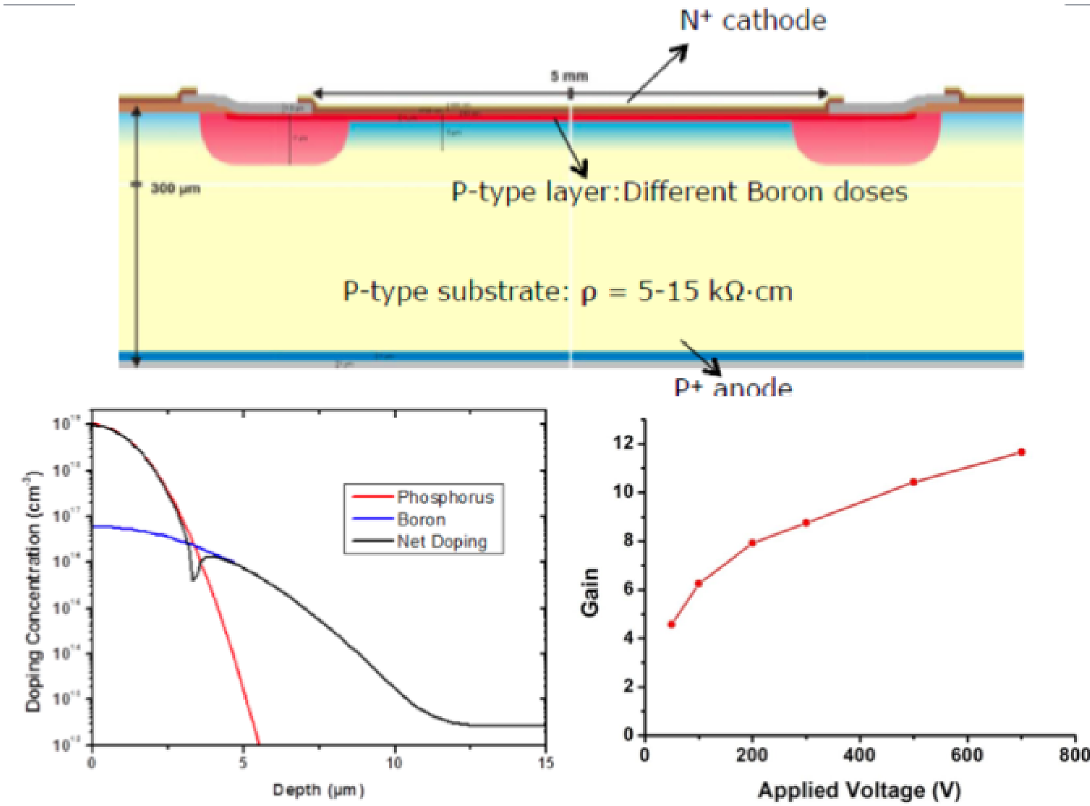

Figure 3.1: A cartoon showing a cross section of an LGAD device. The 1D doping profile vs. depth is shown for a line passing vertically through the central pad and p+ deep diffusion. At the junction the net doping dips because the concentration of donor and acceptor states are equal. The gain factor is shown from alpha TCT measurements compared between a device with p+ diffusion and a device without. [26]

3.2 Measurement Procedures

The majority of tests consist of bias current vs. voltage (IV), capacitance vs. voltage (CV), and transient current (TCT) measurements.

Bias current measurements are performed with Keithley 237 and 2410 series high voltage power supplies. Electrical contact between top surface implant and aluminum backplane is provided through DCM 210 series micro-positioning probes made by Cascade Microtech. A picture of the setup is shown in Fig. 3.3. The process is controlled by the automated data acquisition program (ADAP), which is documented at `http://www.adap.ucsc.edu`. Capacitance measurements are recorded in a similar manner with the aid of the Agilent E4980A Precision LCR meter. Small signals are injected at a frequency of 10 kHz.

Devices sent to UCSC/SCIPP

Wafer 7

Sample	Current Range	Type*	Comments
K7	< 1 μA	SC	-
I2	< 1 μA	DC	VBD < 950 V (Diced)
I9	1-10 μA	SC	-
C8	1-10 μA	DC	-
F10	1-10 μA	DR	-
I7	10-100 μA	SC	-
D9	10-100 μA	SR	-
H9	10-100 μA	SR	-
I4	10-100 μA	DC	-
K4	10-100 μA	DC	I < 1 μA (On Wafer)
D4	10-100 μA	DR	-
F2	10-100 μA	DR	VBD < 800 (Diced)
H4	10-100 μA	DR	-
J8	10-100 μA	DR	-
H7	> 100 μA	SR	I ~ 200 μA

****Type: SC → Devices without ring and with circular window in the cathode metallization.***
DC → Devices with ring, and with circular window in the cathode metallization.
SR → Devices without ring and with square window in the cathode metallization.
DR → Devices with ring and with square window in the cathode metallization.

Wafer 8

Sample	Current Range	Type*	Comments
C9	1-10 μA	SC	-
I9	1-10 μA	SC	-
C8	1-10 μA	DC	-

Figure 3.2: Properties of sensors from the second shipment from CNM containing "high" currents. Note only 2 devices breakdown at bias voltages below 1000V.

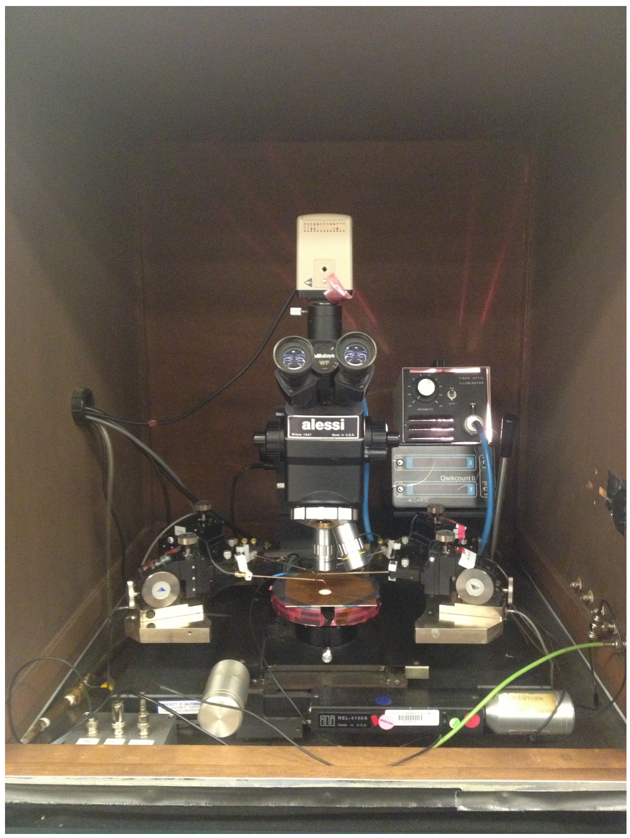

Figure 3.3: A picture of the probe station used for IV and CV general measurements

Sensors are further characterized by the transient current technique (TCT), in which some form of radiation is incident, and the ionized charge is read out as a burst of current that decays quickly. The resultant current has a characteristic waveform that can be analyzed to show various features of the multiplication process.

The TCT measurements are performed in a light-tight, G10 plated box, shown in Fig. 3.4. Sensors are bonded to a small section of PCB to allow electrical contacts. The top of the diodes are wire bonded to a readout node which is AC coupled to a coaxial SMA transmission line. Depending on the method, the current may or may not be amplified by a MiniCircuits ZX60-6013E-S+ series amplifier with 15dB gain, 20 - 6000 MHz bandwidth, and SMA connection. The signal is then terminated in a 50 Ohm Tektronix high precision scope with 2.5 GHz upper frequency bandpass.

Figure 3.4: A picture of the TCT box used for illumination by alpha particles

Americium-241 smoke detector sources provide the alpha radiation. A retractable stand allows illumination from the top and bottom of the sensor, with the alpha source never more than 1 cm from the target. Amplification may or may not be necessary depending on test settings. Equivalent circuit diagrams for TCT measurements are shown in Fig. 3.5.

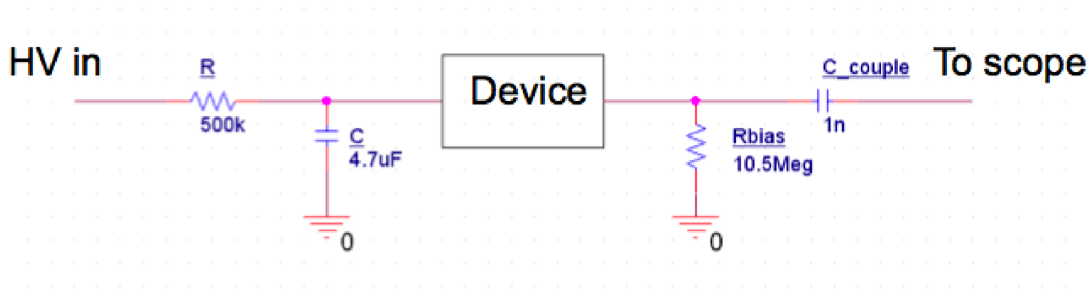

Figure 3.5: The circuit diagram for the TCT measurements is shown here. The RC network on the left is the HV lowpass filter. The components shown on the right act as a bias resistor and decoupling capacitor.

4 Simulations

Device modeling and simulation are performed using commercially available technology computer aided design (TCAD) tools. Several corporations offer such products but the one employed here is written by Synopys and dubbed Sentaurus TCAD tools for semiconductor processing. The scope of the software is enormous and only brief descriptions are provided in this thesis. For more information, see Appendix A and the Synopsys website [29].

4.1 Sentaurus TCAD

Since the mid 1970's engineers have been modeling devices using TCAD technology for semiconductors [34]. TCAD has developed tremendously since the days of 1D bipolar junction models, and today it is capable of simulating almost any practical physical situation. Despite the enormous leap in processing power and structure complexity, the underlying computational method remains the same. The method consists of defining the model of interest, discretizing that model into many small cells, and solving numerically the relevant differential equations. This technique is called finite element analysis and the process flow is shown in Fig. 4.1.

4.2 PSPICE

The student version of PSPICE (Personal Simulation Program with Integrated Circuit Emphasis) version 16.6.0 was used to analyze the readout circuit for the TCT measurements.

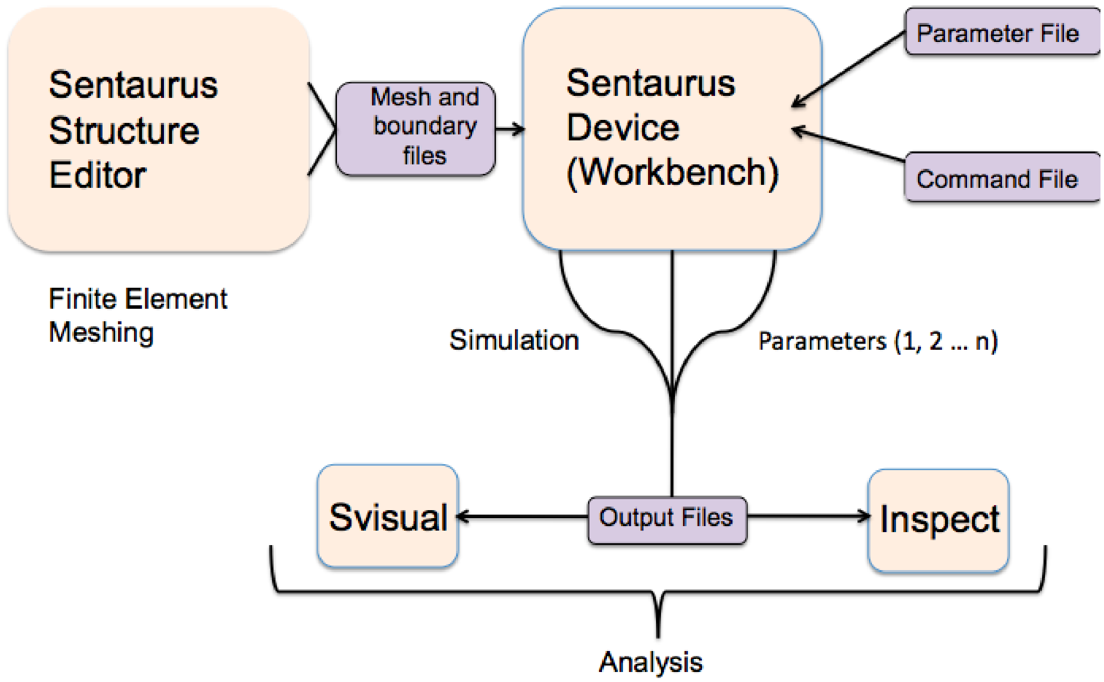

Figure 4.1: A diagram of the data and process flow in Sentaurus TCAD. The three main steps are shown: Design a model, run the simulation with correct parameters, and analyze the output.

Used to numerically analyze circuit networks, PSPICE has been in development since its conception at the University of California, Berkeley in 1973 [35]. In our case, we simply define a current pulse with parameters similar to what we might expect from an LGAD, and watch how it moves through the circuit and what signal appears across the oscilloscope. A screenshot is shown in Fig. 3.5.

5 Results

5.1 Simulation of a Simple Diode

5.1.1 DC

The first data presented are the simulation results for a simple n++ / p / p++ pad diode. It measures 160 μm wide by 300 μm thick, and bulk resistivity is 15 kΩ/cm. These simulations are performed to illustrate the scope of the software and to ensure that the toy model gives reliable results. The device is shown in Fig. 5.1 and the important parts are labeled. The IV curve is shown in Fig. 5.2 and its features exhibit good behavior, as there is no avalanche breakdown up to a bias voltage of 1000V. The CV curve is also shown in Fig. 5.2 and the full depletion voltage is extracted and compared with the following calculation, from the equation in [3].

$$\begin{aligned} V_{fd} &= \frac{qN_{eff}}{2\epsilon} w^2 \\ V_{fd} &= \frac{(1.6 \times 10^{-19} C)(1 \times 10^{12} cm^{-3})}{(2)(11.7 \times 8.85 \times 10^{-14} \frac{C}{V \times cm})} \times (.03cm)^2 \\ V_{fd} &\approx 70V \end{aligned} \tag{5.1}$$

N_{eff} in the equation above refers to bulk doping concentration, q is the electron charge, w is the thickness of the sensor, and ϵ is the electric permittivity of silicon.

The $1/C^2$ curve extracted from the simulation output shows a plateau at very nearly 70V, which demonstrates software reliability in the toy model.

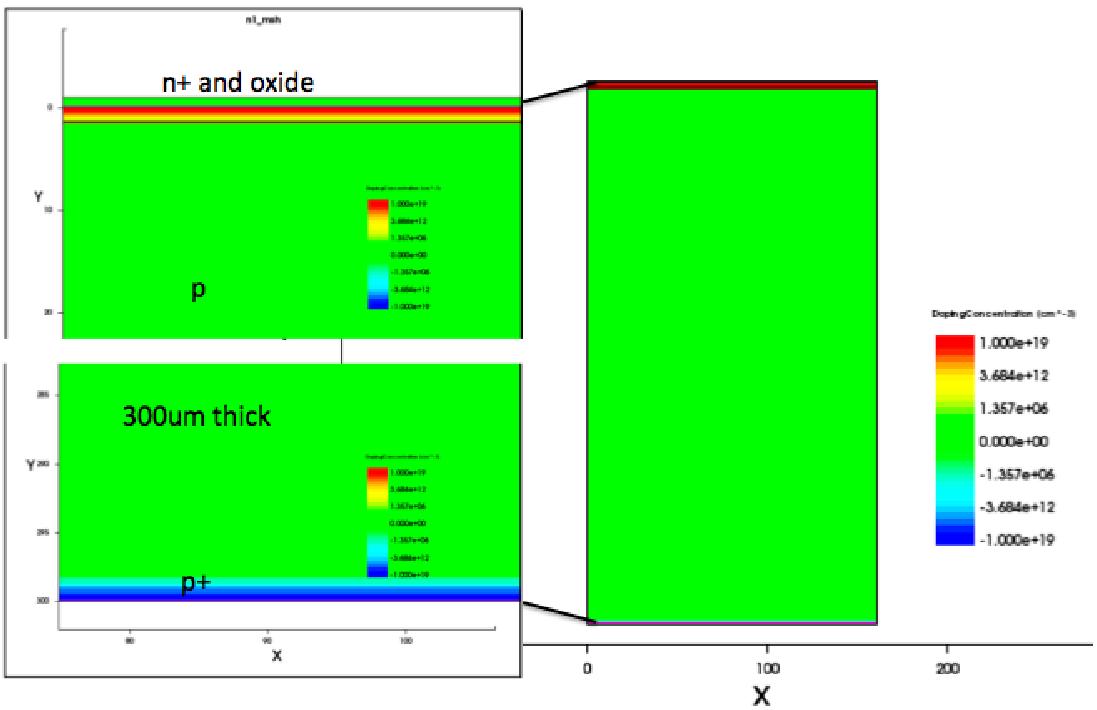

Figure 5.1: The simple diode structure. The device measures 160 μm wide by 300 μm thick and is used to study DC and dynamic signal stimulus.

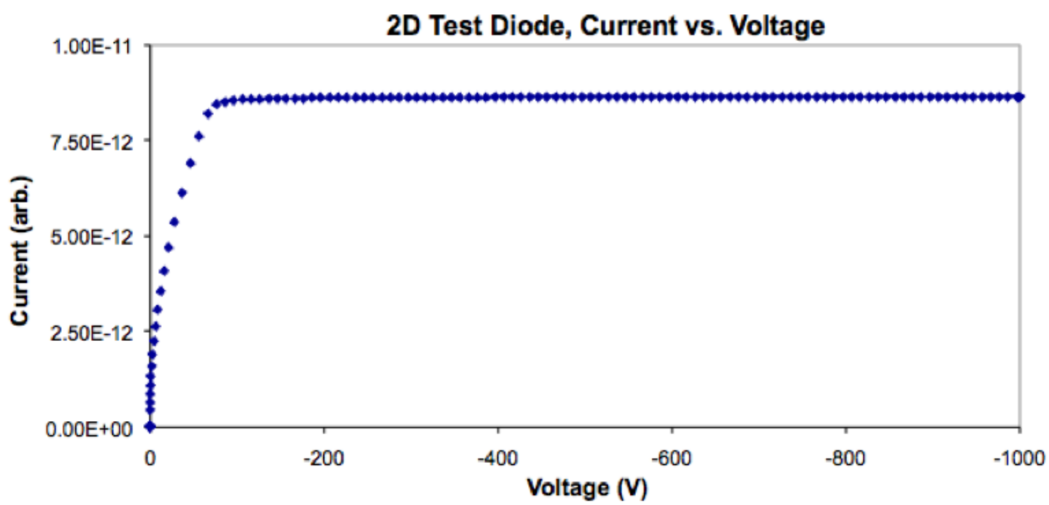

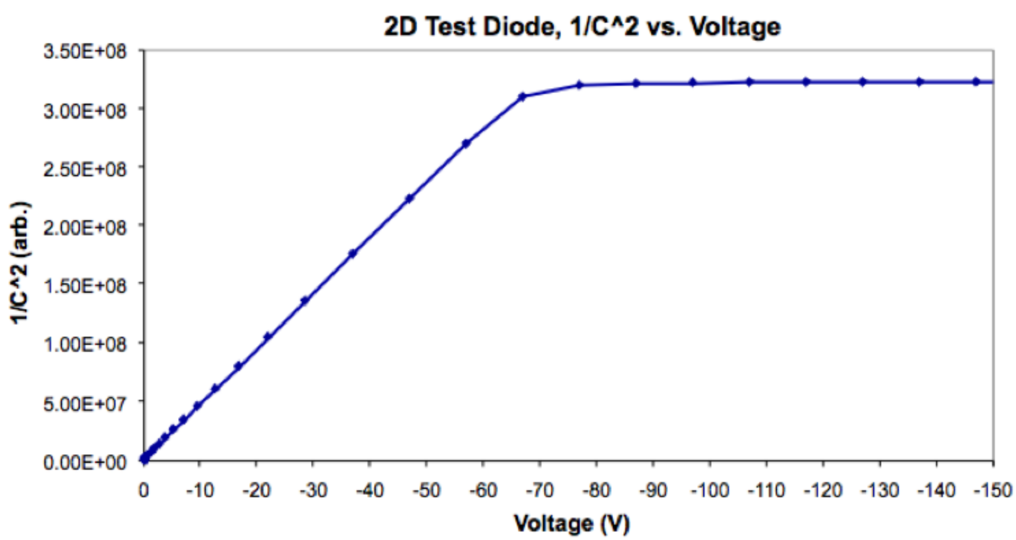

Figure 5.2: Simulation output for simple diode IV and CV curves are sensible results. No breakdown is observed for bias voltages up to 1000V. Depletion occurs around 70V.

5.1.2 Transient Analysis

Since the DC simulations appear reasonable, the next step is to observe the transient current from incident radiation. A MIP is simulated is simulated by a heavy ion traveling all the way through a diode and liberating 80 electron-hole pairs per micron of silicon. We display the charge density at the moment of impact in Fig. 5.3.

The simulation is run at 20V, 200V, and 2000V to show the effect of electric field strength on carrier dynamics. The collection time, shown in Fig. 5.4, is a strong function of field as expected. A current plot vs. time is shown in Fig. 5.5 for different bias voltages, and in Fig. 5.6 for opposite collection electrodes. Additionally, the time-evolution of the current is shown as a grid of contour plots in Fig. 5.7. Each successive tile represents a snapshot at a later time of the time evolution in the sensor. The key to reading the evolutional plot is shown in Table 5.1.

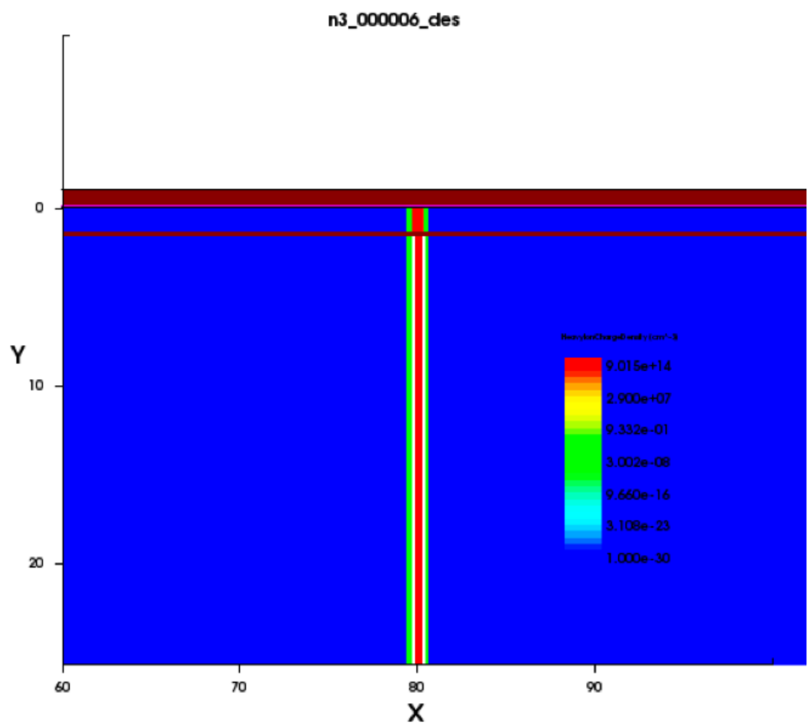

Figure 5.3: The initial charge distribution from a traversing MIP in the simple diode model. Distribution extends 300 μm to the bottom of the device with minimal Bragg peak, consistent with a uniform charge density.

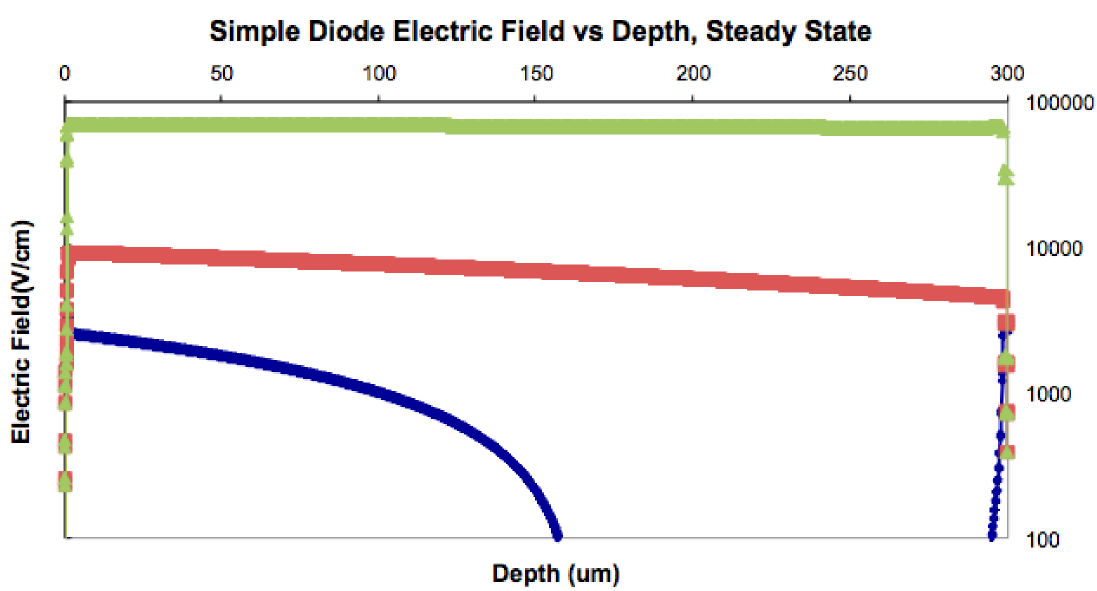

Figure 5.4: A plot showing the difference in electric field strength for the different bias voltages used in MIP transient analysis.

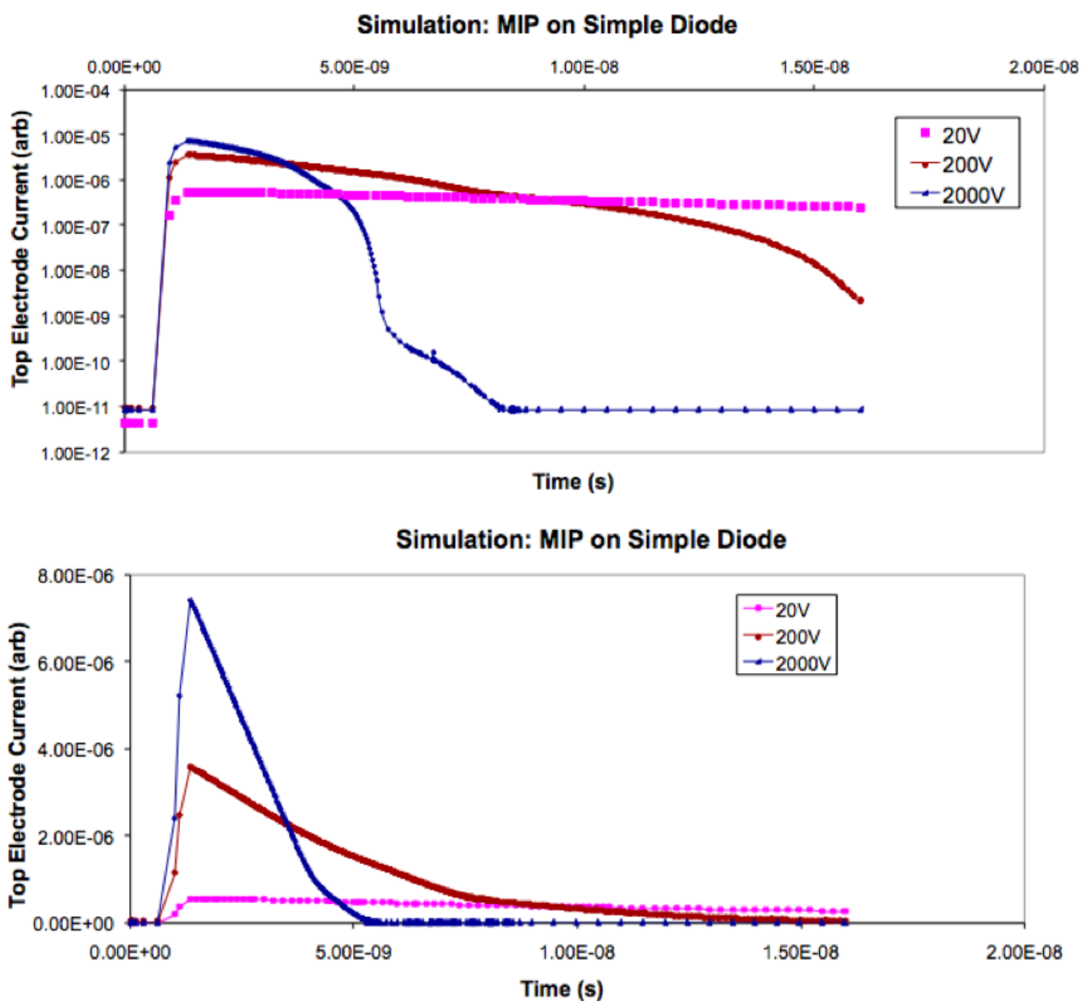

Figure 5.5: Dynamic current vs. time stimulated by MIP in the simple diode. The integral of the current yields equal charge within 1 percent for 200V and 2000V biases. The 20V case suffers from incomplete depletion and ballistic deficit.

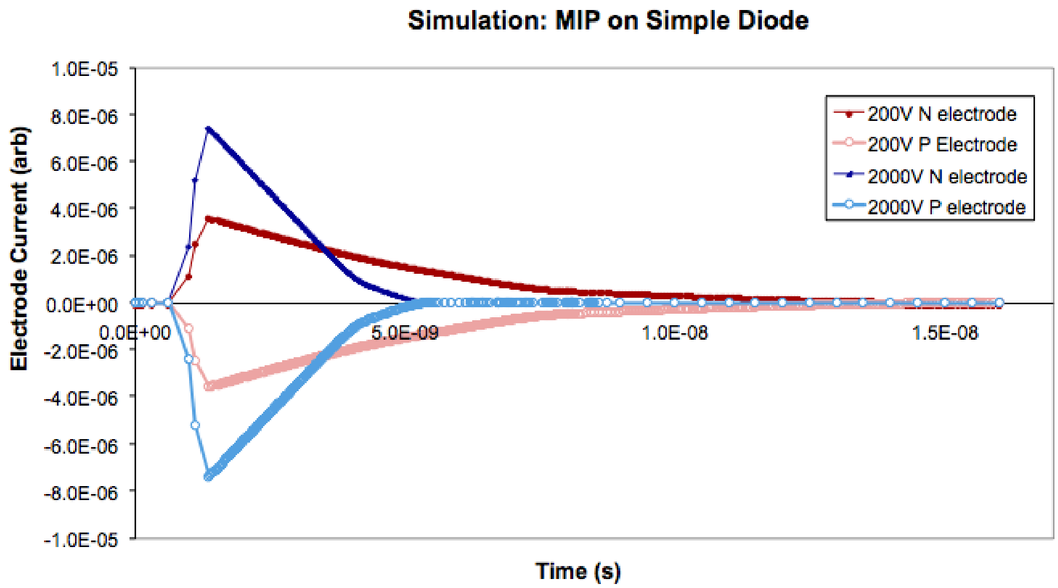

Figure 5.6: N vs. P electrode total current vs. time for the simple diode after incident MIP. These are verified to be equal and opposite, satisfying the continuity equation for electrons and holes.

Time (ns)		
0	1	2
3	5	7
9	12	15

Table 5.1: This table is the key to the 9-tile "evolution plots." The quantity under study is evaluated at the time stamp corresponding to its placement on this grid.

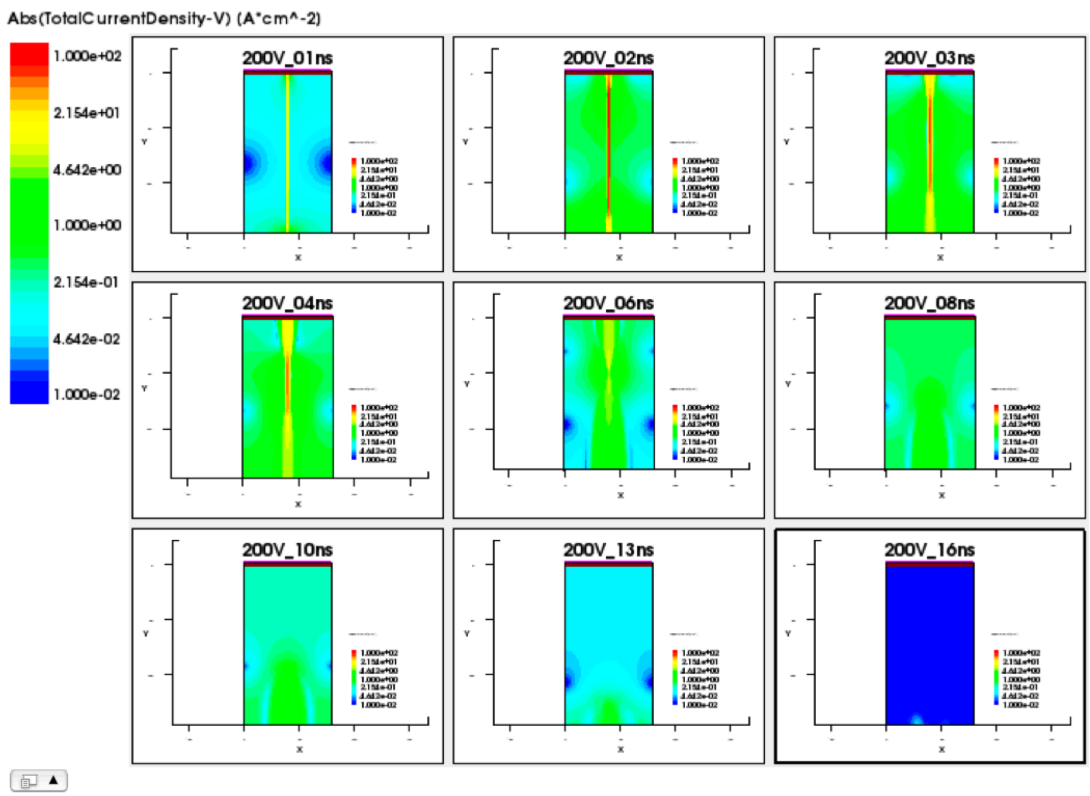

Figure 5.7: 2D plot of the total current evolution in the simple diode after incident MIP for a bias voltage of 200V. Each tile represents a different time slice following the key in Table 5.1. Vbias = 200V

There are several important lessons to be taken from these simple simulations. First the total currents read on opposite electrodes are concluded to be equal and opposite, verifying the continuity equation. Next, carrier collection time is observed to vary with bias voltage, as would be expected from the field profiles. Though the current vs. time curve is different for each bias voltage, the integrated total charge seen by each electrode is the same within 1% for 200V and 2000V bias. The 20V case is subject to incomplete depletion and the virtual version of ballistic deficit, where the transient analysis is only run to 15 ns after impact and charges are still drifting and diffusing in the weak field.

As is visible in the electric field evolution plot in Fig. 5.8, the presence of ionized mobile charges evokes a momentary undepleted region. The charges alter the local electric field and may contribute to charge screening. Figure 5.9 shows the electric field vs. depth at different times in the 200V biased simple diode as charge from a MIP is swept to the electrodes. Additional time-evolution plots of charge and current densities at various settings are shown in Appendix B. This effect is significant when considering short collection times, as screened charges tend not to drift as fast as unscreened ones. After some time the steady state field is reestablished. A cartoon illustrating the field dynamics is shown in Fig. 5.10.

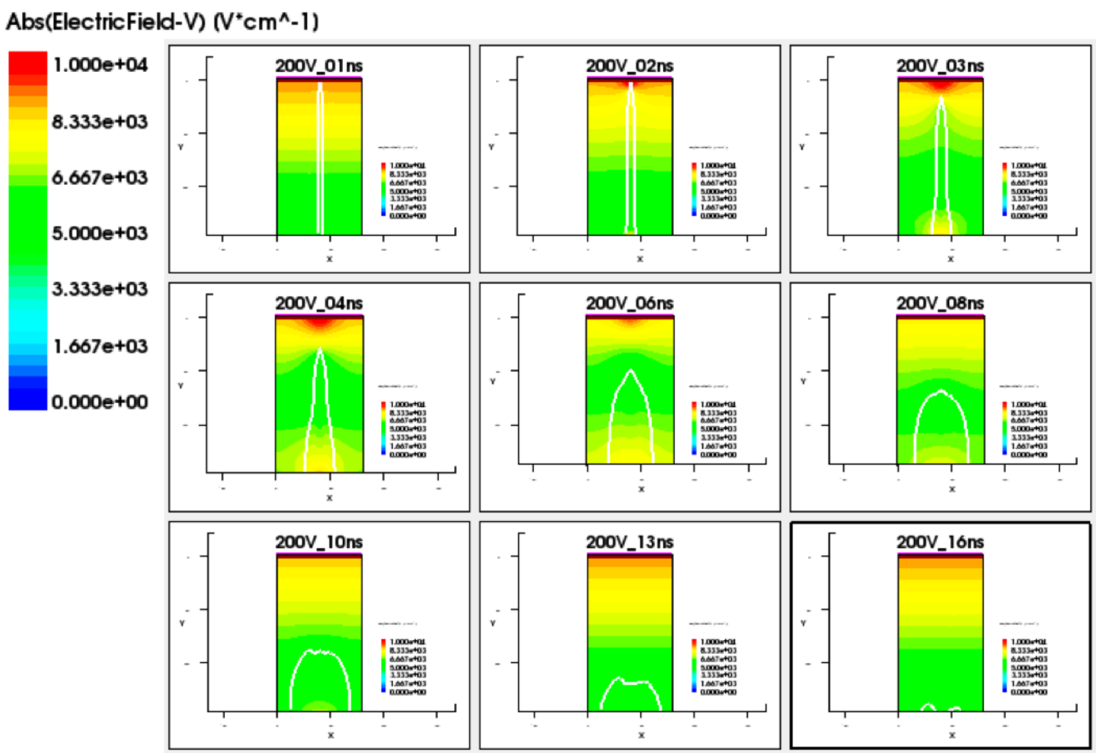

Figure 5.8: A 2D plot of how mobile charge affects the local electric field after a MIP crossing.

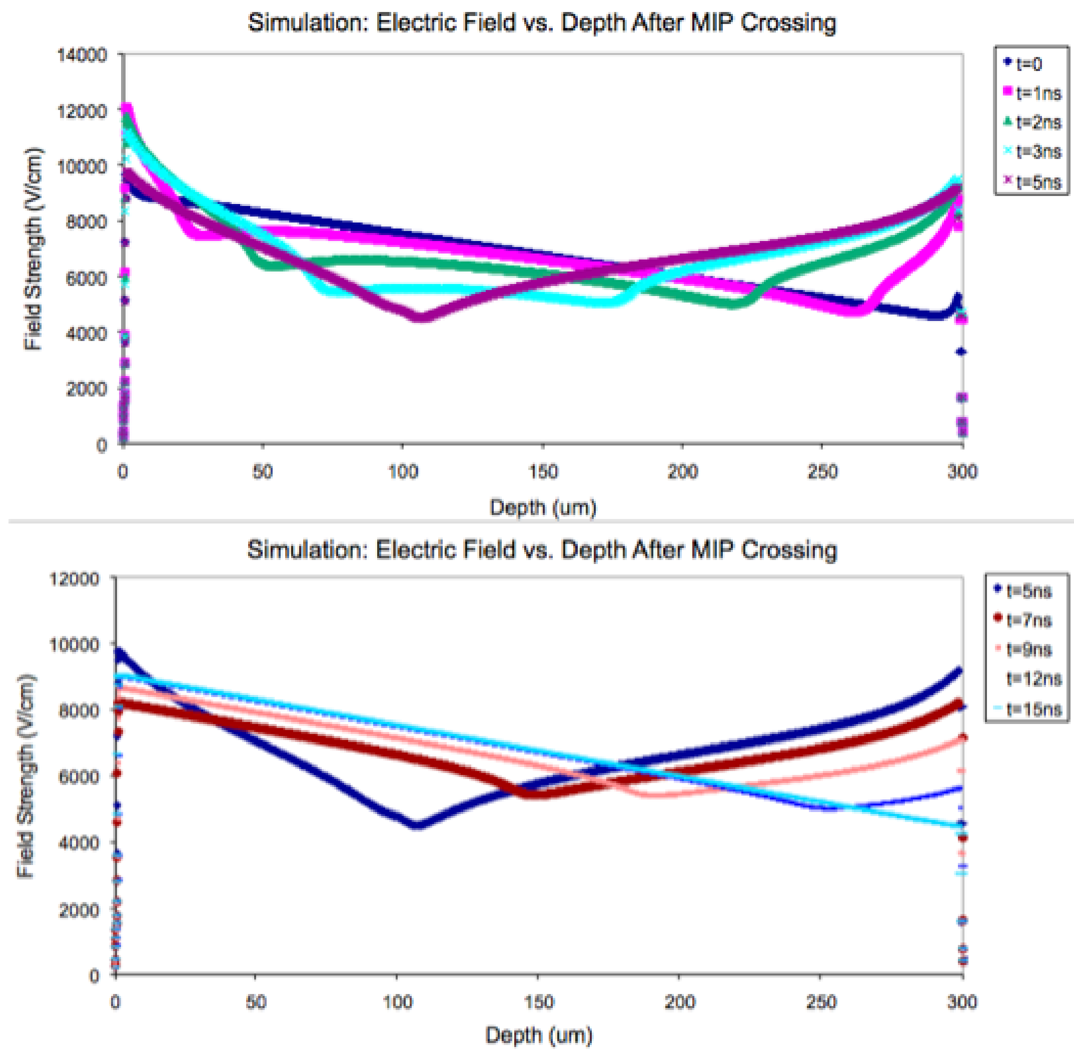

Figure 5.9: A 1D plot of how mobile charge affects the local electric field after a MIP crossing. The electric field orthogonal to the electrodes is plotted here vs. depth for different time slices.

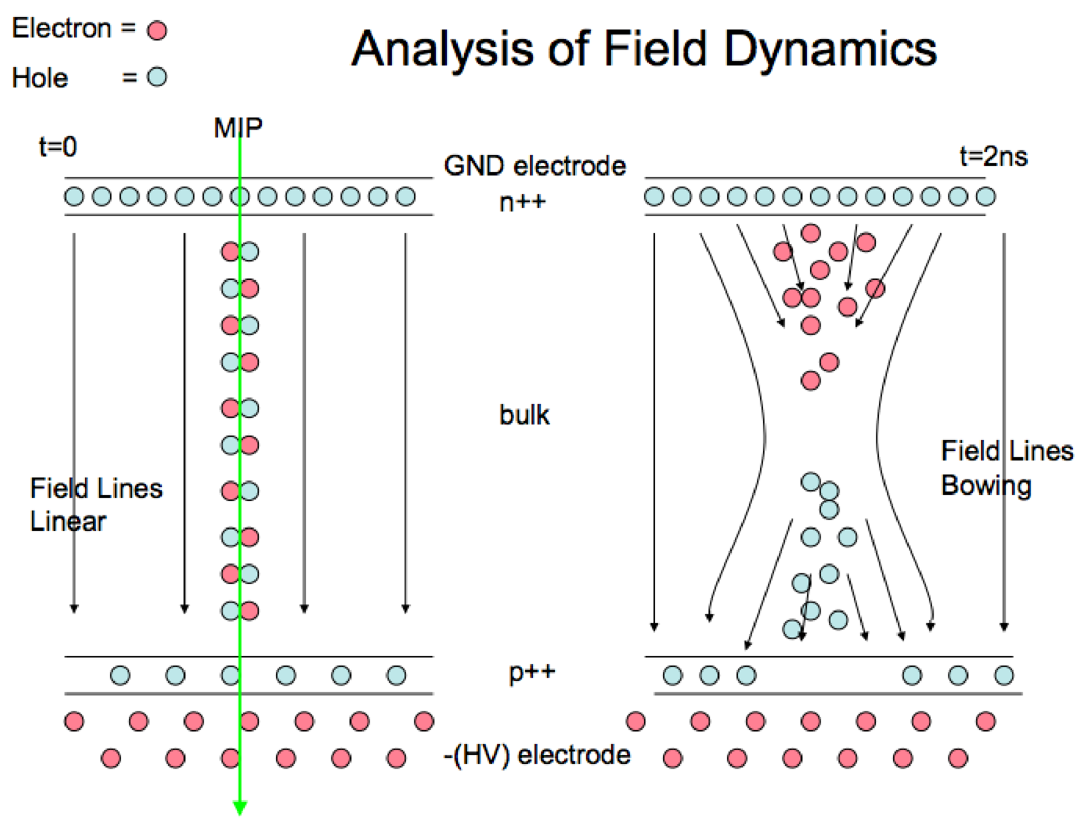

Figure 5.10: A cartoon of a cross section of a sensor. The carrier dynamics alter the steady state electric field. The effect is quantified in the Figs. 5.8 and 5.9 above.

5.2 The LGAD Structure

5.2.1 DC Measurements

Upon receiving the LGAD samples from CNM, we tested IV and CV behaviors for samples from wafers 7, 8, and 9 in the manner described in Section 3.2 above. First shipment data are shown in Fig. 5.11. Interesting features appear in the form of curve kinks in both the IV and CV data. It may be that these kinks can be explained by the additional device structures, namely the collector ring and the p+ diffusion.

Another important feature revealed by the DC measurements is the variation in leakage current for different samples. Figure 5.12 shows that devices range between a few 100's of nA to a few 100's of μA between samples taken from the same wafer. Since the leakage current is expected to undergo some multiplication as well, this might point to a variation in effective p+ deep diffusion concentration. For this reason, the "good" devices, or those with leakage current less than 1 μA, were distributed first. Several months later, it was realized that devices with high leakage current may be of great interest due to large gain factors compared to those with low leakage current, especially considering the excellent breakdown performance of nearly all samples. A map showing the distribution of "good" and "bad" sensors from [36] is shown in Fig. 5.13.

It is clear from Fig. 5.14 that the agreement in CV data between institutions is not ideal. In addition, the curves show wide variations between samples, not like the IV curves, which have a kink at essentially the same point on the curve. It is not understood why this is so as of yet, but we can look for correlations in the currents and the geometries. The results are presented in Appendix C. From those plots it seems that leakage current level has little effect on the CV trends, and the collector ring presence seems to alter the final capacitance slightly, though no other obvious correlations are observed. We will investigate possible causes of CV variation in the simulation section below.

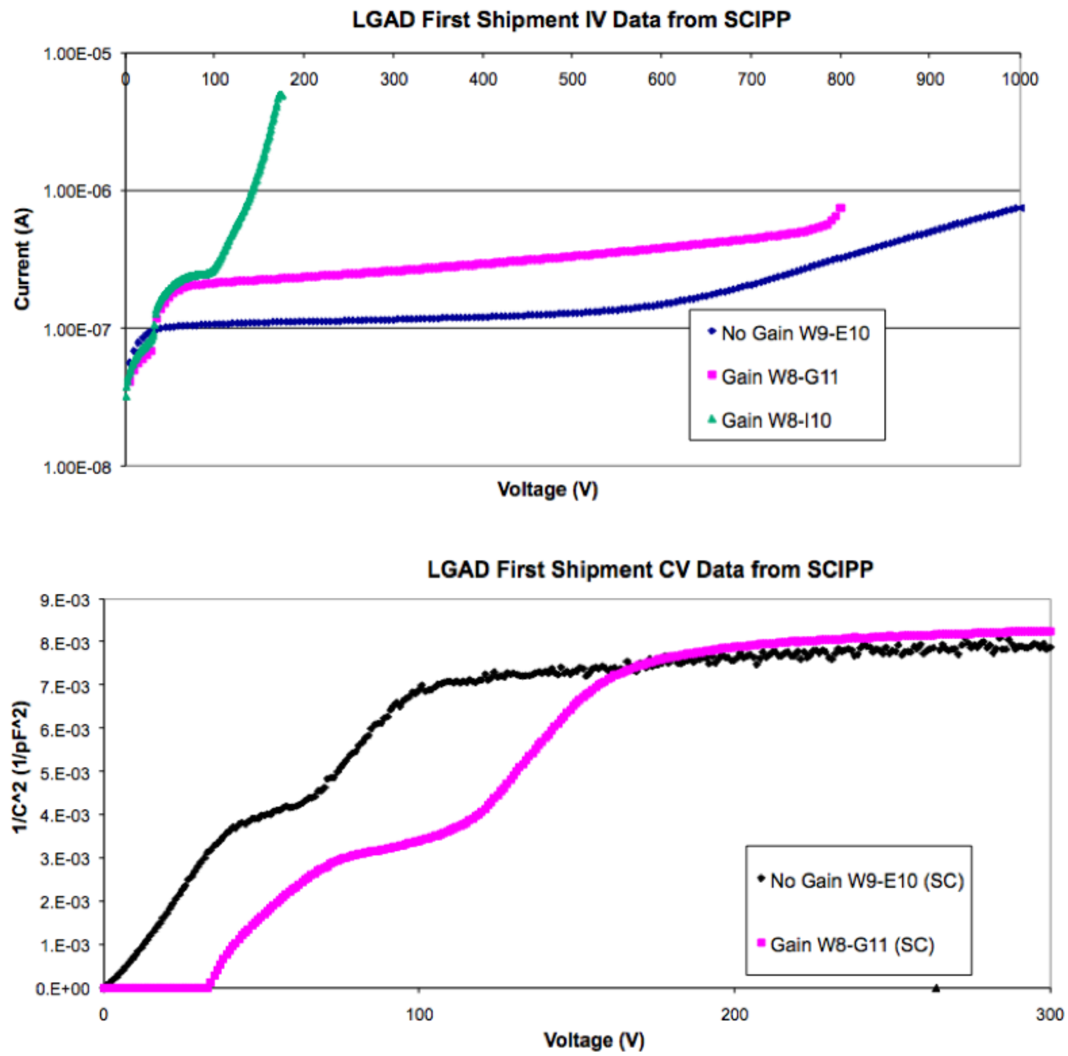

Figure 5.11: The DC results for the "good" sensors received from the first CNM shipment.

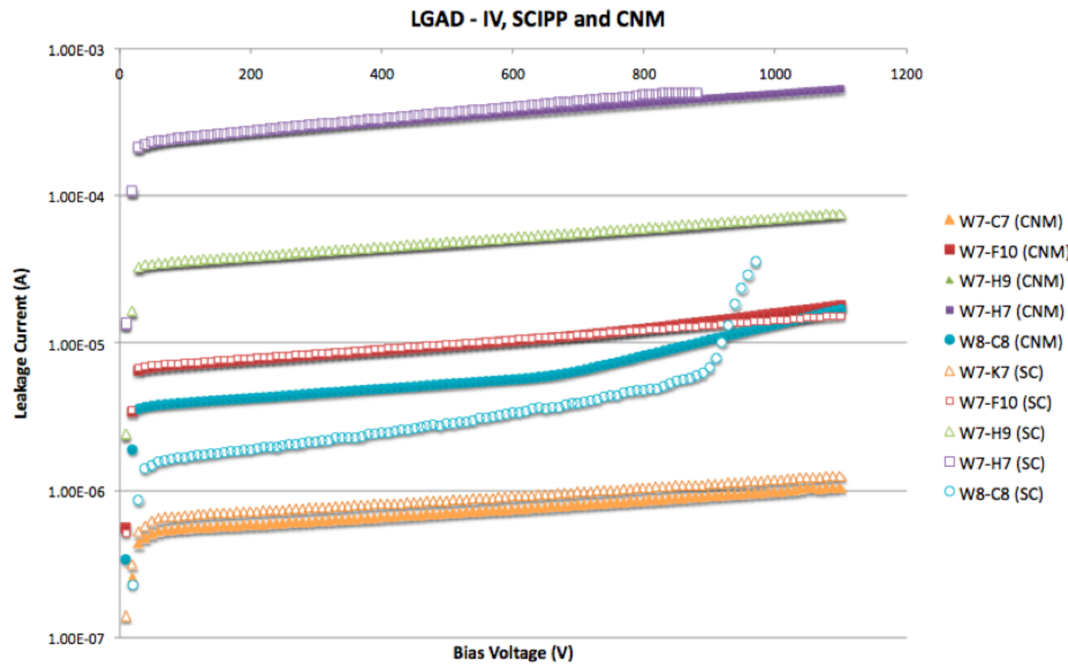

Figure 5.12: The IV results for the second CNM shipment containing "bad" sensors. The agreement between measurements done at CNM and SCIPP is quite good, suggesting shipping was not overly traumatic.

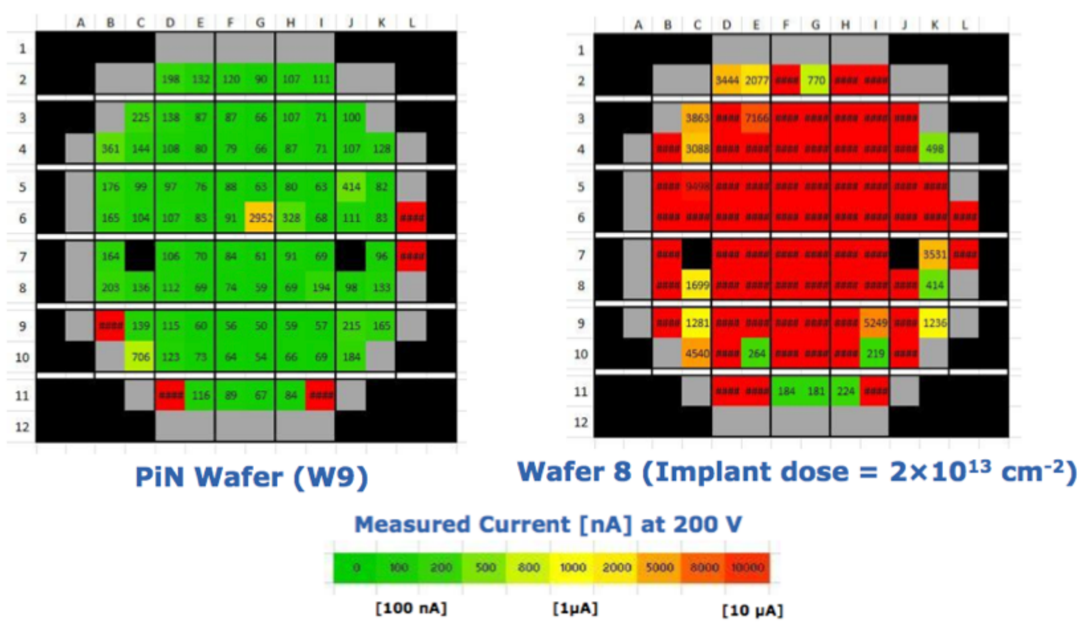

Figure 5.13: CNM's yield map for 2 LGAD wafers, one with p+ diffusion (gain region) and one without (no gain region). Stark differences in leakage current are present between wafers. [36].

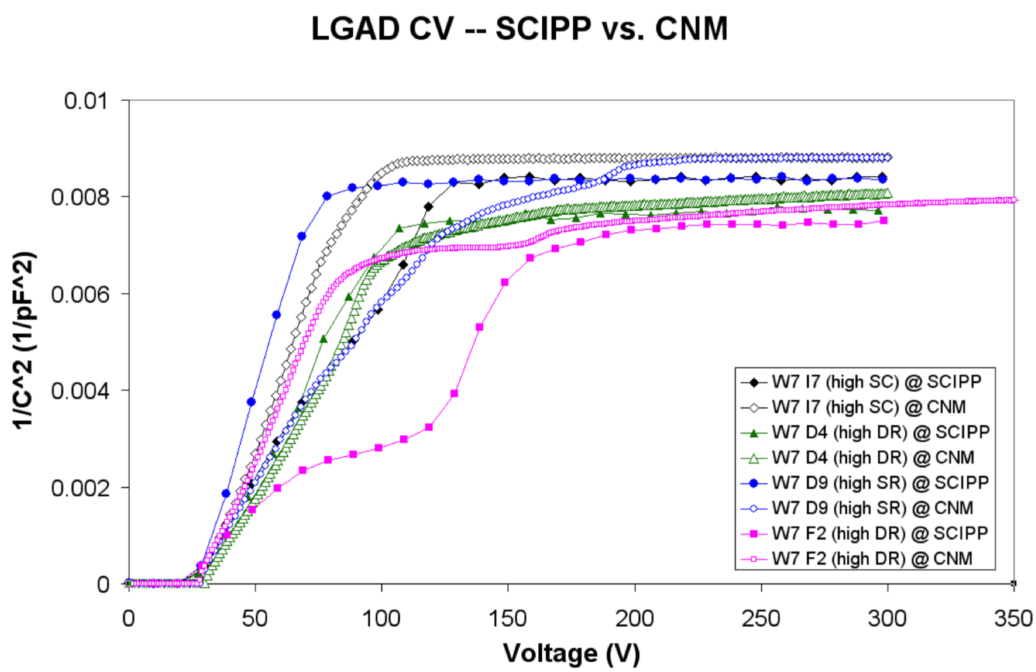

Figure 5.14: A comparison of the CV results between SCIPP and CNM Barcelona. Results are plotted for sensors with "high" leakage currents and various geometries. Significant variation is present between different samples and runs at different testing sites.

5.2.2 DC Simulations

IV and CV

To more deeply investigate the properties of the LGAD structure, a model based on the region specifications from CNM was simulated and analyzed. The main features of the structure are shown in Fig. 5.15. Two versions of the simulation were analyzed, one full 2D slice of a device with full 5mm gain region, and one unit cell containing one channel and 240um of the gain region. The doping concentrations follow the specifications shown in Fig. 3.1. AC analysis is performed at 10 kHz, the same frequency as the real data. Important parameters in DC characterization include p+ deep diffusion dose, P-spray concentration, and Si02-Si interface charge.

The simulation verifies the kink in the IV curve, shown in Fig. 5.16. The explanation follows from examination of the depletion region before and after the kink. Because the p+ deep diffusion region is significantly more doped than the p bulk, it depletes at a slower rate with respect to bias voltage. However, since it is thin and the doping gradient is steep, the deep diffusion region does fully deplete at the point where the kink occurs and the remaining high resistivity bulk depletes much faster. Note that with no p+ deep diffusion no kink is observed, reinforcing the hypothesis. Further verification comes when the p+ deep diffusion

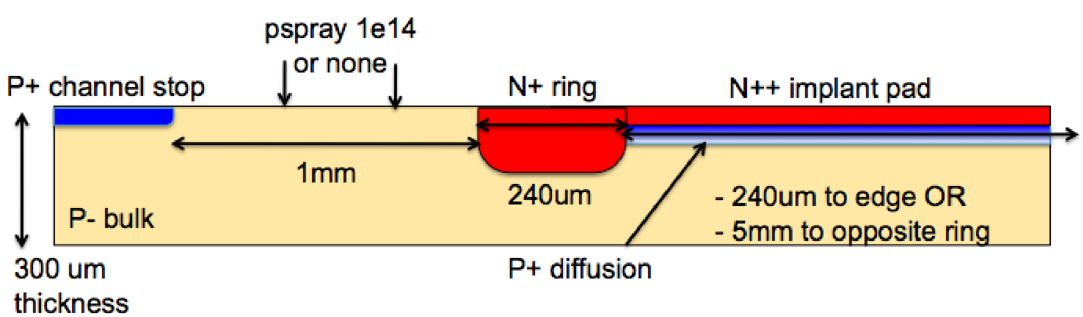

Figure 5.15: A diagram showing the important features of the LGAD device. This contains all regions in the unit cell for the small device simulation, with the larger full slice extending the gain region 5mm to the opposite channel.

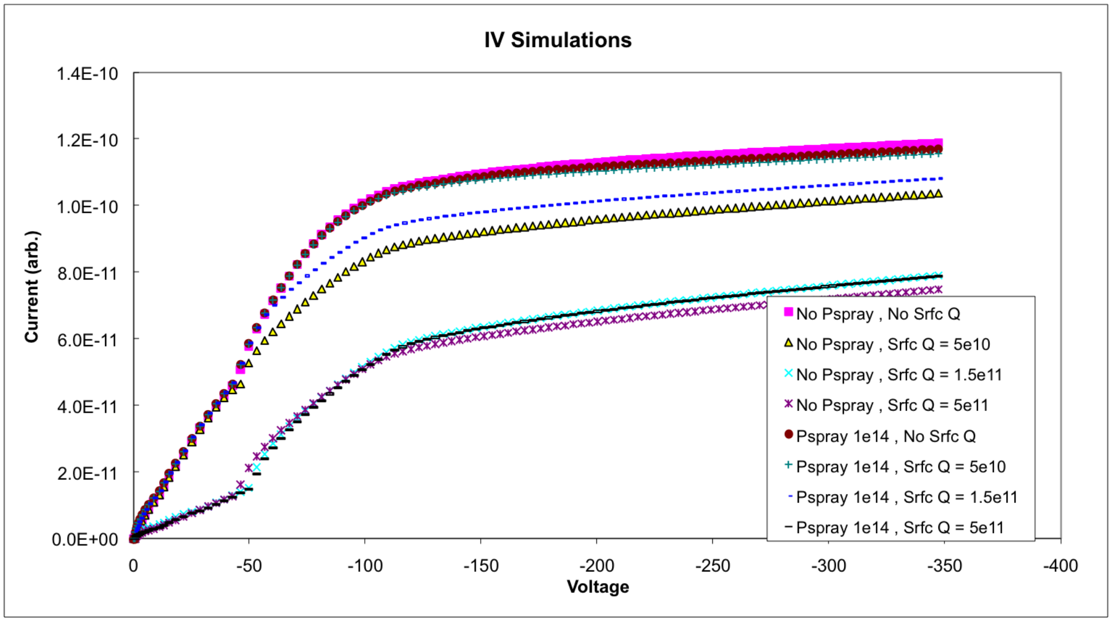

Figure 5.16: The IV curves for the simulated LGAD model. Note there is not as much variation between current levels as in the data. The kink does appear in the simulation as well.

peak concentration is varied. In these cases the kinks in the IVs and CVs move appropriately higher or lower based on the doping density, shown in Fig. 5.18.

The P-spray and surface charge concentrations have only a small effect on the simulated IV curves. A before and after view of the depletion transition is shown in Fig. 5.17.

CV data are more difficult to understand, as they seem to have no recognizable patterns from Fig. 5.14, and the additional comparisons in Appendix C. The first clue to understanding the behavior came with including the Si02-Si interface recombination in the simulation's physical models. There is a clear difference between simulations with and without this physical model, visible in Fig. 5.19. This suggests that surface effects could be important. This hypothesis was reinforced when surface charge and p-spray were varied, and two distinct capacitance plateaus appear. As these data in Fig. 5.20 shows, some curves exhibit a transition from high to low capacitance at a certain bias voltage. To investigate this effect further we examine the depletion region in the device with a limited gain region.

We examine the 2D structure slice at a bias voltage of 350V for the two opposite

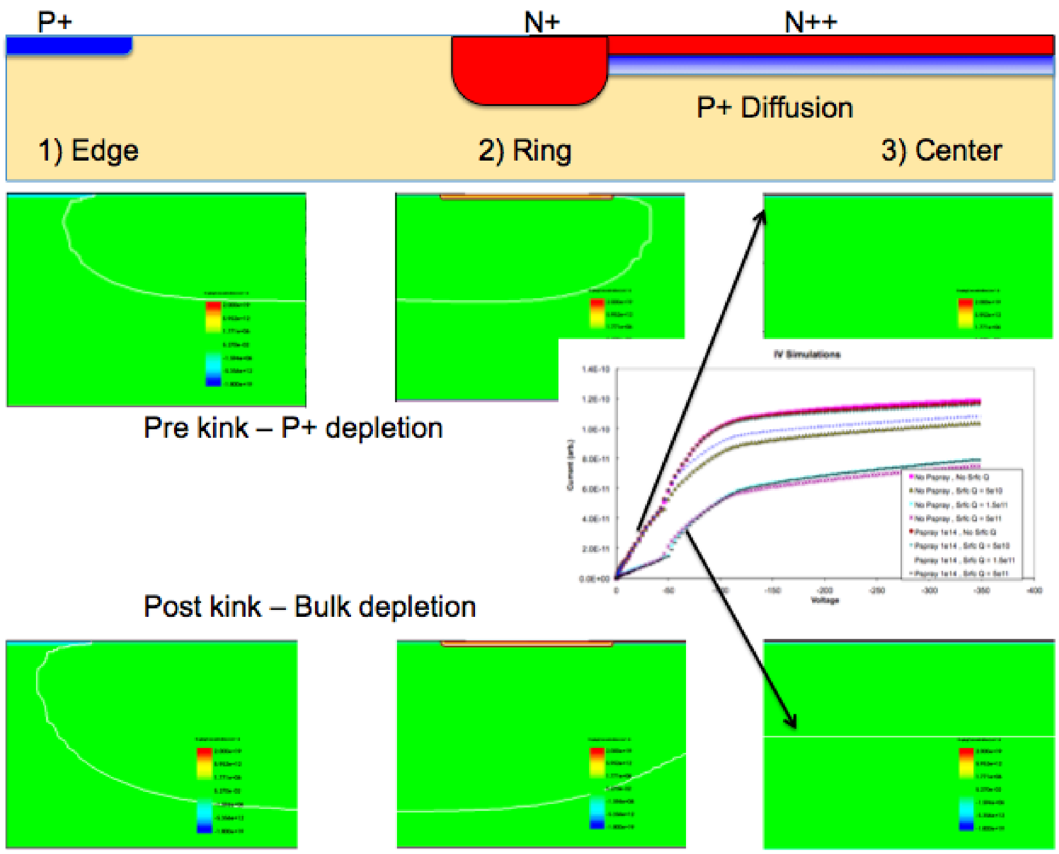

Figure 5.17: An explanation of the kink in the IV curves. The simulation shows a transition from depleting the p+ deep diffusion to depleting the bulk. (Depletion region outline shown in white)

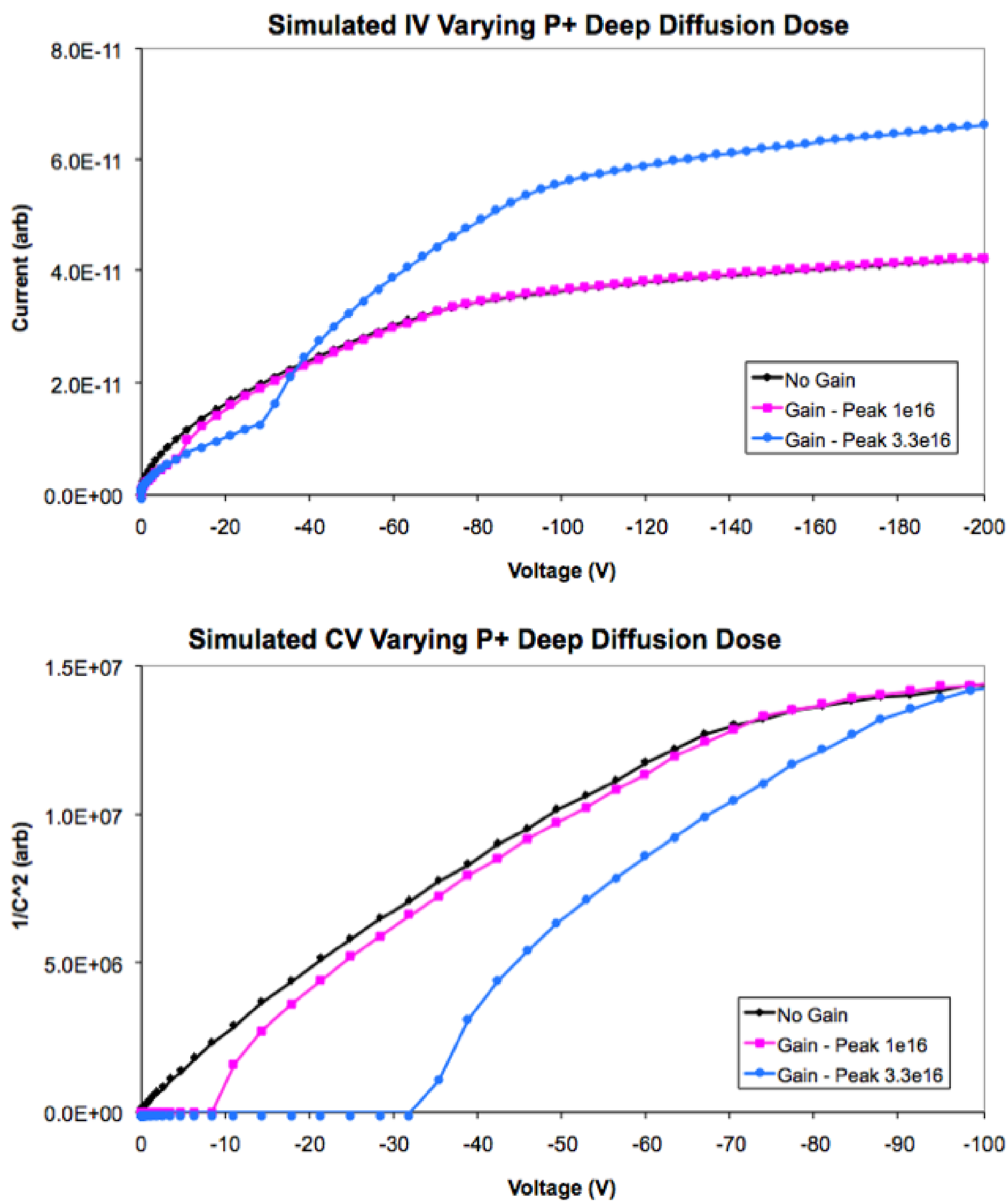

Figure 5.18: When the doping density of the p+ deep diffusion is varied, the kinks in the curves move accordingly. When the concentration reaches that of the bulk, kinks disappear as in the standard pad diode without a p+ deep diffusion.

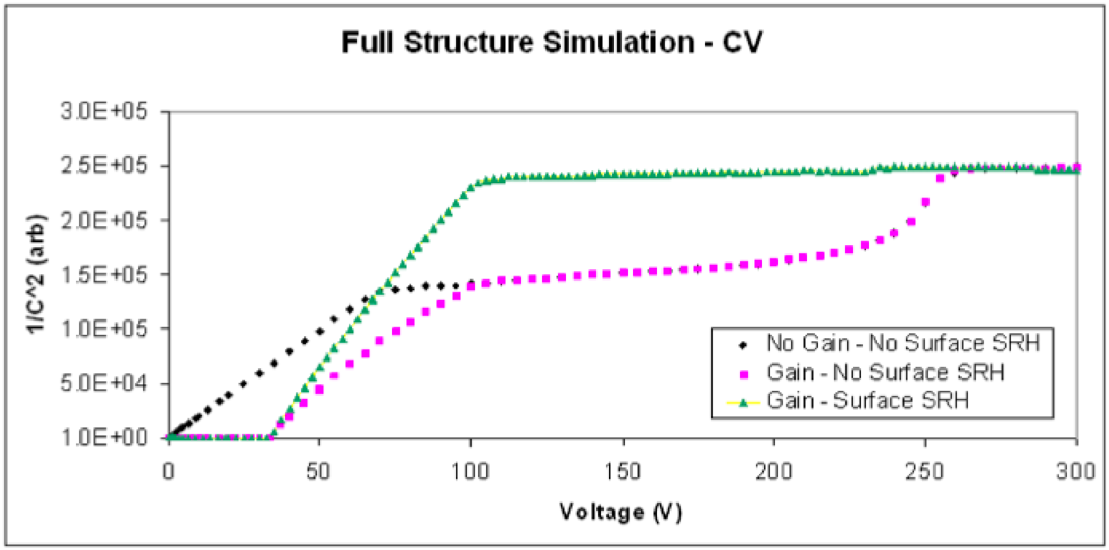

Figure 5.19: This simulation shows two important features. First, the foot in the $1/C^2$ curve in the gain models is caused by depletion of the p+ deep diffusion, which delays depletion of the bulk. Notice the CV curve from the no gain model does not show a foot. Second, the surface recombination shows a significant effect on the capacitance.

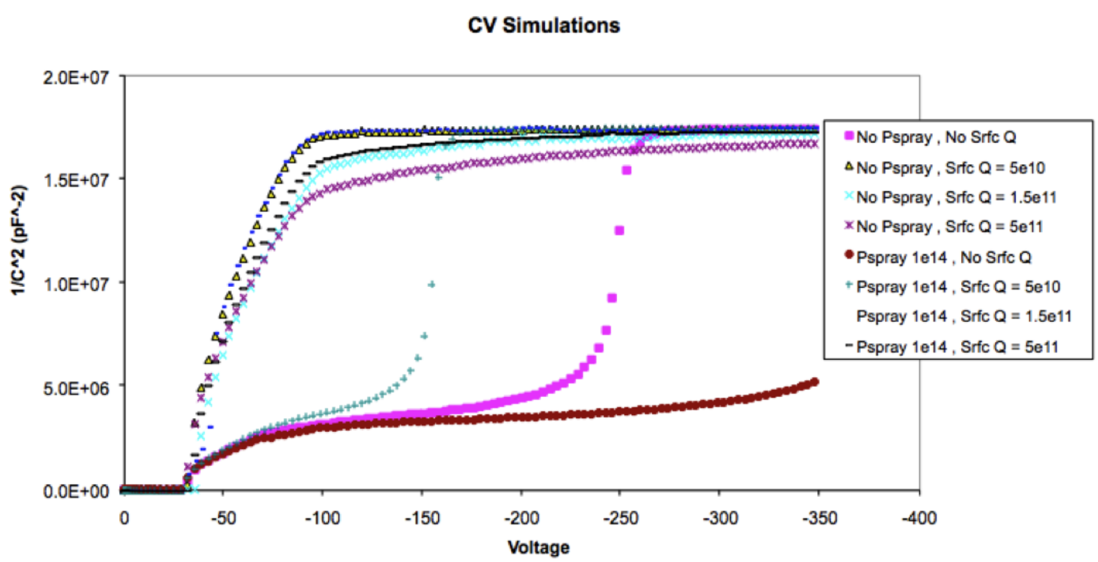

Figure 5.20: This plot shows the effect of charges at the Si02-Si interface on the capacitance. Each curve seems to settle at one of two plateaus, with some exhibiting a transition between the two.

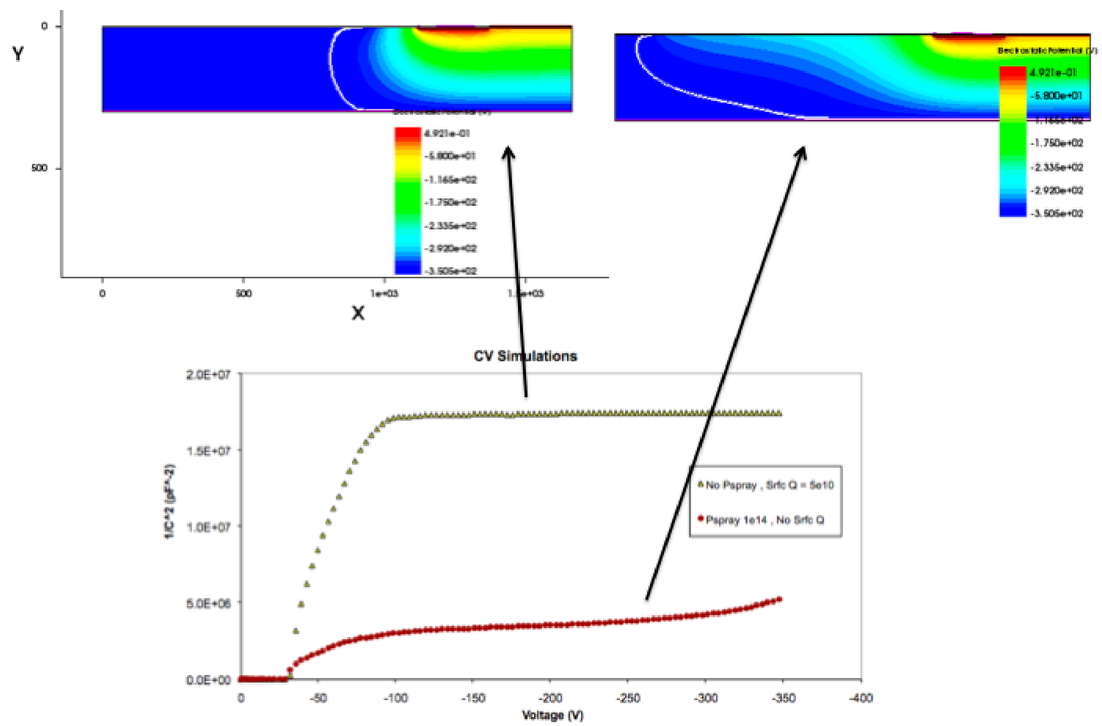

Figure 5.21: A heat map of the equipotential lines in the vicinity of the channel. The transition between capacitance plateaus is due to the charge at the surface interface affecting the depletion region (white outline) presence in the channel.

capacitance cases. The color contours indicate electrostatic equipotential lines in the device. It appears the depletion region in the vicinity of the channel reveals some insight. Shown in Fig. 5.21, one case shows little channel depletion, corresponding to the high plateau on the $1/C^2$ curve, while the opposite case shows significant channel depletion, which corresponds to the opposite case. The reason for the difference, in the simulation at least, is due to the contribution of the surface charges to the electrostatic force in the steady state.

In reality, the CV data do not show such a black and white transition between two capacitance plateaus. However, the variations suggest channel depletion could be an important factor. This would depend on interface quality between silicon and oxide, as well as the presence of P-spray. This is an important factor when considering sensors in operation because a particle passing through a non-depleted region will not ionize charge for collection. However, for the

LGAD structure it will not matter because even when the structure is depleted, charges ionized in the channel will be collected but not pass through the multiplication region.

Even with the aid of simulation software the issue of large differences in leakage current is left unanswered. It could be that the p+ diffusion profile shape plays an important role, in addition to the total effective space charge. In any case, future TCT measurements for the high current sensors should reveal if there is significant change in the multiplication factor.

Field Profiles

Next we observe how the p+ deep diffusion affects the field profiles inside the device. For different bias voltages, the electric field's magnitude is plotted vs. depth in the central gain region orthogonal to the collection electrodes. An identical plot for the same structure without p+ diffusion is shown for comparison. This plot in Fig. 5.22 shows not only that there is a large peak just before the junction, but also that, for high enough bias voltages, the field throughout the remaining bulk is large enough that carriers should be in the regime of saturated velocity. Here, the hypothesis is that when comparing a diode without gain to one with gain, charges should move uniformly from the back to the multiplication region due to the saturated velocity. The only difference should be that the diode with gain exhibits charge multiplication while the one without gain does not. Note that field values in the deeper bulk of the sensors are similar between cases. This is further examined in the transient signal current plots, discussed in the next section.

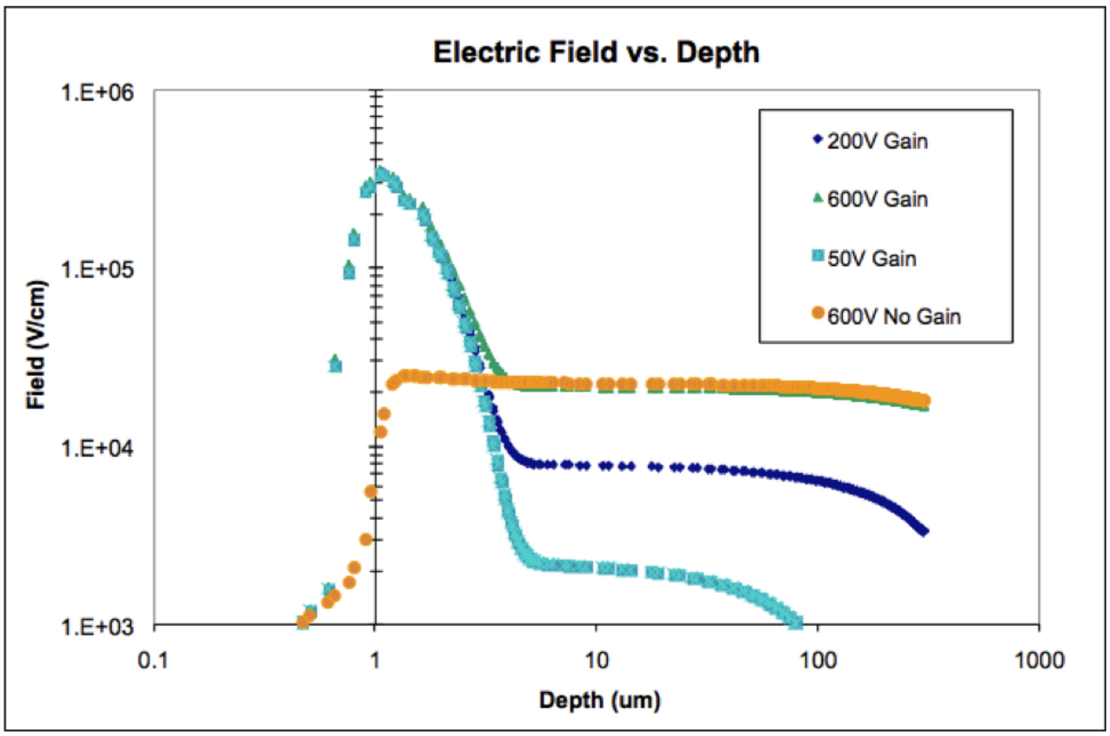

Figure 5.22: The electric field vs. depth under the gain region in the simulated LGAD model. Note the large peak just under the junction stays relatively constant as the field in the bulk increases with bias voltage.

5.2.3 TCT Data

As mentioned previously, only devices from the first CNM shipment were tested with the transient current technique. One of the sensors demonstrated early breakdown, leaving one sensor with gain structures and one without. This proved to be enough for the preliminary results, explored in this section.

When illuminated from the back with alpha particles, the resultant pulse shapes reveal much about the carrier drift dynamics. In accordance with our hypothesis from the section above, the comparison of pulses from the gain and no gain diodes show similar initial behavior, but the distinction between diodes is clearly apparent. The gain pulse is dissected in Fig. 5.23. The shape's implication is that initial electrons take a few nanoseconds to drift the $300\,\mu$m to the multiplication region, appearing much like the case of signal from the diode with no gain. Then a large slew upwards demonstrates the multiplied electrons drifting quickly to their collection point only a few microns away. Liberated holes then oppositely traverse nearly the whole sensor thickness in a few nanoseconds to the opposite collection electrode at the back.

Illumination from the front with alpha particles yields more inconclusive results than illumination from the back. The reason is that the small penetration depth of alphas in silicon prevents many charges from accelerating to ionization energies before collection. Since the large electric field peak extends several microns into the silicon bulk, only a fraction of the initial electrons will traverse its entire length and experience the whole multiplication region. For this reason we primarily consider data from alpha particles incident from the back of the sensor, as each ionized electron should traverse the entire gain region.

To examine the relative gain, the current pulses from the diodes with and without gain are compared as in Fig. 5.24, and the multiplication factor is best extracted in the following way. Assume the time duration of the current pulse from the initial carriers in the gain case is the same as the total duration of the pulse from the no gain case. This assumption should be valid as long as the field strengths in the bulk of each sensor are comparable. In this way we can extract the total charge seen by the readout amplifier from the integral of the current.

Contrarily, the amplitude from each pulse should be considered individually for several reasons. The first is the issue of triggering issue with the oscilloscope, wherein the small pulses from the no gain diode are biased toward the higher energy end of the alpha spectrum. Since these pulses peak at just above the noise baseline, we must trigger relatively much higher with respect to pulse amplitude than for the large gain pulses that don't suffer from such a detrimental signal to noise ratio. Secondly, the gain and no gain samples are mounted on separate housing, which may not be identical. Since alpha particles are very sensitive to energy loss over short distances, the energy spectrum may be shifted. For these two reasons no amount of trigger level adjustment could yield identical pulse amplitudes (alpha particle energy spectra) for the same bias voltage settings. Since the backs of both sensors where the alpha particle enters should be identical, we are forced to conclude there is an offset in the calibration between gain and no gain diodes, and calculation of the gain from comparison of the two will be subject to some systematic error. We can estimate this error from the ratio of the areas of the initial current pulse from the diode with gain and the total current pulse from the diode without gain, though this is also subject to error as the duration of the initial current pulse from the gain diode is also uncertain. Worst case calculations in which the duration of both pulses are the same give figures of systematic errors of up to 35%. It is expected the result of this error would be an increase in the relative gain factor, because the initial current pulse is smaller than the one from the no gain diode, and should be shifted up for proper calibration.

Nevertheless, the initial charge is summed and the current from the new ionized carriers is integrated to yield the multiplied charge. The gain factor is then the ratio of total collected charge from the diode with and without gain, shown in equation (5.2) below, though it is subject to the errors discussed above.

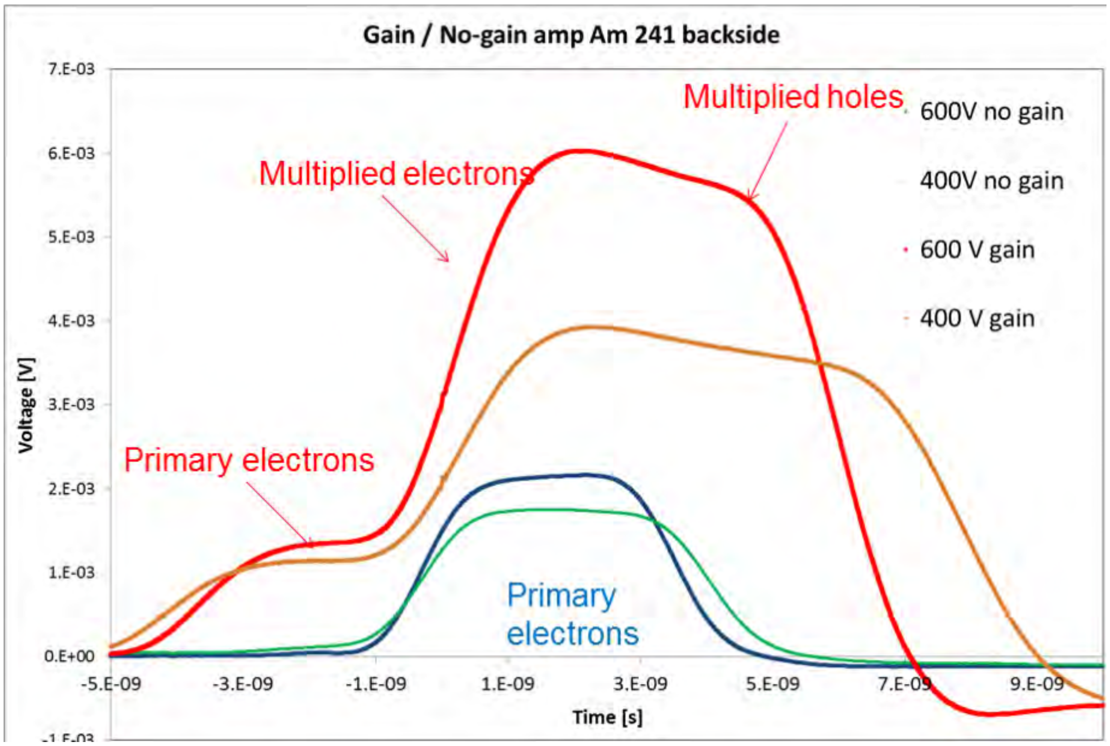

Figure 5.23: A sample averaged waveform for alpha illumination of the gain vs. no gain models. The pulse from the gain model is dissected into regions for the different carrier dynamics.

$$G = \frac{I_M(\alpha)}{I(\alpha)} \times \frac{\Delta T_M}{\Delta T} \tag{5.2}$$

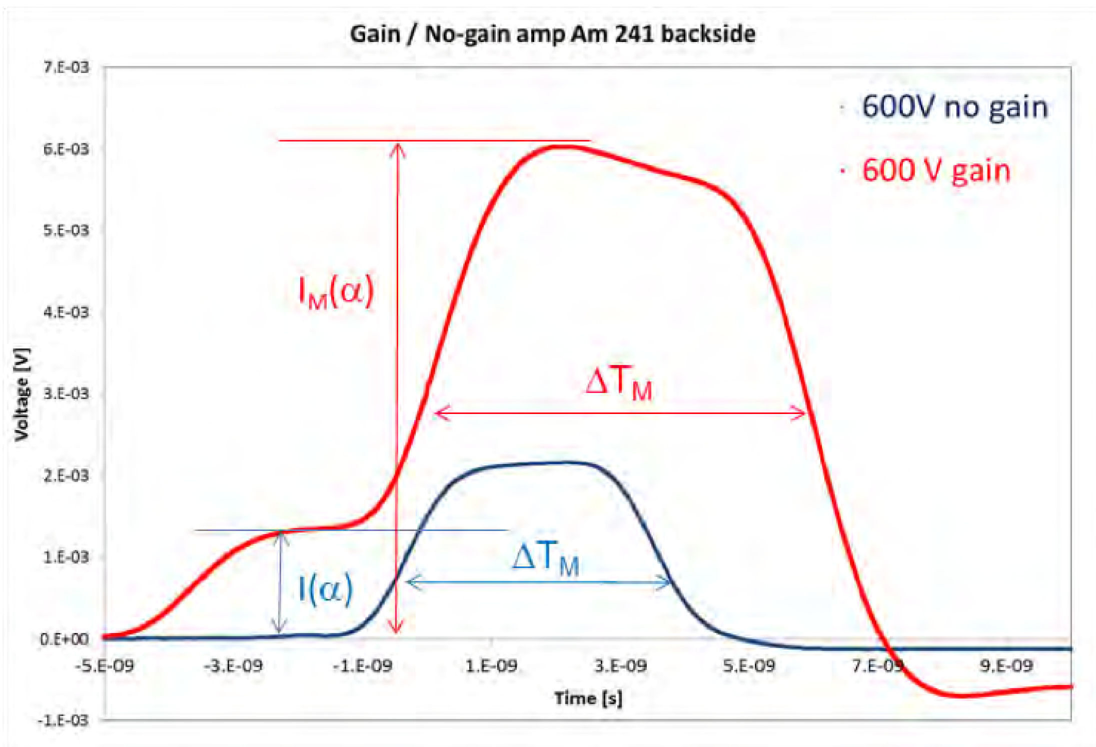

Figure 5.24: A diagram depicting the different quantities used to compute the gain factors. Pulses are from an averaged waveform from alphas incident on the backside of both gain and no gain diodes biased to 600V.

Figure 5.23 shows that the pulses become sharper and narrower for increased bias voltage. This is to be expected, as the larger field should sweep charges away more quickly. However, as discussed above, the multiplication factor should increase with a stronger field as well. Calculation of the total charge as discussed above can easily be converted to effective energy that the alpha particle deposits in the active area assuming average ionization energy is 3.6 eV. For example, if the transient current signal was integrated in time to 1.3 fC, the energy would be calculated as $1.3\,\text{fC}/1.6\,/10^{-19}\,\text{C} \times 3.6\,\text{eV}$ Plots of effective alpha energy and relative gain factors are shown in Fig. 5.25 and Fig. 5.26.

Finally, it should be noted that CERN RD50 collaboration groups have also confirmed observation of charge multiplication in LGAD devices. The team led by G. Kramberger at Jozef Stefan Institute in Slovenia has observed gain factors of up to 10 from β particles from a Strontium-90 source [37]. In addition, the CNM Barcelona group who manufactured the devices have observed gain factors up to 12 from alpha particles [26]. Results are shown in Fig. 5.27. Differences between measurements done by these groups and SCIPP are most likely due to variation in sample quality and electronics in the readout chain contributing to the systematic errors discussed in this section.

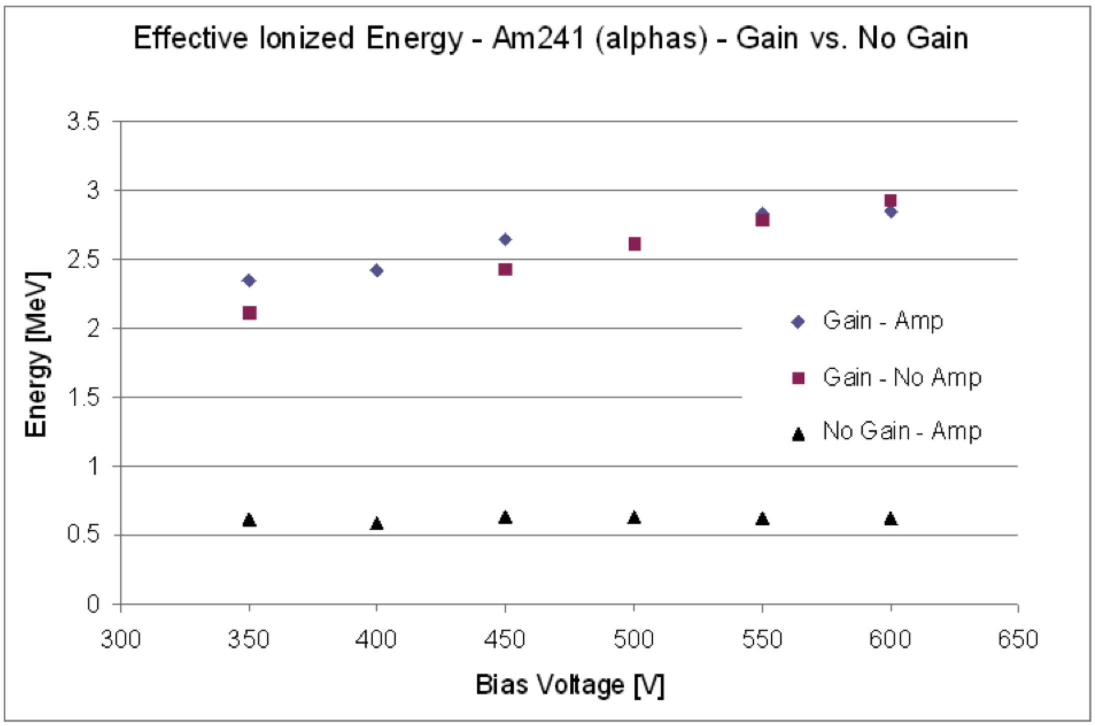

Figure 5.25: A plot of the total energy imparted to carrier ionization from the alpha particles. Note the trend is increasing for diodes with gain and constant for the diode without, affirming the hypothesis that multiplication should scale with bias voltage. Not shown, the statistical error is estimated to be 10%. Systematic uncertainties could contribute significantly more than the statistics but each data point would shift by an amount proportional to the error, leaving the trend intact.

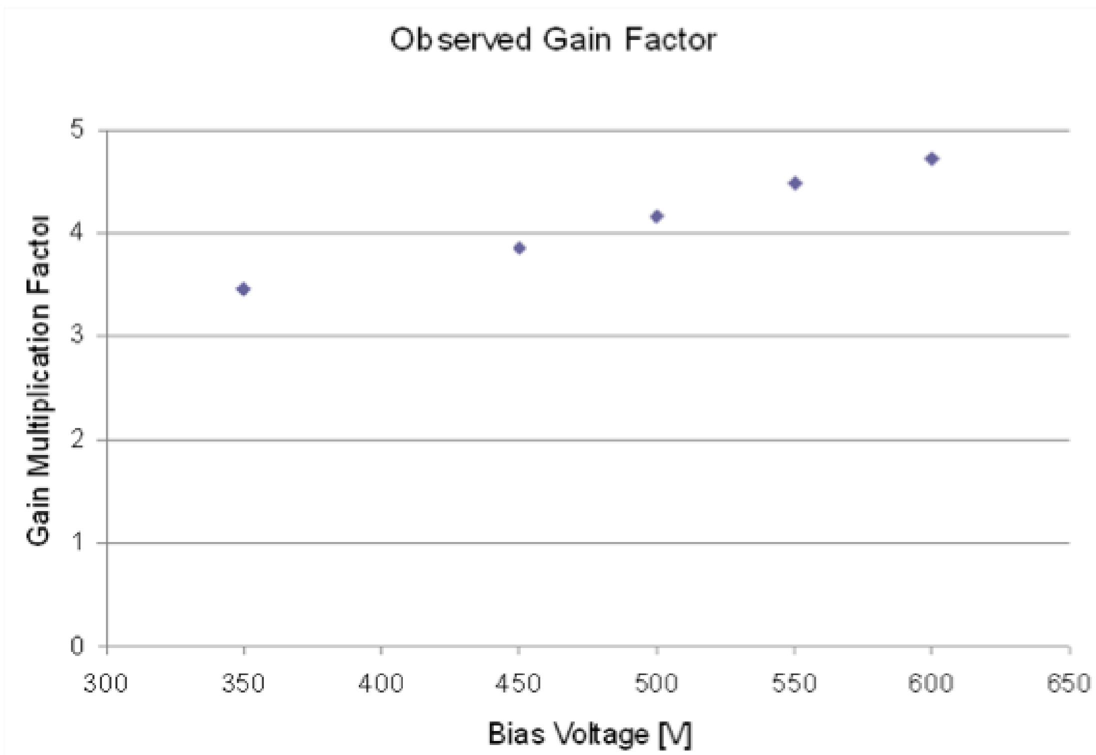

Figure 5.26: The gain factors plotted vs. bias voltage for the diodes with gain. The error on these data are dominated by the systematic uncertainty on the gain vs. no-gain calibration, and are estimated to be up to 35%.

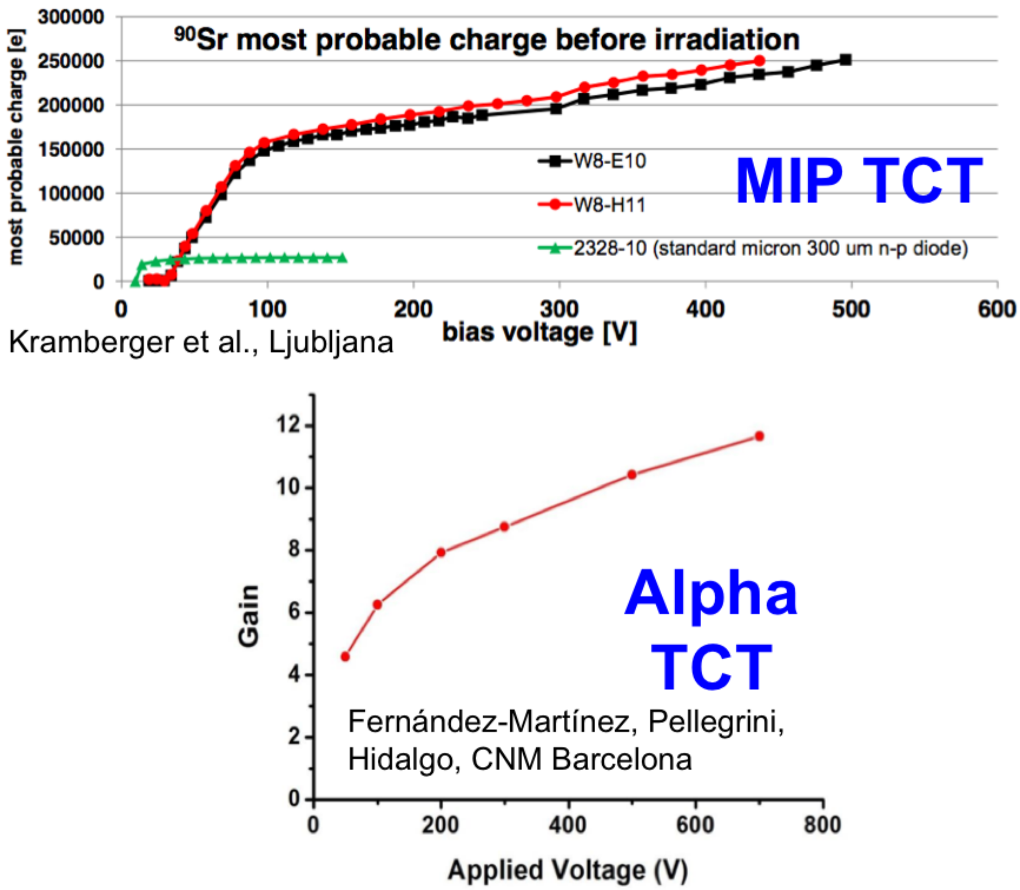

Figure 5.27: Data from RD50 collaborators showing charge multiplication in LGAD devices as well. Data are presented in [37] (top) and [26] (bottom).

5.2.4 TCT Simulations

Due to computational restrictions, transient current pulses will be simulated in the simple diode structure mentioned in the beginning of this chapter but with doping concentrations matching those specified for the LGAD multiplication region. This simplifies the finite element analysis by cutting out the large inactive channel region but still captures the essential physics of the impact ionization. Of course, the carrier avalanche models are implemented in the physics section of the command file.

First we compare signals from traversing MIPs from models with and without gain. The current pulses are plotted in Fig. 5.28. Though there is no current spike as in the alpha TCT data, we can clearly observe the signal for the model with gain is lengthened and thus the total charge collected is significantly higher. When integrated, the observed gain factors shown in Fig. 5.29 are between 1.5 and 3, increasing with bias voltage as expected. The gain factors are not as high as those observed in the data, suggesting that some parameter needs tuning. Note also the 200V current transient suffers from virtual ballistic deficit, as the signal has not returned to the baseline when the simulation ends. If the run had lasted long enough for complete collection, the integrated charge and gain factor would be augmented.

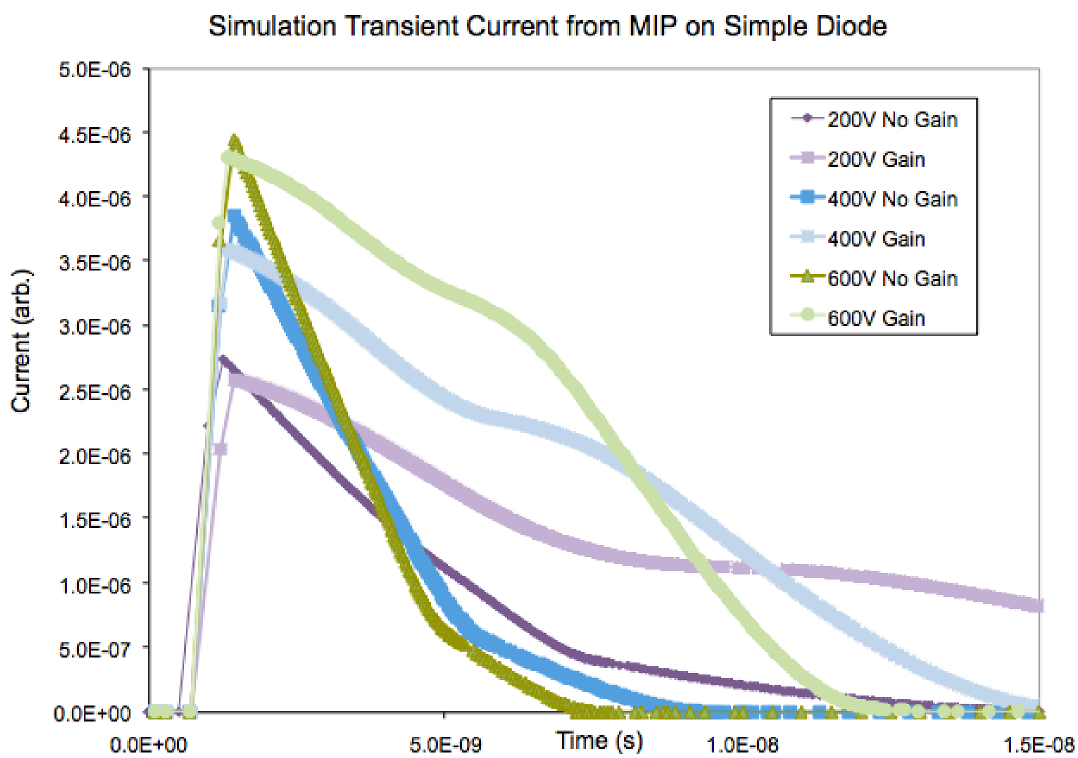

Figure 5.28: The current collected on the top implant from a MIP incident on the simple diode structure with and without deep diffusion.

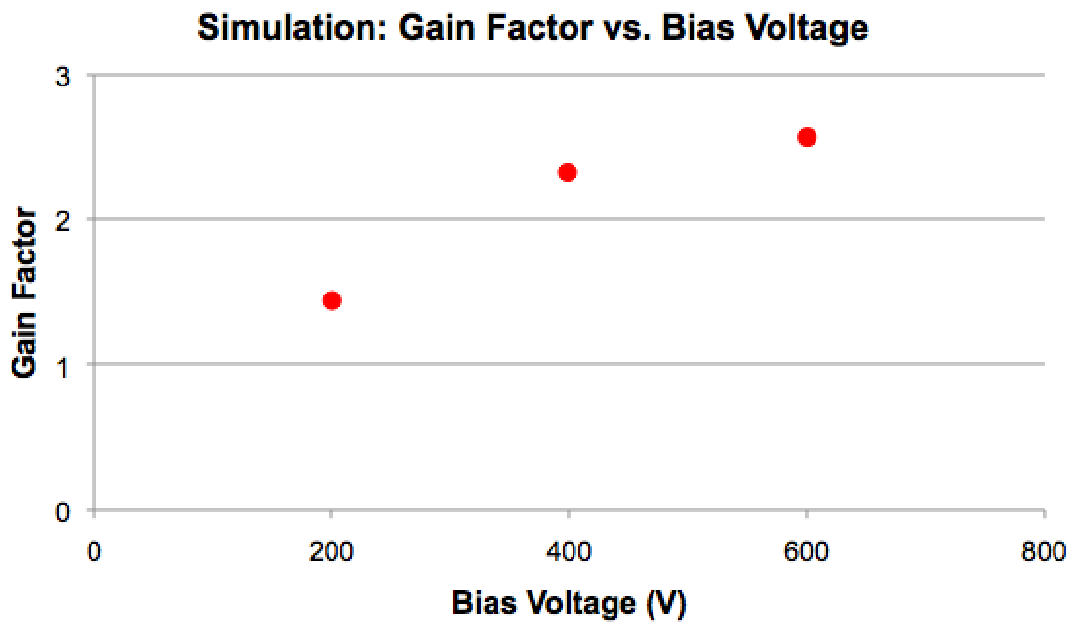

Figure 5.29: The gain factor computed from integrating the currents from the MIP simulations discussed in this section.

5.3 PSPICE Pulse Shape Analysis

With a general idea of how a current pulse from an alpha particle should behave in the LGAD model, we would like to study the effect of the readout electronics on the pulse waveform. No amplifier is added to the chain, but a 3 part current pulse is excited in the circuit. The current has contributions from the initial ionized carriers, the fast multiplied electrons, and the slower multiplied holes and has been normalized to the energy deposited by a 2 MeV alpha particle with a multiplication factor of 4. In contrast to the measured data, the current pulse is constructed with sharp edges to determine the shaping characteristics of the electronics. The circuit and the current pulse are depicted in Figs. 5.30 and 5.31.

The output shape resembles the observed waveform, so we can conclude the electronics contribute to pulse shaping. This is important and should be optimized when considering future setups for TCT measurements. The voltage output is shown in Fig. 5.32

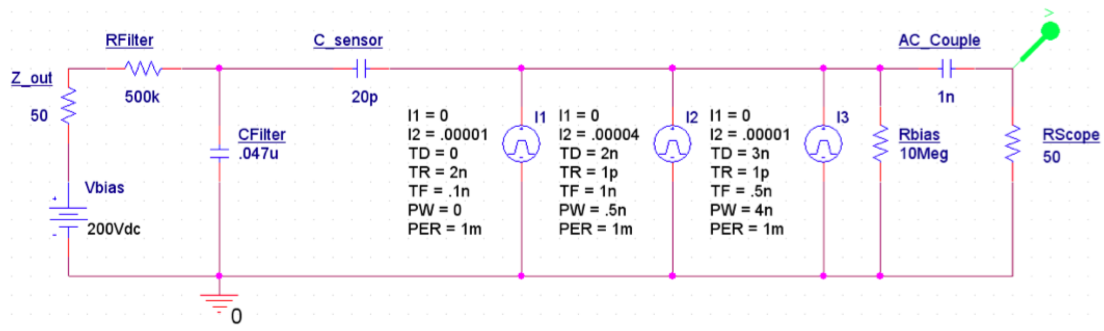

Figure 5.30: The PSPICE circuit diagram modeling the sensor and TCT data acquisition analog readout circuit.

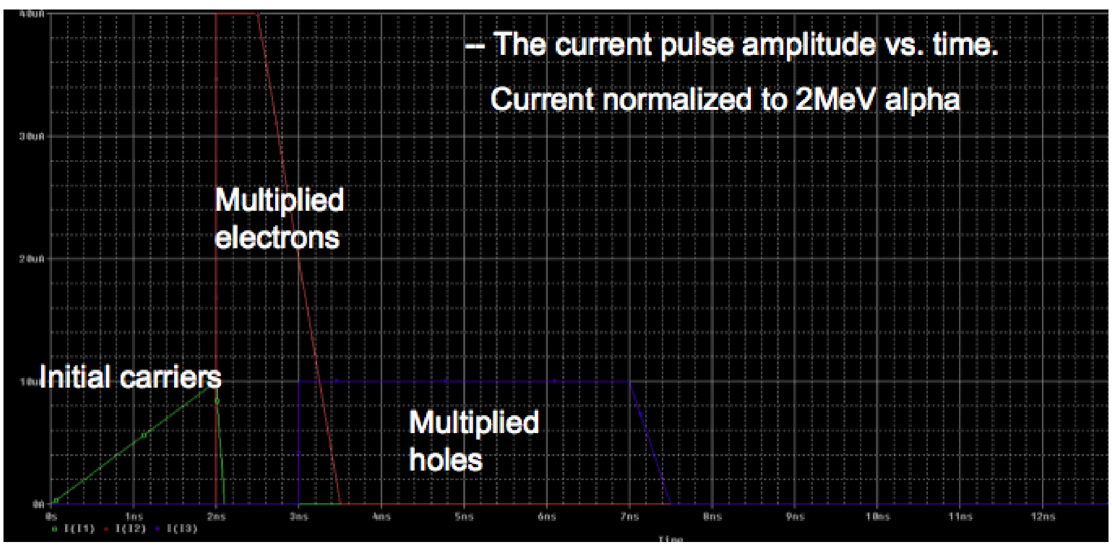

Figure 5.31: The input current pulse modeling the carrier dynamics in the LGAD from a 2 MeV alpha incident from the back. Note the sharp edges on the current pulse.

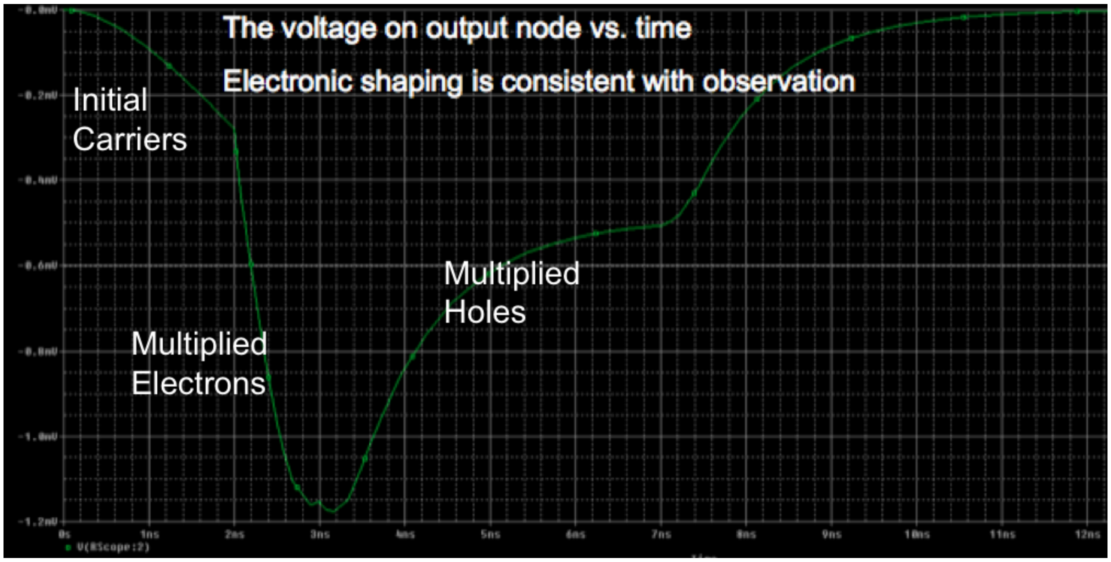

Figure 5.32: The voltage seen at the scope's resistor as computed from PSPICE. Note this output is shaped, confirming the effect of the readout electronics on a current pulse.

5.4 Thinned LGAD Model

5.4.1 DC Simulations

A preliminary investigation of the LGAD layout was simulated in thinner detector models to test the possibility of faster collection. It is expected that a thinner model will sustain higher fields in the bulk for the same bias voltage when compared to a thick sensor. This is because the gradient of the equipotentials is much sharper as the bias voltage is distributed throughout the thinned bulk. However, an important question remains as to how this will affect the gain region field peak near the surface collection electrode. Will this higher field lead to an earlier breakdown in thinner models, and if so how significant is the effect?

First IV test results in Fig. 5.33 show that thinner models do indeed experience an early breakdown, though also generally lower currents. In principle, one could scale the depth of the p+ deep diffusion down with the thickness of the sensor, however this would presumably lead to lower gains as multiplication is dependent on the distance the electron travels before ionizing another carrier pair. For this reason, this feature scaling was not investigated.

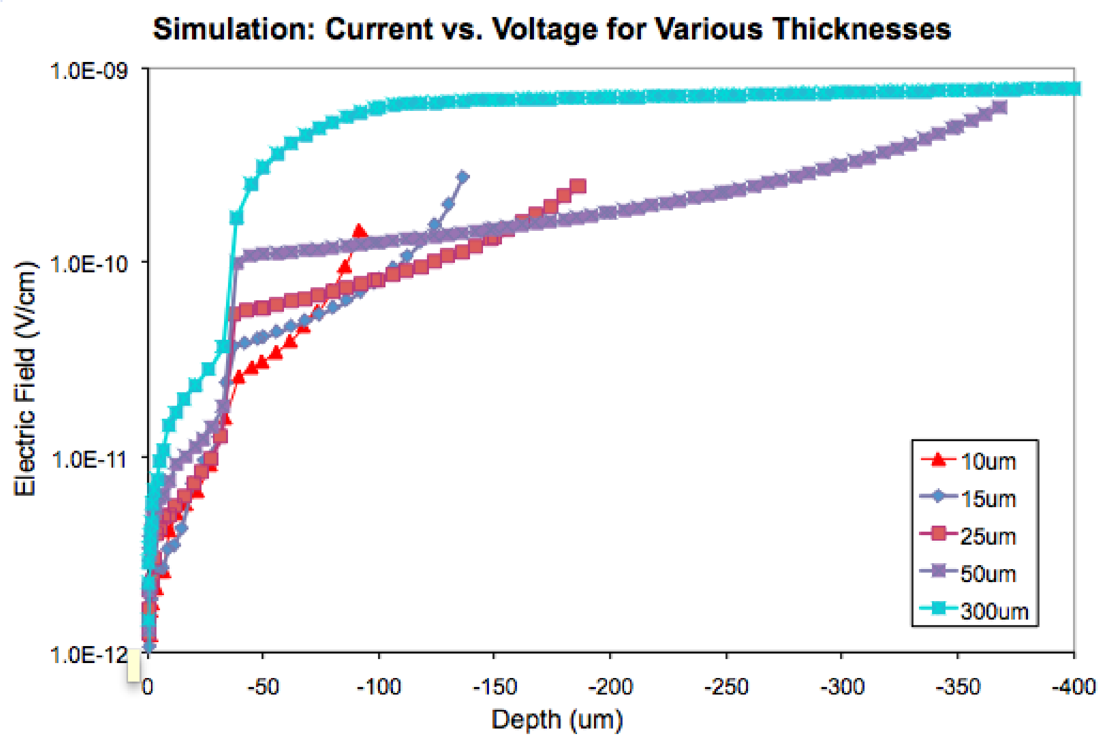

Figure 5.33: The IV curves for sensors following the LGAD layout but of various thicknesses. The curves end when the field exceeds 4×10^5 V/cm in the silicon, which is imposed as the breakdown condition. Note the kink is still present in some degree for all models.

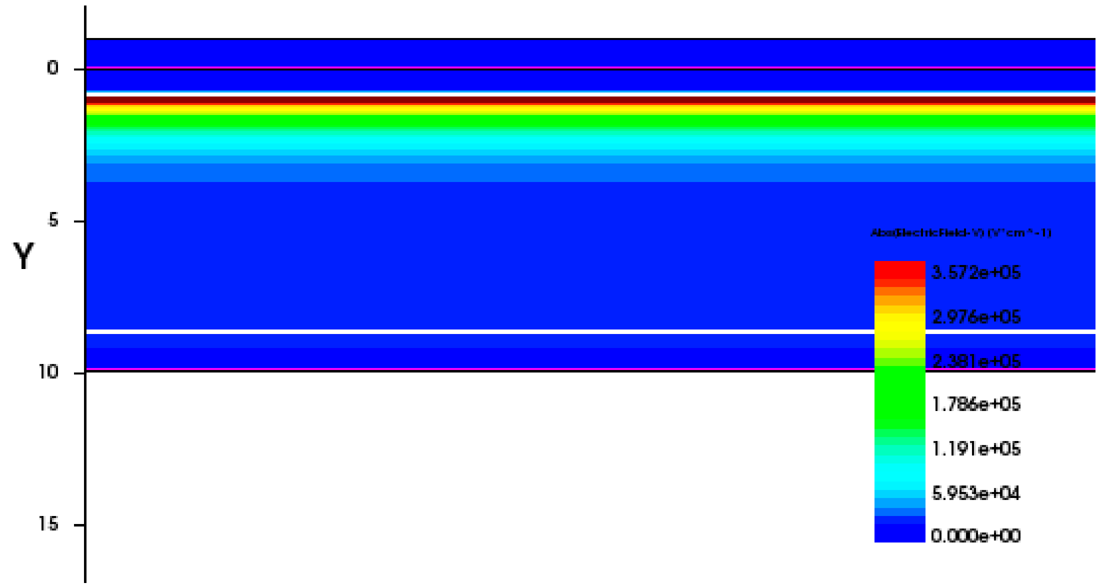

Figure 5.34: A 10 μm thinned LGAD model still supports a field peak below the collection electrode at 50 Vbias.

5.4.2 Simulated Field Profiles

Examination of an orthogonal slice of the field profile in the gain region yields an encouraging conclusion. Even at 10 μMeV thickness, the electric field contour plot of Fig. 5.34 shows a field peak under the collection electrode similar to the thicker LGAD model. This suggests that charge multiplication should be possible even in this thin structure. For 50V bias, sensors of all thicknesses seem to demonstrate a field peak of similar magnitude, shown in Fig. 5.35. This means that thin sensors could be operated at lower bias voltages than thicker counterparts because full bulk depletion occurs much earlier. In addition, bulk drift fields are stronger in thinner sensors, leading to even faster carrier collection. However, the distinction between linear gain and breakdown becomes even finer than in thick sensors; thus fabrication must be ultra-precise. Still, the results are promising and should be considered in the next iteration of sensor design.

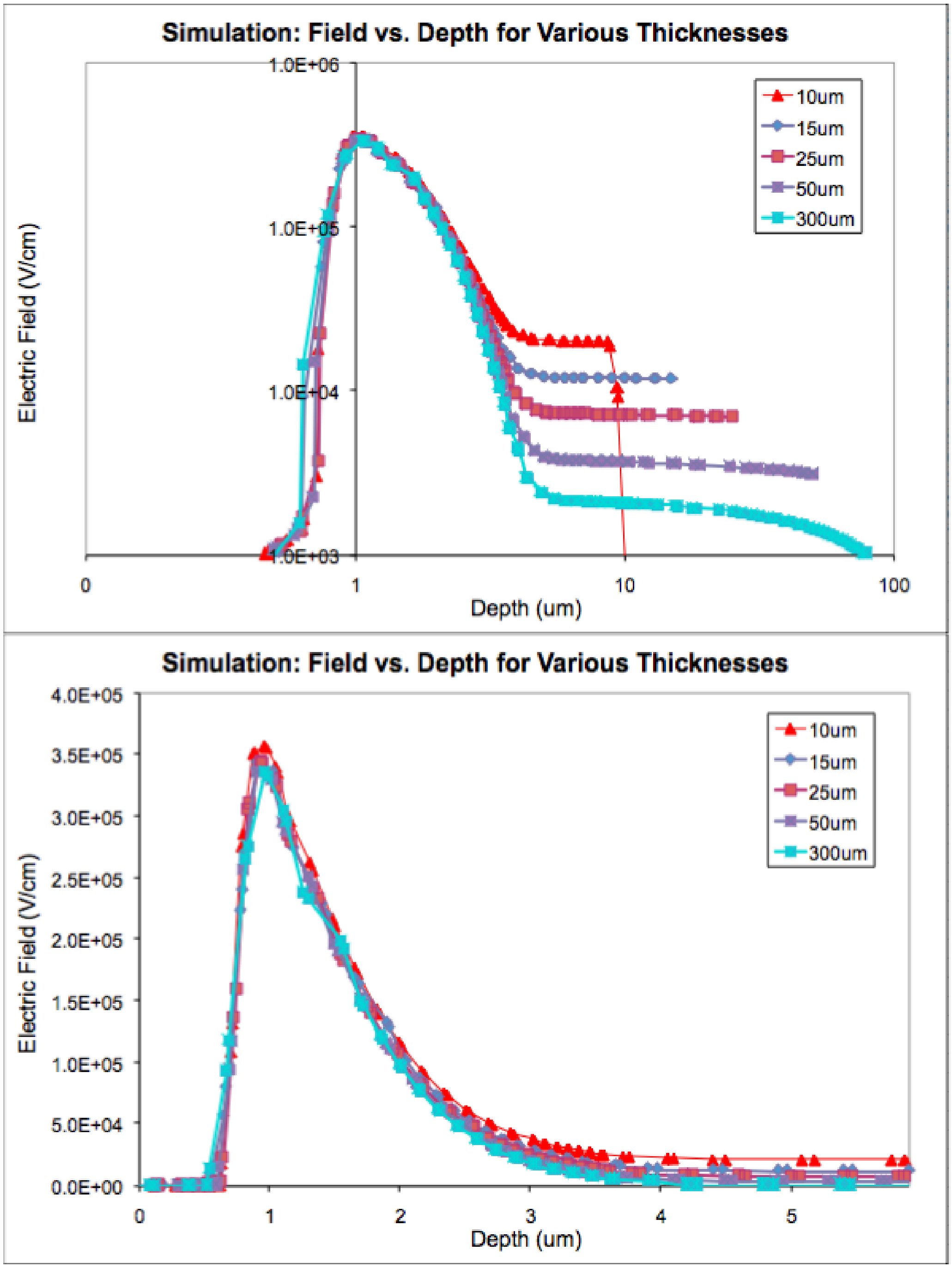

Figure 5.35: Detail of the electric field vs. depth under the gain region in the thinned LGAD model. Profiles are taken at a bias voltage of 50V. Note the thinner models have a higher bulk field as expected, and the thickness does not affect the height of the field peak.

6 Conclusions

A systematic study of charge multiplication using an APD deep diffusion doping scheme in a P type diode device has been conducted. It is found that this controlled doping scheme can produce uniform electric fields near the collection electrode large enough to stimulate the onset impact ionization. Samples produced at CNM Barcelona have been electrically characterized and measured at SCIPP. DC tests yield unusual kinks in the IV and CV curves due to the APD reach through doping. CV curves are additionally affected by charges at the Si02-Si interface. Plots of the electric field show a large peak extending several microns into the bulk, which is ideal for charge multiplication. TCT analyses show charge multiplication can augment the collected charge by up to factors of 5. This can be useful in designing a detector for fast timing applications, which are necessarily thin. Simulations of similar APD models with thinned sensor bulk suggest charge multiplication is also feasible in thin sensors.

Appendix A TCAD Operational Principles

This is a brief overview of how to make models and run simulations using Sentaurus TCAD tools. A picture of the data flow is shown below, and each section is described. For more information consult the manual [29].

A.1 Structure Definition

Sentaurus offers graphical user interface software, shown in Fig. A.1, to aid in the definitions of a structure. As it turns out, this is just to create the text of an input script for the structure editor that contains the dimensions of the model, as well as material placements, doping definitions, electrical contacts, and meshing references. Careful attention is required when meshing, especially a 3D structure, as the most efficient simulations optimize the number and placement of nodes. Simulation time increases like a power law with node number, but cell size should be small enough that quantities of interest should can be approximated as constant over the dimensions. This usually entails refining meshes in areas of high current densities and field or doping gradients. Luckily, Sentaurus has built in an adaptive meshing algorithm with a few user tunable parameters for meshing simply. A screenshot depicting a 3D meshing example is shown in Fig. A.2. Still, the user may find this part of the simulation process as the most tedious, and in general it is safer to err on the side of too many nodes, resulting in increased simulation time but less chance of approximation or convergence errors.

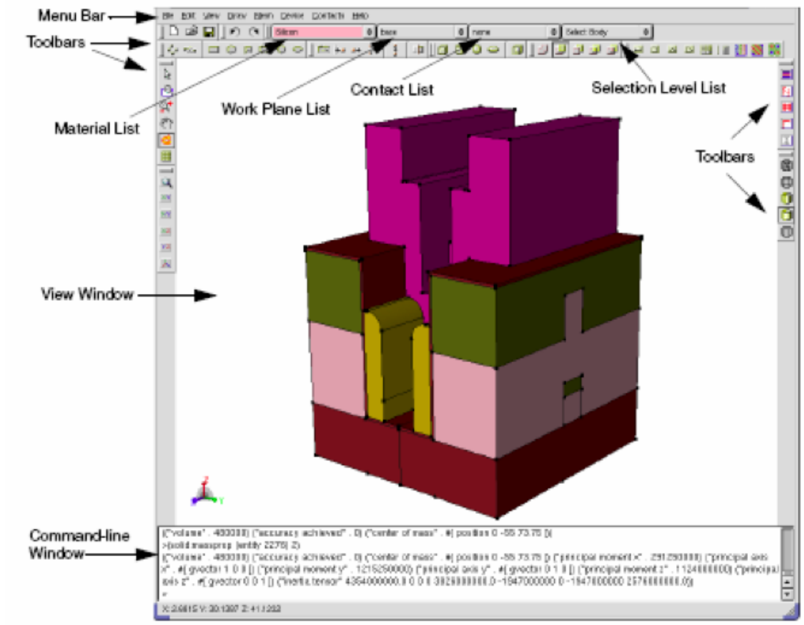

Figure A.1: The graphical user interface for Sentaurus Structure Editor showing a stock example transistor structure. [29]

A.2 Device Simulation

Once the device is defined, Sentaurus computes the mesh with the parameters defined, and outputs a grid and boundary file. The next step is to specify the commands that will be used in the simulation. The command file has multiple sections, described here.

File

Contains information about what files to reference in the computation and how to label output files. It is important to use the correct file extensions here.

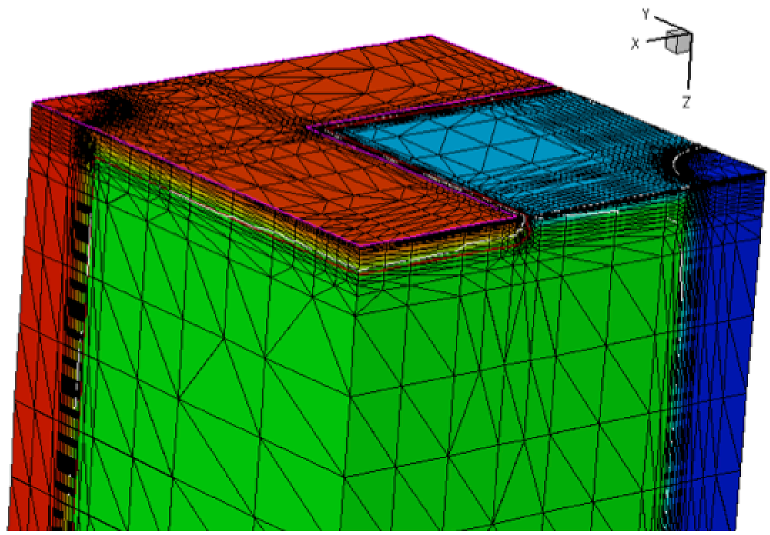

Figure A.2: A screenshot showing the finite element mesh for an example 3D sensor structure. This illustrates the usefulness of the adaptive mesh algorithm, as the mesh is most dense near large doping gradients and less so in bulk silicon.

Electrode / Thermode

In this section the electrical and thermal contacts are specified along with initial conditions for later reference.

Physics

This crucial section contains all the physical models to be implemented in the computation. Models are applied to the device in general but it's also possible to employ models in material or region specific areas for more control over the simulation. There are many models, all with different, tunable parameters. In each simulation it is of utmost importance to use only relevant models. If too many are used, each iteration's computation time can diverge. If too few are used, one is in danger of missing some important physics. From experience and the following sources, the recommended models for a un-irradiated, planar, particle-sensing device are as follows:

- **Mobility -** Doping Dependent, Carrier Carrier Scattering, High Field Saturation, Component of Electric Field Normal to an Interface
- **Generation / Recombination-** Doping Dependent Shockley Read Hall (SRH) Model, Surface SRH (if applicable)
- **Effective Intrinsic Density -** Old Slotboom (For bandgap narrowing in highly doped regions)

If applicable, one may also want to include variable Si / Si02 interface charge to simulate dangling bonds at the surface. Also, any incident radiation by alpha, gamma, or heavy ions is specified here with parameters controlling time of crossing, direction, and energy.

Math

In the math section, the user specifies primarily which solver to use, along with its parameters for error control, number of iterations, etc. Here one can also choose to include a break condition to end the solve loop early. A relevant example would be a cap on the electric field in the silicon to model the onset of breakdown. Finally, parallelization is an option if the number of available licenses allows it.

Solve

The solve section contains an ordered list of the steps to be performed during the simulation. Generally, the first step is to build up an initial solution with the coupled command, which activates a Newtonian root finding algorithm for the set of desired equation-variable pairs, which may include Poisson's equation, and electron and hole continuity equations. Once the initial solution is known, a quasi-stationary command allows ramping of electrode or thermode values. This command takes step size controlling parameters as arguments for greater control of the solver. Any transient current from irradiation requires a transient command, which solves and iterates the coupled equations in a defined time interval.

Plot

Here, the user defines which quantities to write to the plot file for later analysis.

A.3 Workbench

With the device and command files in place, the simulator is ready to compute. As mentioned earlier, batch processing is made possible by a tool called Workbench. In either file, a parameter's value can be replaced with a variable to be specified in the spreadsheet of experiments. Each time a variable is added to the spreadsheet, a new experiment is created that Workbench will evaluate sequentially. For the user, this eliminates the need to run a single simulation, save the output, change a value in the script, and rerun over and over. The layout is shown in Fig. A.3.

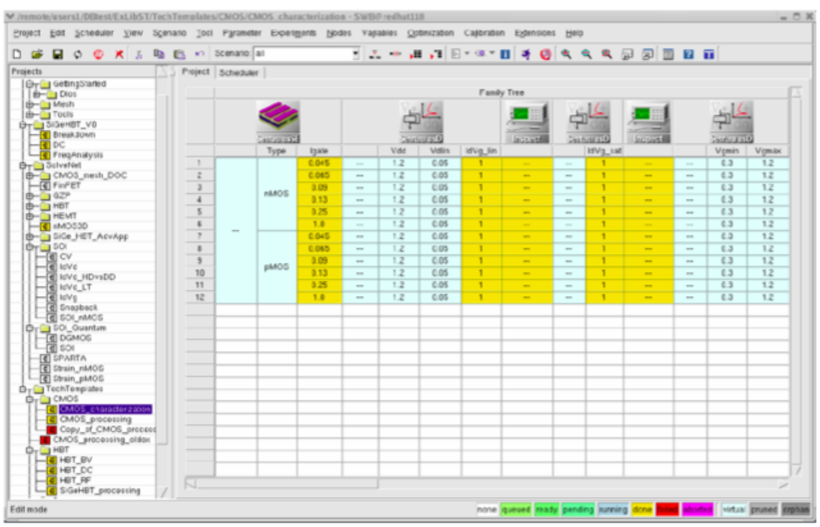

Figure A.3: Screenshot of the interface for Sentaurus Workbench, showing batch processing and simulation flow. Each row contains a different set of parameters that the simulator will execute in left to right sequential order for the processes shown above the columns.

A.4 Output Analysis

Analysis of output files is made possible by tools called **Inspect** and **svisual**. Inspect allows quick visualization of x-y plots, the most common of which is current vs. voltage. The data can be extracted to several file formats from here. Svisual shows the device structure in detail with values of variables as multiple dimensional contours. The user can zoom in on areas of interest, inspect the structure's mesh, extract a lower dimensional slice of the data and write data to files. Screenshots of both inspect and svisual are shown in Fig. A.4.

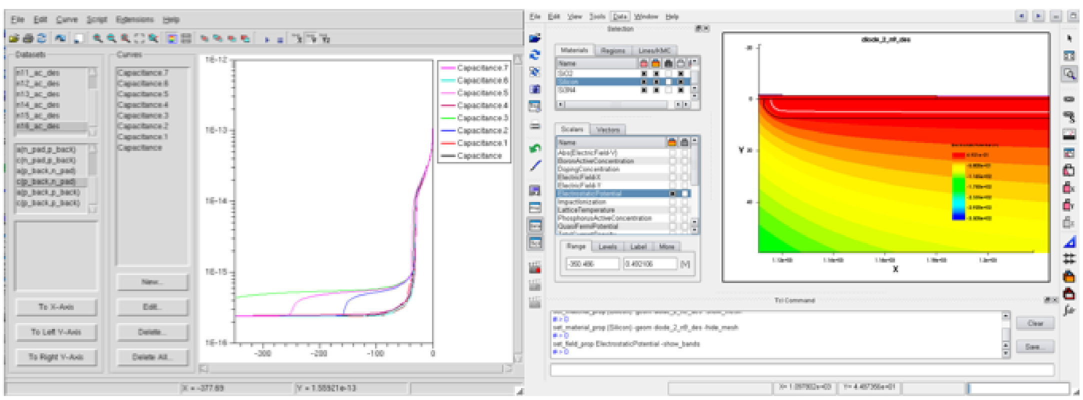

Figure A.4: Screenshot of the interfaces for Inspect and Svisual. Inspect (left) shows a typical set of Capacitance vs. Voltage curves, and Svisual (right) shows equipotential lines near an implant.

Sentaurus makes it possible to couple the device with SPICE netlists for complete circuit simulation. It is necessary to describe the circuit for AC analysis. This requires the use of a network hierarchy in the command file to execute properly; see the manual for further details [29].

Appendix B Time Evolution of Some Quantities

Some more contour plots of relevant quantities after a MIP traverses a simple diode structure. From the plots of electron and hole densities of Fig. B.1 and Fig. B.2, we can see that ionized charge density is significant compared to the space charge background. For this reason the electric field is perturbed by the carriers presence, and may be subject to screening effects. This may be an important factor when considering ultra fast collection time. Figures B.3 and B.4 show current density evolutions in the simple diode for bias voltages of 20V and 2000V respectively. These results show how the strength of the electric field affects the duration of the carriers' presence on

Instructions for how to read the evolution plots are discussed in Section 5.1.2 and the key for each tile's time stamp is shown again in table B.1.

Time (ns)		
0	1	2
3	5	7
9	12	15

Table B.1: This table shows the time of evaluation for each tile in the evolution profiles.

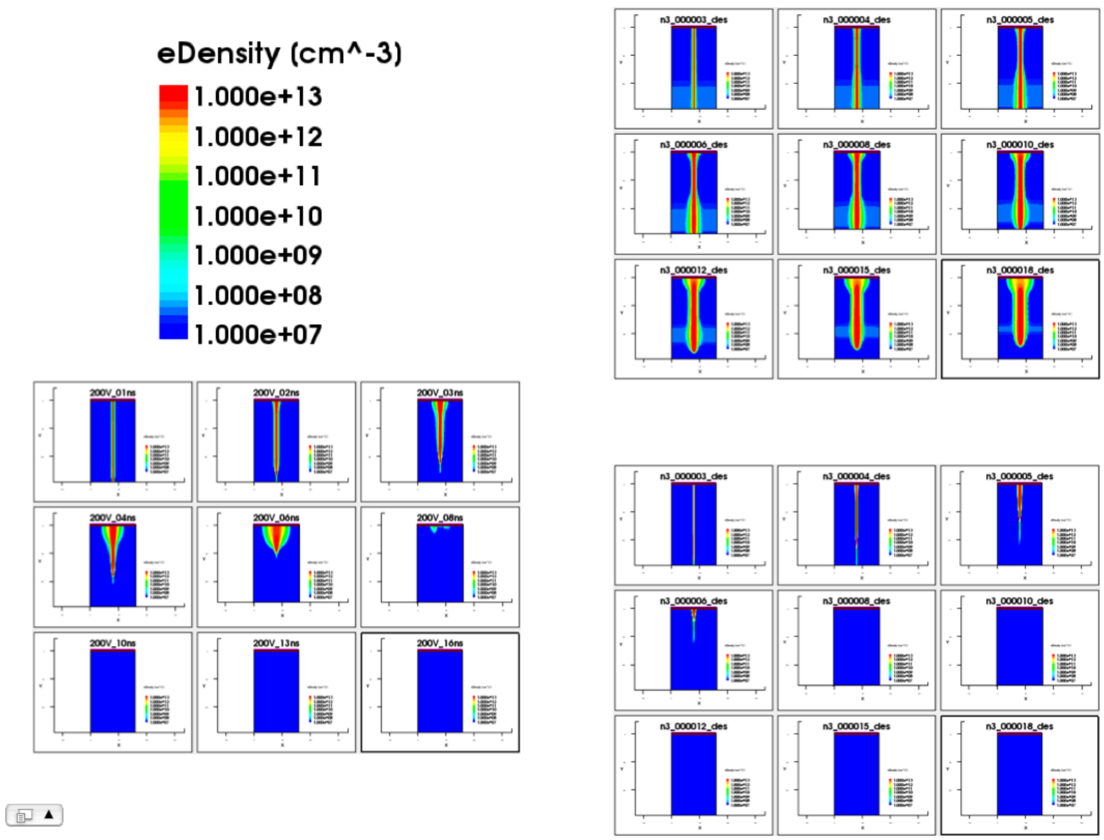

Figure B.1: 2D plot of the electron density vs. time in the simple diode after incident MIP.

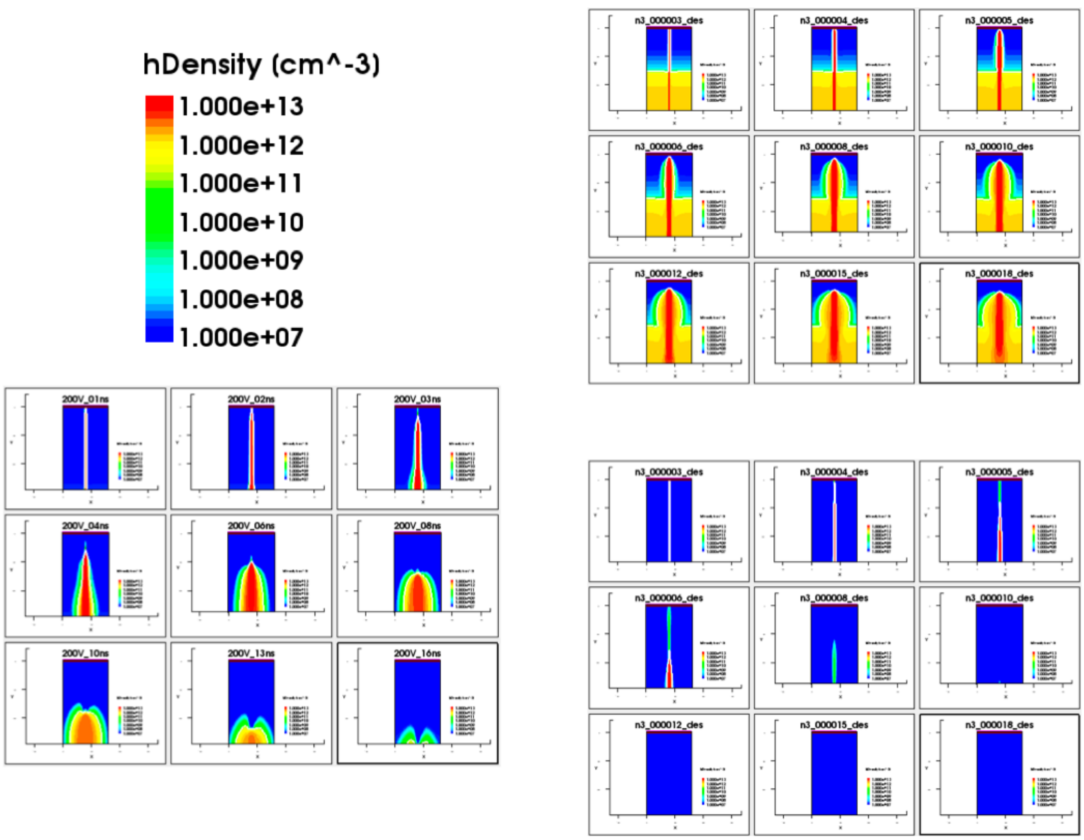

Figure B.2: 2D plot of the hole density vs. time in the simple diode after incident MIP. Note the holes remain active carriers in the bulk even after the electrons are swept away.

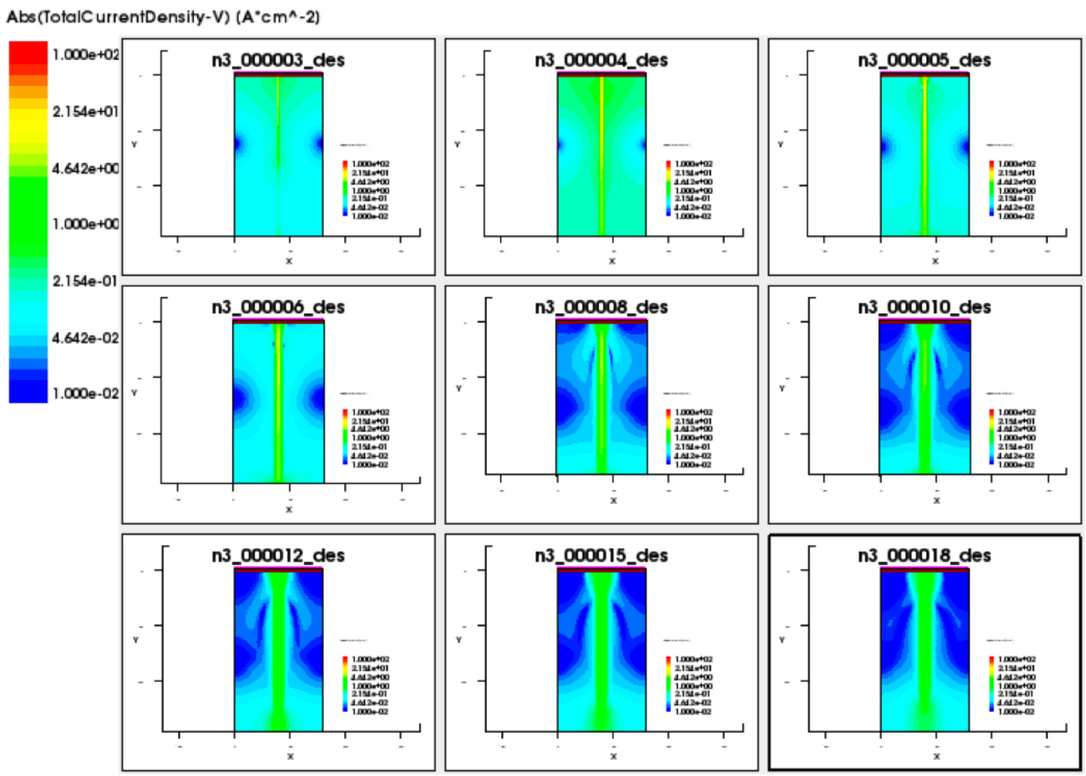

Figure B.3: 2D plot of the total current evolution in the simple diode after incident MIP. Vbias = 20V

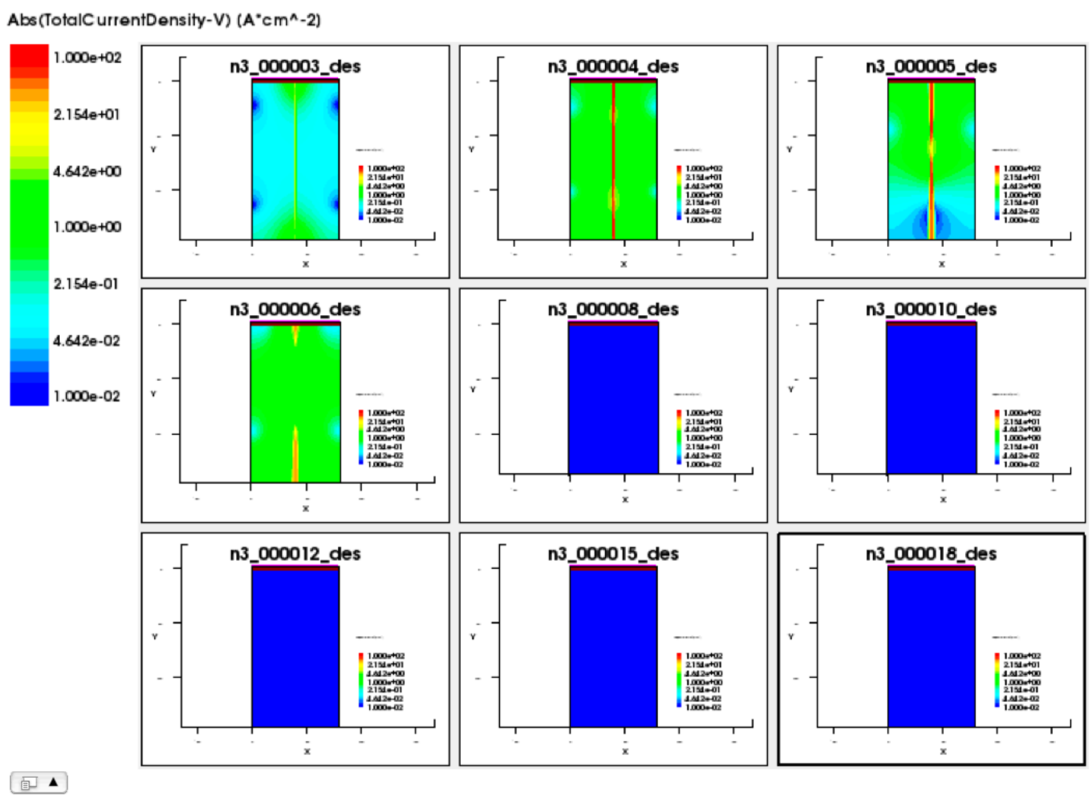

Figure B.4: 2D plot of the total current evolution in the simple diode after incident MIP. Vbias = 2000V

Appendix C LGAD CV comparisons

To understand the variation in CV curves, the traces were color coded according to different parameters to look for trends. Figure C.1 shows an arrangement of the curves based on current levels and Fig. C.2 shows an arrangement based on Geometry of the pad implant. The geometries are labeled in Fig. 3.2. No clear patterns emerged, though there is a slight difference in full depletion capacitance values between structures with a collector ring and those without.

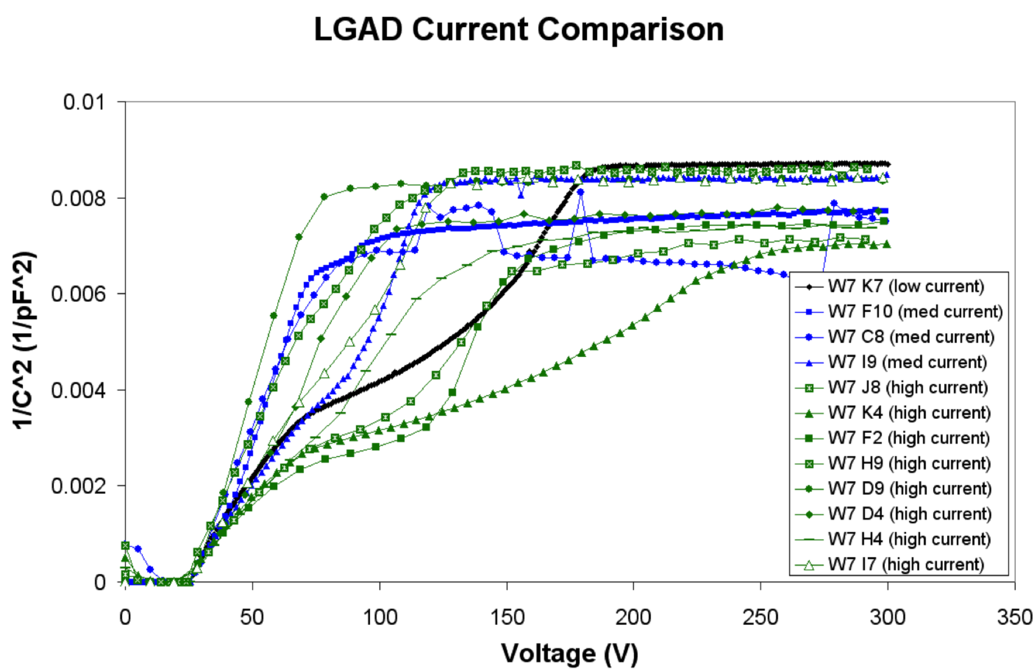

Figure C.1: When CV curves are color coded according to IV current level, no clear trend emerges.

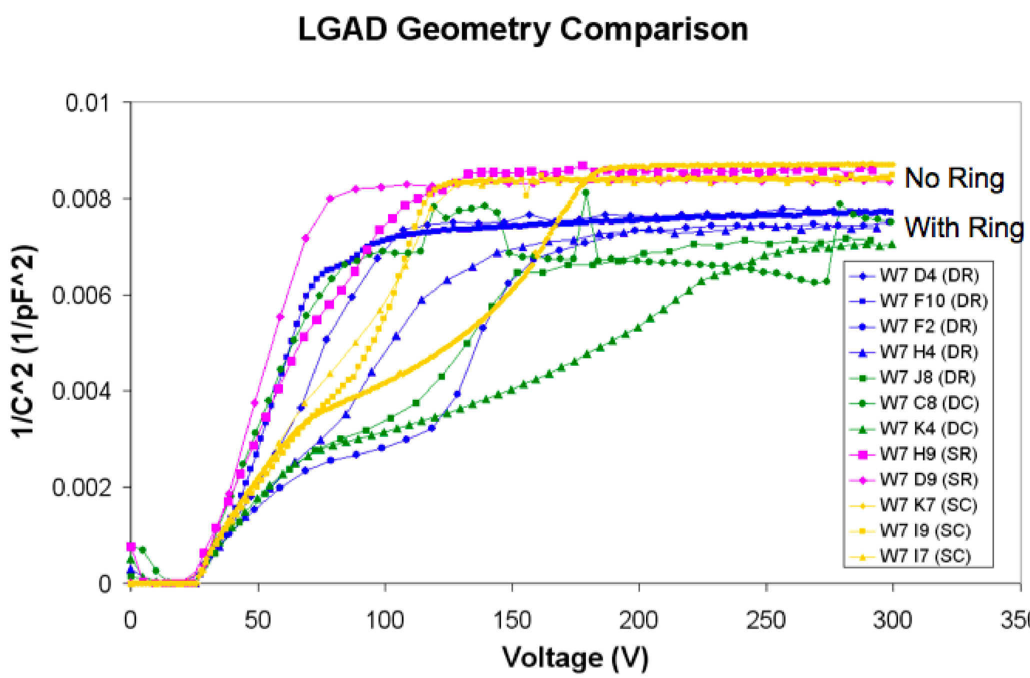

Figure C.2: When CV curves are color coded according to pad geometry, the only noticeable effect comes from the slight difference in final capacitance due to the presence or absence of the collector ring.

Bibliography

[1] ATLAS Collaboration (G. Aad et al.), The ATLAS Experiment at the CERN Large Hadron Collider, JINST 3 (2008) S08003

[2] F. Hartmann, *Evolution of Silicon Sensor Technology in Particle Physics*, Springer-Verlag Berlin Heidelberg 2009

[3] H. Spieler, Lectures on Detector Techniques, `http://www-group.slac.stanford.edu/sluo/lectures/detector_lecture_files/detectorlectures_6.pdf`, SLAC 1998

[4] H. Spieler, *Semiconductor Detector Systems*, Oxford University Press 2005

[5] A. Brandt, C. Royon et al., AFP: A Proposal to Install Proton Detectors at 220m around ATLAS to Complement the ATLAS High Luminosity Physics Program, `http://www-hep.uta.edu/~brandta/ATLAS/AFP/TP-report-May52011.pdf`, 2011

[6] L. Taylor, Silicon Pixels, <CMS.web.cern.ch/news/silicon-pixels>, 2011

[7] H. Wiedemann, *Particle Accelerator Physics*, Springer-Verlag Berlin Heidelberg New York, 1999

[8] M. G. Albrow et al., Quartz Cherenkov Counters for Fast Timing: Quartic, 2012 JINST 7 P10027

[9] E. Martin, G. Aglieri Rinella et al.,, Review of Results for the NA62 Gigatracker Read-Out Prototype, 2012 JINST 7 C03030

[10] V. Bindi et al., The Time of Flight Detector of the AMS-02 Experiment on the International Space Station, Nucl. Instrum. and Methods A716 2012 Pages 478480

[11] The Alpha Magnetic Spetrometer Experiment, The Instrument, `<http://www.ams02.org/what-is-ams/tecnology/>`, 2013

[12] S. Schuon et al., High-Quality Scanning Using Time-of-Flight Depth Superresolution, IEEE Computer Society Conference, `http://www-cs.stanford.edu/people/theobalt/TOF_CV_Superresolution_final.pdf`, Anchorage, Alaska 2008

[13] M. Conti, Focus on Time-of-Flight PET: The Benefits of Improved Time Resolution, Eur J Nucl Med Mol Imaging. 2011 Jun;38(6):1147-57

[14] ToF-PET, Hamamatsu Photonics Corp

[15] S. M. Sze, *Physics of Semiconductor Devices*, John Wiley & Sons, Inc. Hoboken, New Jersey 2007

[16] N. W. Ashcroft, N. D. Mermin, *Solid State Physics*, Harcourt College Publishers, Fort Worth 1976

[17] C. Canali, Electron Devices, IEEE Transactions Volume 22, Issue: 11, 1975

[18] V. Radeka, Detector Signal Processing, `http://www.inst.bnl.gov/~poc/ShortCourse_Documents/NSS2009/VR_Lecture_NSS_2009-1\%20[Compatibility%20Mode].pdf` BNL 2009

[19] M. Lozano, AIDA Project Kick-Off Meeting, `http://scipp.ucsc.edu/~hartmut/UFSD/CNM.pdf`, CERN 2011

[20] S. Meroli et al., Energy Loss Measurement for Charged Particles in Very Thin Silicon Layers, 2011 JINST 6 P06013

[21] H.F.-W. Sadrozinski, Silicon Short Course, Firenze 2012

[22] H.F.-W. Sadrozinski, 4D Sensors: Unifying the Space and Time Domain with Ultra-Fast Silicon Detectors UFSD, DPF, `https://indico.bnl.gov/contributionDisplay.py?sessionId=17&contribId=158&confId=603`, University of California, Santa Cruz 2013

[23] Dougism, Visualisation of a Townsend Avalanche, `http://en.wikipedia.org/wiki/File:Electron_avalanche.gif`, 2012

[24] G. Casse et al., Enhanced Efficiency of Segmented Silicon Detectors of Different Thicknesses after Proton Irradiations up to 1e16 n.eq., Nucl. Instrum. and Methods A 624, 2, 2010

[25] J. Lange et al., Properties of a Radiation-Induced Charge Multiplication Region in Epitaxial Silicon Diodes, Nucl. Instrum. and Methods A 622, 2010

[26] P. Fernández et al., Simulation of New P-type Strip Detectors with Trench to Enhance the Charge Multiplication Effect in the N-type Electrodes, Nucl. Instrum. and Methods A658, 2011

[27] W. Maes, K. De Meyer, and R. Van Overstraeten, Impact Ionization in Silicon: A Review and Update, Solid-State Electronics Vol. 33 No. 6., 1990

[28] A. G. Chynoweth, Ionization Rates for Electrons and Holes in Silicon, Physical Review Volume 109, Number 1, 1958

[29] Sentaurus User Guide, Synopsys, 2010

[30] A. Macchiolo, Simulation of CCE for N-in-P 75 and 150um Thick Detectors Irradiated Up to a Fluence of 1e16 n.eq., `http://indico.cern.ch/getFile.py/access?contribId=`

1&sessionId=3&resId=0&materialId=slides&confId=86625, 16th RD50 Workshop, Barcelona, 2010

[31] S. N. Ahmed - *Physics and Engineering of Radiation Detection*, Academic Press Inc. Published by Elsevier, San Diego 2007

[32] A.G. Stewart et al., Study of the Properties of New SPM Detectors, Pro. SPIE 6119, 2006

[33] Electrical Properties of Silicon, Ioffe Physico-Technical Institute, <ioffe.ru/SVA/NSM/Semicond/Si/electric.html>

[34] R.W. Dutton, Perspectives on Technology and Technology-Driven CAD, IEEE Transactions, Vol. 19, No. 12, 2000

[35] C. Warwick, Everything You Wanted to Know About SPICE But Were Afraid to Ask, The EMC Journal, Issue 82, 2009

[36] S. Hidalgo et al., Simulation and Technology Development of Low Gain Avalanche Detectors (LGAD) for High Energy Physics Applications, https://indico.cern.ch/getFile.py/access?contribId=4&sessionId=3&resId=0&materialId=slides&confId=209612, 22nd RD50 Workshop, Albuquerque, 2013

[37] G. Kramberger et al., Studies of CNM Diodes With Gain, https://indico.cern.ch/getFile.py/access?contribId=28&sessionId=3&resId=0&materialId=slides&confId=209612, 22nd RD50 Workshop, Albaquerque, 2013